MIT/WHOI

Massachusetts Institute of Technology
Woods Hole Oceanographic Institution

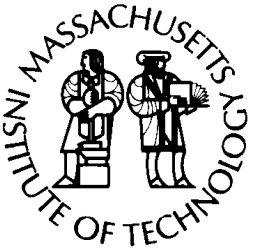

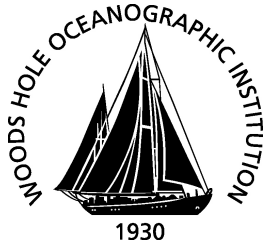

Joint Program in Oceanography/ Applied Ocean Science and Engineering

---

DOCTORAL DISSERTATION

Reconstructing Atmospheric Changes in Monsoon Regions Using Eolian Dust

by

Christopher William Kinsley

September 2019

RECONSTRUCTING ATMOSPHERIC CHANGES IN MONSOON REGIONS USING EOLIAN DUST

By

Christopher William Kinsley

MEarthSci, University of Oxford, 2012

Submitted in partial fulfillment of the requirements for the degree of

Doctor of Philosophy

at the

MASSACHUSETTS INSTITUTE OF TECHNOLOGY

and the

WOODS HOLE OCEANOGRAPHIC INSTITUTION

September 2019

Signature of Author 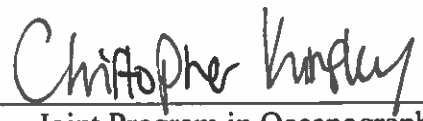

Joint Program in Oceanography/Applied Ocean Science and Engineering
Massachusetts Institute of Technology
and Woods Hole Oceanographic Institution
August 2, 2019

Certified by 

David McGee
Thesis Supervisor
Massachusetts Institute of Technology

Accepted by 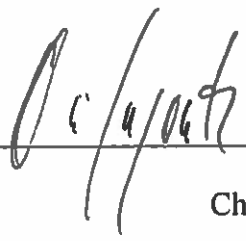

Oliver Jagoutz
Chair, Joint Committee for Marine Geology and Geophysics
Massachusetts Institute of Technology

RECONSTRUCTING ATMOSPHERIC CHANGES IN MONSOON REGIONS USING EOLIAN DUST

By

Christopher William Kinsley

Submitted to the MIT-WHOI Joint Program in Oceanography/Applied Ocean Science and Engineering on August 2, 2019 in Partial Fulfillment of the Requirements for the Degree of Doctor of Philosophy in Geochemistry

Abstract

Mineral dust is generated in continental interiors and exported by winds to ocean basins, providing a sedimentary archive which is one of the few direct indicators we have of atmospheric circulation in the past. This archive can be utilized in regions of dust transport also affected by monsoons to examine how different climate forcing mechanisms impact the monsoon regions over glacial-interglacial, orbital, and millennial timescales. This thesis generates new eolian dust records from two monsoon regions to reconstruct changes in atmospheric circulation in response to forcing by high-latitude insolation and boundary condition change. In Chapters 2 and 3 I use $^{230}Th_{xs}$-normalization to construct high-resolution eolian dust flux records from sedimentary archives downwind from the West African and East Asian Monsoon regions respectively. The West African margin dust records show variability associated with an interplay between Northern Hemisphere summer insolation forcing and North Atlantic cooling. The longest record at ODP Site 658, stretching back to 67 ka, shows evidence for a "Green Sahara" interval from 60-50 ka and a skipped precessional "beat" from 35-20 ka. This record also shows evidence for abrupt increases in dust flux associated with Greenland stadials. The Shatsky Rise record at ODP Site 1208, downwind of East Asian dust sources, shows variability associated with glacial-interglacial boundary conditions over the last 330 ka, exhibiting high dust during glacial times. The record also exhibits variability associated with a Northern Hemisphere summer insolation control at times overriding the glacial-interglacial signal. In Chapter 4 I demonstrate the feasibility of using radiogenic neodymium isotopes ($^{143}Nd/^{144}Nd$) at IODP Site U1430 in the Sea of Japan to fingerprint the provenance of eolian material at the core site from Asian dust sources. I then generate a $^{143}Nd/^{144}Nd$ record from isolated eolian material over the last 200 ka to examine Westerly Jet behavior in the Asian interior, which shows resolvable orbital-scale variability from 200 to 100 ka, and muted variability from 100 to 0 ka. The findings imply a quicker shift of the Westerly Jet to the north of the Tibetan Plateau during times of high Northern Hemisphere summer insolation and a strong Asian monsoon.

Thesis Supervisor: David McGee
Title: Associate Professor of Paleoclimate

Acknowledgments

First and foremost, I would like to thank my thesis advisor David McGee for his scientific guidance and support over the past 7 years. David took me on as his first PhD during his first year as a professor. The experience of seeing a lab built from the ground up was simply invaluable. David supported and encouraged me during all the ups and downs of the PhD process, and I am especially grateful for his understanding during the harder times I faced. He gave me the flexibility to be able to stay close with my family in the UK and other family members who live abroad, something which was very important to me.

I would also like to thank my thesis committee members, Delia Oppo, Olivier Marchal, and Bernhard Peucker-Ehrenbrink, as well as Gisela Winckler (who was unable to sit on the committee for the defense itself due to a research cruise), for their expertise and extensive input on all chapters of my thesis. I am especially grateful to Rick Murray for agreeing to serve as chair of my thesis defense, and along with co-chief scientist, Ryuji Tada, for giving me the opportunity to sail on IODP Expedition 346. This research cruise and subsequent post-cruise work, provided the samples for Chapter 4 of my thesis and was an unforgettable learning experience. I would also like to thank all of the scientists and technicians involved with this cruise (especially Jerry Dickens, Bill Anderson, Ann Dunlea, Chloe Anderson, Bobbi Brace, and Chad Broyles).

Over the years, many collaborators and scientists have been involved in my work in some fashion, and I am grateful for their mentorship and support. Alex Thomas and Gideon Henderson sent me down the paleoclimate and geochemistry research path during my Masters research project at the University of Oxford, and along with the guidance and expertise of Martin Brasier and Hugh Jenkyns, I could not have asked for a firmer grounding in the Earth Sciences. Tristan Horner and Sune Nielsen oversaw my second generals project during a wonderful summer that I spent at WHOI. Louisa Bradtmiller collaborated on two of my thesis chapters and her input has been much appreciated. I also want to thank the following lab managers, postdocs, graduate students, undergraduates, and lab administrators who I have had the privilege to work with during my time in the McGee Lab, and who taught me so much: Irit Tal, Ben Hardt, Adam Jost, Rick Kayser, Alan Hsieh, Christopher Hayes, Charlotte Skonieczny, Francois Tissot, Nick Scroxton, Elena Steponaitis, Christine Chen, Gabi Serrato Marks, Michaela Fendrock, Yan Zhang, Zach Norberg, Josh Murray, Almanzo Seguin, Melody Abedinejad, Annora Borden, and Erin Wedding.

The EAPS and WHOI administrative staff who have helped to make this experience so wonderful for me include: Ronni Schwarz, Kris Kipp, Meg Tivey, Jim Yoder, Megan Jordan, Julia Westwater, Vicki McKenna, and Lea Fraser. I was lucky enough to be involved with the Terrascope community at MIT for 3 years as the graduate teaching assistant, and I thank everyone in that fantastic group, especially Ari Epstein, Johnny Yang, Elise Chambers, Emily Martin, Clio Macrakis, Sabrina Mazer, and Anna Jungbluth.

My MIT-WHOI Joint Program and EAPS graduate student friends gave me much needed breaks from work, countless laughs, and great memories that sustained me through graduate school. To name a few: Sara Bosshart, Hector Fornes, Stephanie Brown, Ben Klein, Aimee Gillespie, Jaap Nienhuis, Rene Boiteau, Kelsey Stoeringer, Kate French, Deepak Cherian, Ross Williams, Sharon Newman, Dook, Jimmy Bramante, Yodit Tewelde, Simone Moos, Emily Matys, Ben Mandler,

Ruel Jerry, Arthur Olive, Niya Grozeva, Jill McDermott, Frank Centinello, Mike Sori, Alex Andrews, Annie Bauer, Emily Zakem, Dan Amrhein, Melissa Moulton, Sophie Chu, Kelsey Moore, and Jeemin Rhim. I had the good fortune to live with an amazing set of housemates while I lived in Cambridge and Somerville: Tsehai Grell, Maria Paula Angarita Fonseca, Sarah Luppino, and Spencer Shinaberry, and I can only thank them for putting up with me and having to actually live with me. I did manage to meet some people outside of graduate school, surprisingly, and I am thankful for their friendship of the following people: Robert Wainblat, Kevin Hillburn, and Christopher Campbell.

My friends from Oxford and home (St Andrews) offered endless support from afar throughout this experience (and amazingly almost all made it out to Boston to visit me at one point or another): Jennifer Falconer (and her parents Isobel and Kenneth who were instrumental on my path to Oxford), Charlotte Toon, Ruth Campbell, Tom Chalk, Isabel Wood, Helen Leach, Neil Morton, Chris Tatum, Charlie Wilson, Aletta Warne, Rhea Wolfson, Thomas Harrison, Lily Muller, Katie Bray, Kimberley Pyle, Catherine Hirst, Paul Starr, Erica Webb, and Rebecca Neely.

And finally, my deepest and most profound love and thanks to my big family, who I am so lucky beyond measure to have. Words falter. You all mean the absolute world to me. My grand and great-grandparents: Gangan, Granny Mary, Grandad, and Granny Morrison, who passed along so much wisdom to me. Aunts, uncles, cousins, and friends who have all been as close as parents and siblings to me: Susan, Eric, Kathryn, Fraser, Jonathan, Graham, Sheila, Andy, Stephanie, Natalie, Kaz, Zak, Joan, Dorothy, Louise. The Mikey, I am so grateful we found each other, I could not have done this without your unwavering support over the last few years. Piper (both real and my stuffed animal version!) you have brought such joy in such a short amount of time to us all. Smoochy, to the best frog and travel partner a boy could have had. Bobo, my younger but bigger brother, your presence in my life has kept me grounded, and the many many laughs that we have had together over all the years of growing up are a treasure to me - so long may they continue! Mummy. Daddy. You've given me everything. I share this accomplishment with you with my humblest and most heartfelt gratitude.

This thesis research was supported by the National Science Foundation under Grant Nos. OCE-1030784 and EAR-1434138 and a Post-expedition activity award through the U.S. Science Support Program, Integrated Ocean Drilling Program. Kinsley was supported by fellowships from the MIT Department of Earth, Atmospheric, and Planetary Sciences in his first year of graduate school and the WHOI Academic Programs Office in his sixth year of graduate school.

Contents

List of Figures

1. Monsoons and dust

2. Orbital- and Millennial-Scale Variability in North African Dust Emissions Over the Past 67 ka

3. North Pacific Dust Fluxes at ODP Site 1208 (Shatsky Rise) Over the Last 330 ka

4. Eolian Dust Provenance Changes Recorded in Japan Sea Sediments (IODP Site U1430) Over the Past 200 ka by Radiogenic Pb, Nd, and Sr Isotopes

Chapter 1

Monsoons and Dust

Monsoon circulations are major features of the tropical atmosphere, which, primarily through the rainfall associated with them, are of profound importance to a large fraction of the world's population (Clift & Plumb, 2008). Monsoon climates are characterized by a strong seasonal cycle, with wet summers and dry winters, and involve a reversal of wind direction from equatorward-easterly flow in the dry season to poleward-westerly flow after monsoon onset. Paleo-records have found dramatic changes to monsoon circulations on millennial, orbital, and tectonic timescales. As these heavily populated regions will be affected by future climate change, bringing changes to atmospheric circulation, the need to understand controls on monsoon circulations is fundamental. Windblown dust proxies can be used to aid in reconstruction of the atmospheric response to changing climate in monsoon regions. Deserts at the poleward limits of the Asian-Indian Ocean-Australian and the West African monsoon systems are the largest source areas for dust worldwide (Figure 1-1). This observation points to the potential of reconstructions of windblown dust using sedimentary archives to provide insights into changes in winds and aridity at the edges of these monsoon systems in the past. Dust reconstructions can also provide insight into the role of dust radiative forcing in amplifying climate change, and its role in marine biogeochemical cycles.

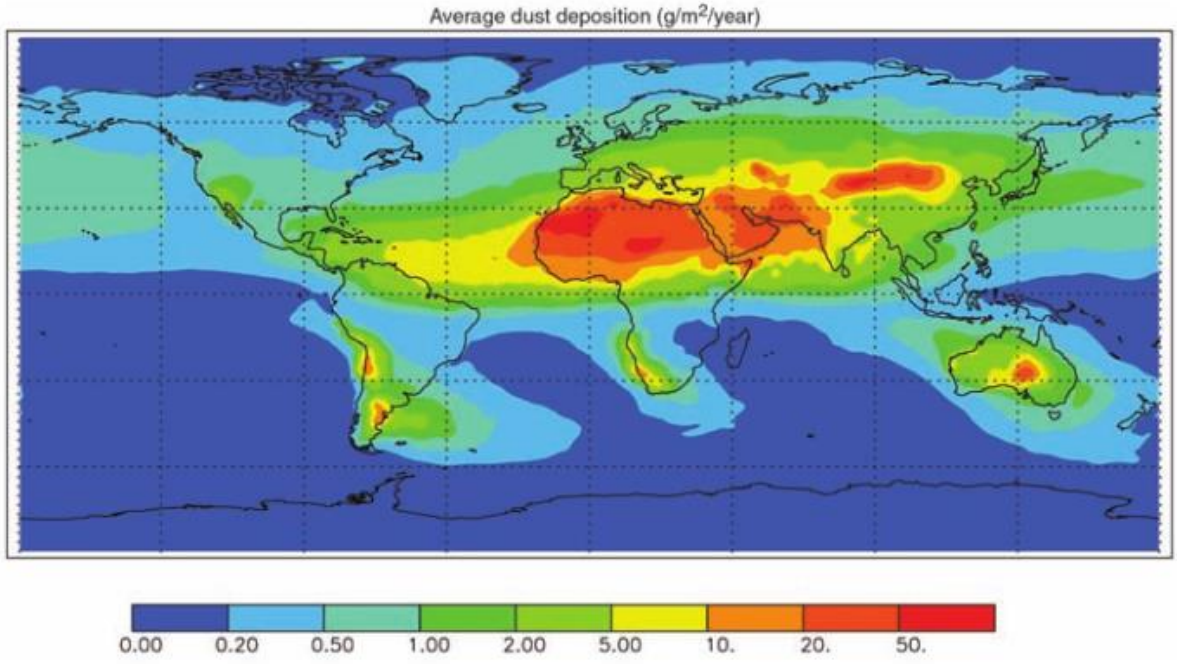

Figure 1-1. Dust fluxes to the land and ocean surfaces based on a composite of three published modeling studies that match satellite optical depth, in situ concentration, and deposition observations (Jickells et al., 2005).

This thesis focuses on reconstructing the atmospheric response to glacial-interglacial, orbital-, and millennial-scale climate variability in two Northern Hemisphere monsoon regions as indicated by dust proxy records. I generate new high resolution ^{230}Th-normalized dust flux records for the West African monsoon over the last 67 ka (Chapter 2) and the East Asian monsoon over the last 330 ka (Chapter 3), and a record of changing dust provenance for the East Asian monsoon over the last 200 ka (Chapter 4).

Chapter 2

Orbital- and Millennial-Scale Variability in North African Dust Emissions Over the Past 67 ka

2.1 Abstract

High resolution reconstructions of eolian dust flux to West African margin sediments can be used to explore changing atmospheric circulation and hydroclimate over North Africa on millennial to orbital timescales. Dust flux records from the margin over the past 20 ka, and the Mid-Atlantic Ridge over the past 70 ka, show variability associated with both summer insolation and North Atlantic cold periods. Here, we extend existing dust flux records from the West African margin back to 35 ka in a transect of core sites from 19°N to 27°N, and back to 67 ka at ODP Hole 658C, in order to explore the interplay of orbital and high-latitude forcings on North African climate and make quantitative estimates of dust flux during the core of the Last Glacial Maximum (LGM; 23-19 ka).

The ODP 658C record shows a "Green Sahara" interval from 60-50 ka during a time of high Northern Hemisphere summer insolation, with low dust fluxes similar to levels during the African Humid Period (AHP; 12-5 ka), and an abrupt peak in flux associated with Heinrich event 5a (H5a; ~55 ka). A general trend of increasing dustiness is observed from 60 to 35 ka while the Northern Hemisphere cools, with multiple millennial-scale peaks in dust flux associated with cool events in the North Atlantic superimposed on top of the longer-term dust increase. From 35 ka through the LGM all cores exhibit a coherent decrease in dust deposition, with millennial-scale peaks in dust flux associated with H3 (~32 ka) and H2 (~25 ka). A striking feature of these records is the absence of a strong low-latitude insolation response in dust flux over the interval from 35-20 ka, suggesting a skipped precessional "beat". The dust fluxes at all core sites were relatively moderate during the LGM, with mean values near late Holocene levels, suggesting much lower glacial-interglacial response than observed in mid-latitude dust sources.

2.2 Introduction

Records of mineral dust emissions from the Sahara Desert are essential for understanding past changes in North African climate, and are tightly linked to the strength of the West African monsoon (deMenocal, 1995; deMenocal, et al., 2000; Skonieczny et al., 2019; Wang, et al., 2015). Wind speed and aridity variations are expressed as fluctuations in the amount of dust exported from the North African continent to the Atlantic Ocean, meaning that downcore measurement of dust flux to North Atlantic sediments allows an integrated reconstruction of how winds and aridity respond to climate changes.

Presently, mineral dust is emitted from North African sources as a result of dust storms, and blown across the northwest African continental margin and over the Atlantic Ocean. Annual dust emissions are the cumulative result of dust outbreak events transporting material to the margin throughout the year, with maximum emissions during winter and early spring, moderate emissions in summer, and minimum emissions of dust in fall (Ridley et al., 2012). Observational records of interannual and decadal-scale variability of dust emissions attribute peak winter dust to reduced rainfall associated with southward movement of the Intertropical Convergence Zone (ITCZ) and increased surface winds over North African dust source regions (Van der Does et al., 2016; Doherty et al., 2012; Ridley et al., 2012).

Paleoclimate proxy records and geochemical tools have been used to extend the record of variability of dust transport to the margin beyond the observational record, which exists only from the mid-1960s (Prospero & Lamb, 2003). Records of the last 20 ka were developed using sediments from ODP Hole 658C by deMenocal et al. (2000) and Adkins et al. (2006). Later work demonstrated that the variations in this core were coherent along the northwest African margin between 19°N and 27°N (McGee et al., 2013) and were observed across the Atlantic Basin in the Bahamas and central Atlantic as well (Williams et al., 2016). These reconstructions show an abrupt transition from a time of high dust accumulation during the deglaciation to a sustained period of low dust accumulation between 12 and 5 ka. This low-dust period is known as the African Humid Period (AHP) and is marked by an abrupt onset and termination, followed by a more gradual increase of dust accumulation toward the present. Comparison of these dust records with other

climate proxy records of North African climate shows that the AHP marks a "Green Sahara", when the Sahara Desert received high rainfall supporting diverse and widespread vegetation, permanent lakes, and human populations (McGee & deMenocal, 2017, and references therein), with accompanying continental runoff (Skonieczny et al., 2015). The AHP occurred when Northern Hemisphere summer insolation was increased relative to the present due to precessional variation, which has been shown through modeling efforts to increase the extent and intensity of the monsoon system (Battisti etal., 2014; Braconnot et al., 2012; Kutzbach, 1981; Tjallingii et al., 2008). There is also evidence that trade wind strength was decreased over the West African margin during the AHP, as evidenced by decreased wind-induced biogenic fluxes to margin sediments and increased sea surface temperatures (SSTs) along the margin (Adkins et al., 2006; Bradtmiller et al., 2016). These findings over the AHP highlight two controls on changes to dust flux from North Africa, aridity and wind strength, and the importance of considering the interplay between the two. The AHP was a time of increased humidity over North Africa, with increased soil moisture and vegetation cover reducing dust generation from source regions, with accompanying reductions in trade wind strength further limiting dust export to the margin. Together, the data and modeling reveal a strong summer insolation control on African climate and its expression in dust flux records over the past 20 ka.

These studies also began to elucidate dramatic intervals of rapid and high-amplitude changes to climate and dust transport in this region over far shorter timescales, punctuating the orbitally-forced record at a millennial scale. During abrupt North Atlantic cooling events such as Heinrich event 1 (H1) (18-14.7 ka) and the Younger Dryas (YD) (12.9-11.7 ka), abrupt increases in dust flux have been recorded at multiple sites over the margin, with fluxes reaching the highest values of their respective records during these events (Mulitza et al., 2008). Comparison of these dust records to other climate proxy records in the region has been used in combination with numerical modeling efforts in an attempt to understand the relationship between these abrupt increases of dust and North Atlantic climate.

Multiple studies have linked North Atlantic cooling to increases in northeasterly winds over North Africa (deMenocal et al., 1993; Liu et al., 2014; McGee et al., 2018; Mulitza et al., 2008; Tjallingii et al., 2008). Cooling of winter SSTs and expansion of sea ice in the North Atlantic shift the

Atlantic ITCZ to the south, weakening the monsoon and increasing trade wind strength, leading to an increase of dust export (Liu et al., 2014; Meyer et a., 2013; Murphy et al., 2014). Consistent with this finding from models, northwest African margin sediments record increases in the accumulation of biogenic opal and organic carbon during these cold events, suggesting increased wind-driven upwelling (Adkins et al., 2006; Bradtmiller et al., 2016; Romero et al., 2008). A weakening of monsoon rainfall during North Atlantic cooling events also shifts the Sahel-Sahara boundary south (Collins et al., 2013), potentially opening up new dust source areas and further contributing to the increase in dust emissions during these events. These high-resolution studies provide evidence for a North Atlantic high-latitude control causing abrupt changes to atmospheric circulation and North African climate on millennial timescales, in addition to the low-latitude orbital regulation of African monsoonal climate.

Recent efforts by Skonieczny et al. (2019) have shown a high correlation of Saharan dust flux, calculated using ^{230}Th normalization, with summer insolation over the last 240 ka, confirming low-latitude pacing of northwest African dust fluxes at 18°N spanning at least the last two glacial cycles for sediment core MD03-2705. Low sedimentation rates for core MD03-2705, which is adjacent to ODP Hole 658C, precluded detailed study of potential millennial scale controls on North African climate over this longer time frame. Here we present northwest African margin dust flux records from core sites with higher sedimentation rates (5-10 cm/kyr) to explore the combined effects of high-latitude and orbital forcing of African climate extending back to 67 ka. Probing this time period allows us to make quantitative estimates of dust flux during the core of the LGM, and examine over multiple precessional cycles the impact of high-latitude and summer insolation forcing on dust export. Drawing on the mechanistic links between regional climate and dust export, we aim to deepen understanding of changing climate of the North Africa region over the past 67 ka.

2.3 Methods and Core Sites

2.3.1 Core Locations

A meridional transect of 4 core sites between 27°N and 19°N were used in this study (Figure 2-1). These sites have been used to monitor past variations in northwest African climate, as they represent North African dust emissions to the tropical North Atlantic (McGee et al., 2013; Williams et al., 2016). The three gravity cores GC37, GC49, and GC68, were taken by the R/V Oceanus during the 2007 Changing Holocene Environments of the Eastern Tropical Atlantic (CHEETA) cruise (OC437-7). The sediments from Ocean Drilling Program Hole 658C off Cap Blanc, Mauritania were cored during ODP Leg 108 (Ruddiman et al., 1988).

2.3.2 Age Models

The chronologies for the OC437-7 cores were developed from AMS radiocarbon ages on planktonic foraminifera (see Appendices Figure 2-10). Radiocarbon ages younger than 20 ka in GC37 and GC68 and ages as old as 31.5 ka in GC49 were taken from McGee et al., (2013). Seven new radiocarbon ages were measured for this study. The ages for this study were determined on specimens of *Globigerina bulloides*; radiocarbon measurements were performed at the Center for Accelerator Mass Spectrometry at Lawrence Livermore National Laboratory. Radiocarbon ages were converted to calendar ages using Marine13 (Reimer et al., 2013), with an additional reservoir correction (ΔR) of 130 ± 50 yr (2σ) based upon local modern reservoir ages (Mulitza et al., 2010; Ndeye, 2008; Pittauerov et al., 2009). We do not attempt to estimate past changes in reservoir age, though these most certainly accompanied the dramatic changes in upwelling observed in African margin records (Bradtmiller et al., 2016; Romero et al., 2008). Age models were interpolated between ^{14}C tie points using the P_Sequence routine in OxCal 4.2 (Bronk Ramsey, 2008). This routine provides Bayesian age-depth modeling and treats sediment deposition as a series of discrete "events" following a Poisson distribution with a user-specified step size. A step size (k) of 0.75 cm^{-1} provided sufficient flexibility in the age-depth relationship to fit our ^{14}C ages.

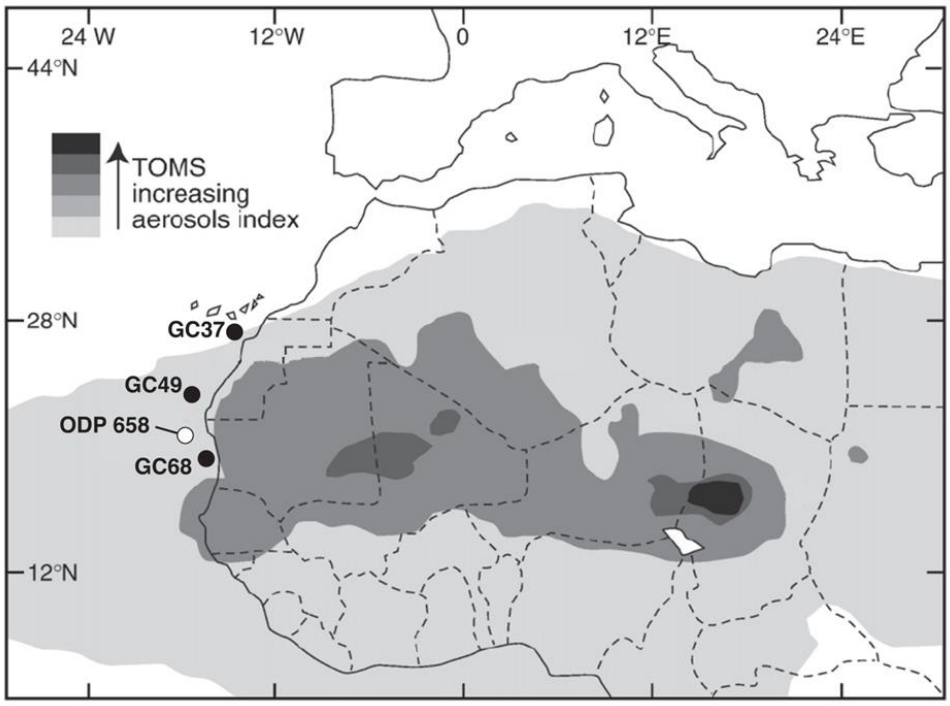

Figure 2-1. Map showing core sites and the TOMS 13-year (1992–2005) averaged aerosol concentrations (http://toms.gsfc.nasa.gov/aerosols/aerosols_v8.html). Modified from (Cole et al., 2009). Core locations and depths as follows: GC37 (26°81'N, 15°12'W, 2771 m), GC49 (23°21'N, 17°85'W, 2303 m), ODP 658C (20°45'N, 18°35'W, 2263 m), GC68 (19°36'N, 17°28'W, 1454 m).

The chronology for the ODP 658C core is based on AMS radiocarbon ages and correlation to a geochemical record from a nearby core with existing age model (see Appendices 2.A). From the coretop to 20 ka radiocarbon ages from deMenocal et al. (2000) are utilized, and two new radiocarbon ages determined on specimens of *Globigerina bulloides* were measured for this study to constrain the chronology from 30 to 38.5 ka. Radiocarbon ages were calibrated using Marine13 and a constant ΔR of 130 years. Between 25 ka and 67 ka the chronology is based on matching $CaCO_3$ weight percent in ODP 658C to calibrated XRF $CaCO_3$ weight percent in neighboring core GeoB7920-2 (see Appendices Figure 2-8). The age model for this part of GeoB7920-2 is based on visual correlation of the benthic (*Cibicidoides wuellerstorfi*) $\delta^{18}O$ record with that of marine sediment core MD95-2042, with the $\delta^{18}O$ stratigraphy of MD95-2042 on the GRIP ss09sea age scale (Tjallingii et al., 2008).

2.3.3 Determination of Biogenic Components and Eolian Fraction of Sediments

The detrital percentage of the samples was calculated as the residual after subtracting the carbonate, opal and organic carbon percentages measured at Macalester College. Percent carbonate and percent total carbon were determined through coulometry. Percent organic carbon was calculated as the difference between total carbon and carbonate carbon. Percent biogenic opal was determined using alkaline extraction and molybdate blue spectrophotometry after the method of Mortlock & Froelich (1989).

The eolian fraction of the sediments was calculated by measuring grain size and utilizing endmember modeling of grain size distributions to sum the two coarsest endmembers, which are taken to represent the eolian fraction of the detrital material, as determined above. Prior to grain size measurement the non-detrital fraction of the sediment was removed in a stepwise leaching procedure. Organic matter and calcium carbonate were removed in a glass beaker using excess 10% hydrogen peroxide and 0.1 M hydrochloric acid, respectively. Opal was removed by transferring the samples to centrifuge tubes, adding excess 2 M sodium carbonate, and heating the samples in an 80°C hot bath for 5 hours. Grain size measurements were made on a Beckman Coulter LS 13320 Laser Diffraction Particle Size Analyzer at the Royal Netherlands Institute for Sea Research.

The grain size distribution below 250 μm was used for grain size endmember modelling in order to separate eolian from hemipelagic inputs. The grain size data for each core was fit using Weibull distributions, which are unimodal, asymmetric distributions that closely approximate measured grain size distributions of airborne dust and loess (Sun, 2004; Zobeck et al., 1999). Three endmembers per core were used to model the grain size distributions, with the two coarsest endmembers identified as eolian dust, following the work of McGee et al., (2013). The proportion of the grain size distribution that is accounted for by the two coarsest endmembers was taken as the fraction of the detrital material that is eolian, and this value was multiplied by the detrital percentage to obtain the eolian fraction of the bulk sediments.

The same endmember distributions that McGee et al., (2013) calculated for cores GC37, GC49, and GC68 were utilized to estimate eolian fractions for new sediment samples in this study for those sites. For core ODP 658C best fit endmember distributions were calculated from grain size distribution data on all samples worked on in this study (from 18.879 ka to 67.019 ka), and used to estimate the eolian fraction of the bulk sediments (see Appendices 2.B).

2.3.4 Uranium, Thorium Isotope Measurements

Eolian fluxes were calculated by multiplying the eolian fraction of the sediments by the vertical sediment flux. Sediment fluxes were calculated using $^{230}Th_{xs}$-normalization (Bacon, 1984; Suman & Bacon, 1989), which utilizes the fact that the instantaneous ratio of water column scavenged ^{230}Th flux to the total sediment flux must be equal to the concentration (in dpm g^{-1}) of ^{230}Th in the underlying sediment:

$$\text{normalized eolian flux} = \frac{\beta z}{[^{230}Th_{xs}^{0}]} F$$

(Equation 2.1)

where β is the production rate of ^{230}Th from ^{234}U in the water column (0.0268 dpm m^{-3} yr^{-1}, McGee et al., 2010), z is the water column depth, $[^{230}Th_{xs}{}^{0}]$ is the concentration of the component of the total $^{230}Th_{meas}$ that is not derived from detrital material or supported by ^{238}U decay within the

sediments, and has been corrected for decay since it was deposited, and *F* is the fraction of eolian material. The water column depth was adjusted for changing sea level (Waelbroeck et al., 2002) as this affects the production rate of ^{230}Th in the water column.

$^{230}Th_{xs}^{0}$ is calculated using the following equation:

$$^{230}Th_{xs}^{0} = e^{\lambda_{230}t} \times \left[^{230}Th_{meas} - ^{230}Th_{det} - ^{230}Th_{auth} \right]$$

(Equation 2.2)

The correction for decay was made using the age model of the core to assign an age to each sample and account for the decay of initial excess $^{230}Th_{xs}$ since the time of deposition. The detrital ^{230}Th was calculated by assuming the ^{232}Th content of the sample was entirely sourced from the detrital component, and calculating the activity of the ^{238}U associated with this detrital component using a 'known' detrital U/Th ratio of 0.7 ± 0.05 (1σ) for this area (Adkins et al., 2006). The detrital ^{230}Th is assumed to be in secular equilibrium with this uranium, so it can be subtracted from the $^{230}Th_{meas}$. Authigenic uranium is taken to be that which remains after accounting for the detrital uranium. Authigenic ^{230}Th is therefore calculated by assuming that the formation of authigenic minerals/coatings occurs at the time of sediment deposition and incorporates $^{234}U/^{238}U$ at a constant seawater ratio of 1.1468 (Andersen et al., 2010).

In preparation for isotopic measurements samples were weighed, doped with a mixed spike of ^{229}Th and ^{236}U, and fully dissolved with hydrogen peroxide, nitric acid, hydrochloric acid and hydrofluoric acid. An iron coprecipitation step allowed removal of much of the matrix of the dissolved sediments and thus improved yields of Th and U. Samples then underwent anion exchange chromatography using Dowex Bio-Rad AG1-X8 100-200 mesh anion exchange resin to elementally separate Th and U so that the two elements could be measured separately. ^{230}Th, ^{232}Th, and ^{238}U isotope measurements were made using a multi-collector inductively coupled plasma source mass spectrometer (MC-ICP-MS). The majority of isotopic measurements were made using a ThermoScientific Neptune Plus MC-ICP-MS at Brown University; more recent measurements were made on a Nu Plasma II-ES MC-ICP-MS at MIT.

Uncertainties in the final eolian fluxes reported reflect confidence limits associated with mass spectrometric measurements, the detrital U/Th ratio, and the eolian fraction of the sediments.

2.4. Results

The meridional sediment core transect along the northwest African margin reveals latitudinal differences in the relative expressions of low-latitude (orbital monsoon) and high-latitude (glacial and stadial event) forcing on regional dust fluxes and coastal upwelling (Figure 2-2; see Appendix A for the data). Dust, opal, and organic carbon fluxes for the 0-20 ka portions of GC37, GC49 and GC68 were previously published in McGee et al., (2013) and Bradtmiller et al., (2016), respectively. Detrital fluxes for the 0-20 ka portion of ODP 658C were previously published in Adkins et al., (2006).

2.4.1 GC37 (27°N)

Dust fluxes in core GC37 exhibit a maximum from 36 to 31 ka during late MIS3 (~0.5 g cm^{-2} kyr^{-1}), with a millennial-scale peak coincident with H3 (31.3 ka) (Sanchez Goñi & Harrison, 2010). Fluxes gradually fall during MIS2 to moderately low values (0.26 g cm^{-2} kyr^{-1}) in the late LGM (~20 ka), with a small dust peak associated with H2 (24 ka). Dust fluxes rise to millennial-scale peaks during H1 (0.37 g cm^{-2} kyr^{-1}) and the YD (0.47 g cm^{-2} kyr^{-1}), with the YD showing a 20% higher peak flux of dust than H1. Fluxes abruptly fall during the onset of the AHP at ~11 ka, and continue to fall to the lowest recorded value at ~6 ka (0.09 g cm^{-2} kyr^{-1}). Dust fluxes then increase into the Late Holocene (~1 ka) to a value of ~0.2 g cm^{-2} kyr^{-1}.

Both opal and organic carbon fluxes are highly correlated with dust fluxes in core GC37 ($r^2 = 0.69$ and 0.43, respectively). Similar to dust, both opal and organic carbon are at maximum levels at ~36 ka, the base of the core. Biogenic fluxes decrease into the LGM, with opal more closely tracking dust and organic carbon dropping rapidly after 30 ka. Opal fluxes rise to high levels during both H1 and the YD, while organic carbon fluxes peak only in H1. Fluxes of both opal and organic carbon fall to low levels throughout the AHP before rising during the late Holocene.

2.4.2 GC49 (23°N)

Dust fluxes in core GC49 decrease steadily from a late MIS3 maximum at 36 ka (0.74 g cm^{-2} kyr^{-1}) to moderately low values during the late LGM at ~21 ka (0.52 g cm^{-2} kyr^{-1}), with a small peak coincident with H2 (24 ka). Dust fluxes then rise to peaks during H1 (0.65 g cm^{-2} kyr^{-1}) and the YD (0.84 g cm^{-2} kyr^{-1}), before decreasing to a minimum during the AHP (0.08-0.11 g cm^{-2} kyr^{-1}). Similar to the GC37 record, the dust flux peak associated with the YD is larger – by ~30% – than the H1 peak, showing a stronger dust response during the YD in the northern core sites. Dust fluxes then increase into the Late Holocene to a value of 0.52 g cm^{-2} kyr^{-1}.

Both opal and organic carbon fluxes are highly correlated with dust fluxes in core GC49 (r^2 = 0.45 and 0.39, respectively). Opal and organic carbon fluxes are at high levels during late MIS3 at ~36 ka, the end of the core, and both decrease into the LGM. Opal fluxes more closely track dust fluxes, also showing a peak coincident with H2 (24 ka), while the organic carbon fluxes drop rapidly after 30 ka and are highly variable during the early part of the LGM. Opal fluxes rise to high levels during H1 and the YD, while organic carbon fluxes peak only in H1 and show an earlier peak from 18-21 ka at the end of the LGM. Fluxes of both opal and organic carbon fall to low levels throughout the AHP before rising during the late Holocene.

2.4.3 GC68 (19°N)

Core GC68 provides the highest resolution dust fluxes in this study due to the high sediment accumulation rates at this site. From 26 ka to the end of the LGM, dust fluxes show a slight decrease punctuated by abrupt rises and falls between values of ~4.5 to ~2 g cm^{-2} kyr^{-1}, including a small peak coincident with H2 (24 ka) and a prominent peak at ~21 ka. Dust fluxes then rise to peaks during H1 (~6 g cm^{-2} kyr^{-1}) and the YD (~4.2 g cm^{-2} kyr^{-1}), before decreasing to a minimum during the AHP (0.39-0.49 g cm^{-2} kyr^{-1}). In contrast to cores GC37 and GC49, the H1 peak dust flux is larger than the YD peak dust flux (by ~50%), showing a stronger dust response during H1 at this southern core site. Dust fluxes then increase into the Late Holocene (~2 ka) to a value of 1.64 g cm^{-2} kyr^{-1}.

Figure 2-2. Opal (blue line, open diamonds), C_{org} (red line, open squares), dust (black line, open circles), and detrital (grey line, open circles) flux records arranged from north to south as labeled. Data <20 ka in GC37, GC49, and GC68 from Bradtmiller et al., (2016); data <20 ka in ODP 658C from Adkins et al., (2006).

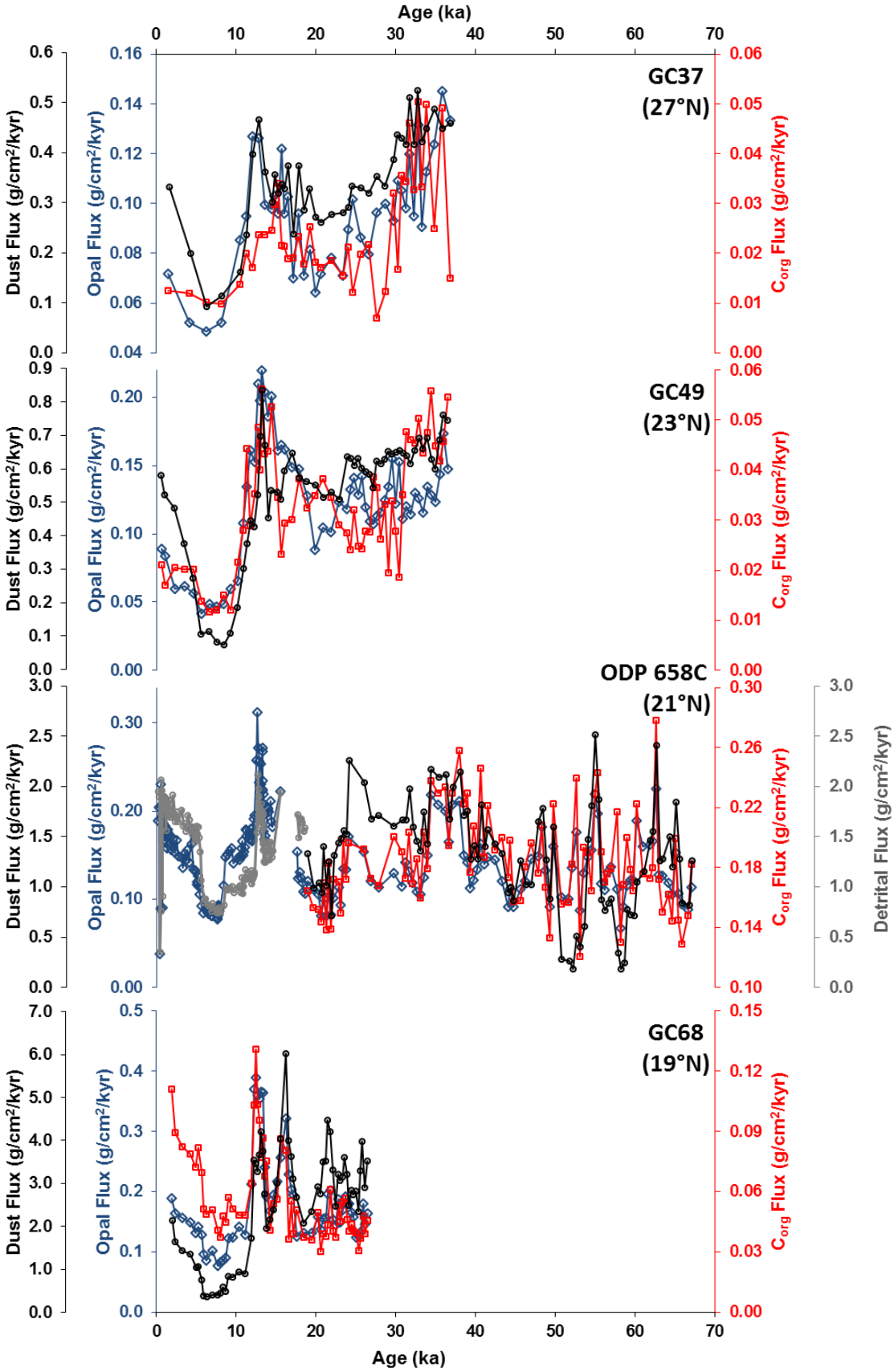
Age (ka)
GC37
(27°N)
GC49
(23°N)
ODP 658C
(21°N)
GC68
(19°N)
Dust Flux (g/cm²/kyr)
Opal Flux (g/cm²/kyr)
Corg Flux (g/cm²/kyr)
Detrital Flux (g/cm²/kyr)

Opal fluxes are highly correlated with dust fluxes in core GC68 ($r^2 = 0.44$), while organic carbon fluxes show very low correlation ($r^2 = 0.02$). From 26 ka, the end of the core, to the end of the LGM opal fluxes show a slight decrease punctuated by abrupt rises and falls similar to the dust record, also recording peaks coincident with H2 and at ~21 ka. Organic carbon fluxes show a substantial difference from dust fluxes from 26 ka to the end of the LGM with no noticeable trend and high variability. Biogenic fluxes rise to high levels during both H1 and the YD, with the YD peak slightly larger than the H1 peak in both opal and organic carbon fluxes. Fluxes of both opal and organic carbon fall to low levels throughout the AHP before rising during the late Holocene.

2.4.4 ODP 658C (21°N)

The ODP 658C core provides a longer archive than the CHEETA cores and allows continued high-resolution study of dust accumulation rates to the margin. Here we extend the record back to 67 ka. The early portion of the record at the latter stages of MIS4 shows moderate dust fluxes to the margin followed by an abrupt peak (2.4 g cm^{-2} kyr^{-1}) coincident with H6 (62.5 ka). This is followed by a decline in dust flux over 3 ka to an interval from 60-50 ka when the lowest dust fluxes (0.18 g cm^{-2} kyr^{-1}) observed in the record for this site are recorded. This low dust interval is interrupted by an abrupt [millennial-scale] dust increase to the highest fluxes (2.5 g cm^{-2} kyr^{-1}) observed in the whole record centered at H5a (55 ka). A trend of increasing dustiness is then observed after the end of the 60-50 ka low dust interval, reaching a maximum (~2.1 g cm^{-2} kyr^{-1}) at 35 to 33 ka. Millennial-scale variability is superimposed on this broad trend, including a peak in flux (1.8 g cm^{-2} kyr^{-1}) coincident with H5 (48 ka). Dust fluxes decrease from the late MIS3 maximum to (~1 g cm^{-2} kyr^{-1} at) at the end of the LGM (20 ka), with millennial-scale abrupt peaks in flux of 2 g cm^{-2} kyr^{-1} and 2.26 g cm^{-2} kyr^{-1}, coincident with H3 (31.3 ka) and H2 (24 ka) respectively. Following the LGM, the remainder of the dust record from this site is a detrital flux record (Adkins et al., 2006), as grain size-based estimates of the eolian fraction of detrital sediments are not available. Detrital fluxes rise to millennial-scale peaks during Hl (1.94 g cm^{-2} kyr^{-1}) and the YD (2.12 g cm^{-2} kyr^{-1}) before decreasing to sustained low values (0.75-1 g cm^{-2} kyr^{-1}) during the AHP; a hiatus occurs during H1, so the peak of H1 fluxes is missing in this record. Detrital fluxes increase abruptly at 5ka and continue to rise steadily into the Late Holocene to a value of ~2 g cm^{-2} kyr^{-1}.

Both opal and organic carbon fluxes are positively correlated with dust fluxes in core ODP 658C (r^2 = 0.46 and 0.32, respectively). Both opal and organic carbon fluxes increase from moderate values at the end of MIS4 to two peaks coincident with H6 and H5a separated by an interval of lower fluxes, with the organic carbon showing higher amplitude rises and falls during the interval of lower fluxes. Biogenic fluxes variably rise and fall from H5a until ~45 ka when both opal and organic carbon fluxes gradually increase to a maximum at 38 to 34 ka. Both opal and organic carbon fluxes drop sharply at 33 ka and remain low throughout MIS2 and the LGM, with small peaks at MIS3 and MIS2. The opal flux record shows peaks during H1 and the YD, falls to low levels throughout the AHP, and rises during the late Holocene. From the end of the LGM to the Holocene organic carbon data was not measured in this study.

2.5 Discussion

2.5.1 Major Features of Dust Flux Records from Four Sites along the NW African Margin from 20-67 ka (MIS 2 through 4)

This work has extended the CHEETA dust flux records to the bottom of cored material reaching back to 37 ka in GC37, 36.5 ka in GC49, and 26.5 ka in GC68, and produced a dust flux record from 67 to 19 ka for the core from ODP Hole 658C (Figure 2-3). The extended portions of the ODP 658C, GC37, and GC49 records overlap from 37 ka to 20 ka and demonstrate coherent variation on both orbital and millennial timescales. Heinrich events 2 and 3 are recorded as increases in dust flux superimposed on a decreasing trend of dustiness through the end of the LGM. The GC68 record also shows H2 recorded as a time of increased dust flux, and a decreasing trend of dustiness through the end of the LGM, while also showing higher frequency variability from 26 to 20 ka with multiple abrupt peaks in dust flux. In the northern core sites (ODP 658C through GC37, 21°-27°N), peak dust fluxes in early MIS2 (27 to 23 ka) are similar to modern, and only in the southernmost core site (GC68, 19°N) are early MIS2 fluxes higher than modern (by ~50%). In all cores, dust fluxes drop from early MIS2 to the LGM (23 to 19 ka) by 20-40%. The strong agreement between dust records from 37-19 ka gives us confidence that the extended ODP 658C record from 37-67 ka is faithfully recording the export of dust to the margin.

Figure 2-3. Dust (black line, open circles) and detrital (grey line, open circles) flux records arranged from north to south as labeled with 1σ uncertainties shown. Data <20 ka in GC37, GC49, and GC68 from McGee et al., (2013), data <20 ka in ODP 658C from Adkins et al., (2006). ^{14}C tie points and 1σ uncertainties shown as black triangles, $CaCO_3$ tie points for ODP 658C shown as black squares.

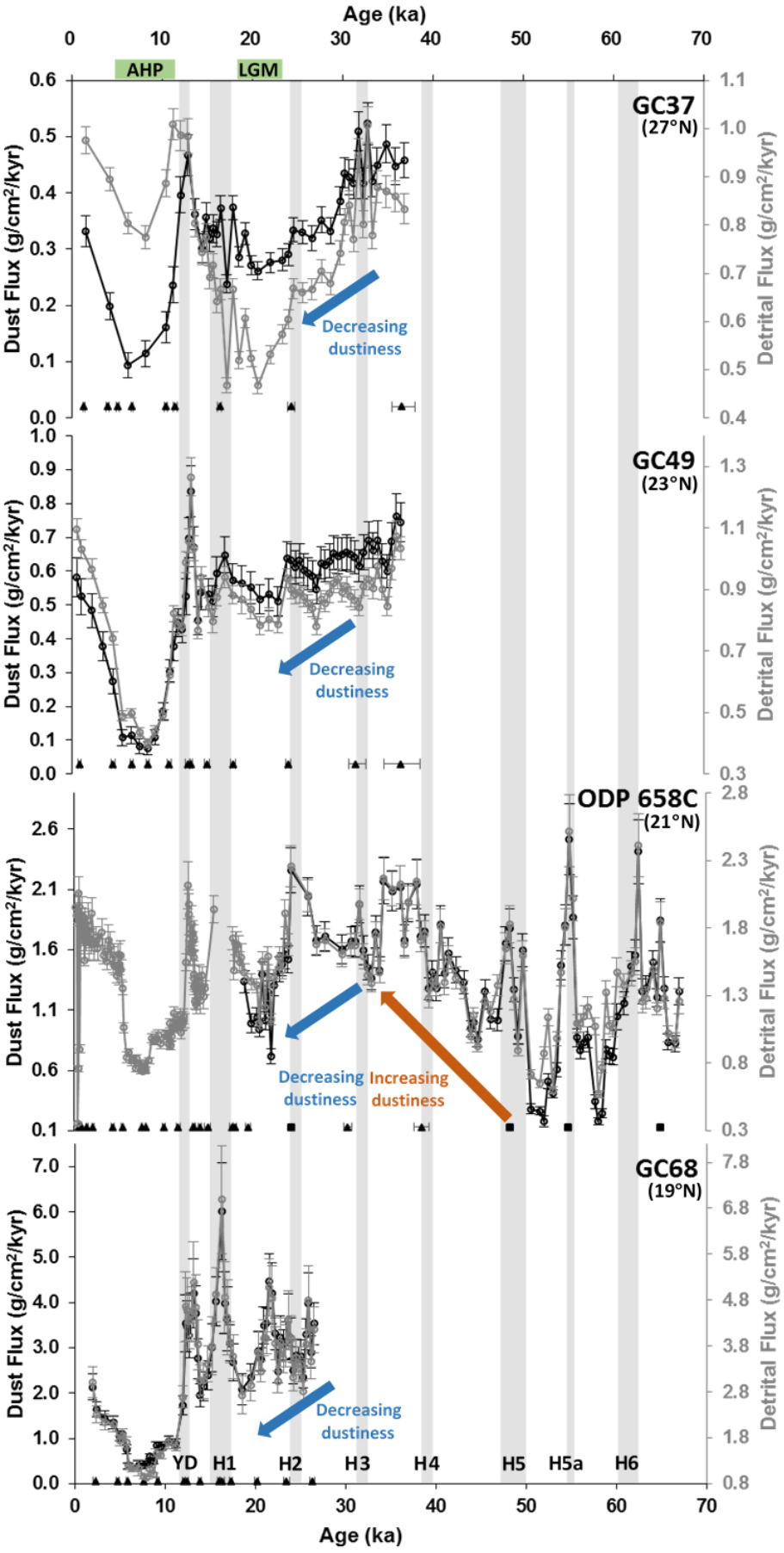
Age (ka)
AHP
LGM
GC37
(27°N)
Dust Flux (g/cm²/kyr)
Detrital Flux (g/cm²/kyr)
Decreasing dustiness
GC49
(23°N)
ODP 658C
(21°N)
Decreasing dustiness
Increasing dustiness
GC68
(19°N)
YD
H1
H2
H3
H4
H5
H5a
H6

The ODP 658C record shows remarkable similarity to the dust flux record covering the last 70 ka from the Mid-Atlantic at 25°N (Middleton et al., 2018), both in overall trends and millennial-scale variability (Figure 2-4). Both records exhibit a background increase in dustiness throughout MIS3, a large decrease during the AHP, and peaks in dust flux during Greenland stadials. There are two distinct times of disagreement between the records, namely during the AHP through the late Holocene, and from 50-60 ka. The Mid-Atlantic record has an AHP which has a more gradual onset following the YD, and ends 2 ka later than in the ODP 658C record. From 50-60 ka the ODP 658C record exhibits much higher variability with fluxes reaching both their maximum and minimum levels of the whole 67 ka record. The disagreement at the end of the AHP is most likely age model based, as sedimentation rates are much lower at distal open ocean locations compared to proximal locations situated in the vicinity of an upwelling area. From 50-60 ka a similar structure in dust flux is seen between the records, and therefore the disagreement in relative amplitude of fluxes within each core may also be a consequence of low sedimentation rates at the Mid-Atlantic site. Average sedimentation rates are 2 cm/ka in the Mid-Atlantic site, whereas the ODP 658C site has an average sedimentation rate eight times this rate at 16 cm/ka. The high amplitude and abrupt "W-shape" changes in dust flux are well resolved due to the high sedimentation rates at the ODP 658C site (Figure 2-4), whereas the amplitude of these abrupt changes may have been smoothed due to the much lower sedimentation rate and thus greater influence of mixing by bioturbation at the Mid-Atlantic site. These times of disagreement highlight the importance of a high sedimentation rate core site to capture the full magnitude of dust export changes during times of millennial-scale variability. The agreement with the Mid-Atlantic dust record, which lies thousands of miles downwind of African dust sources, builds confidence that the influence of sea-level variations is minor on the more proximal ODP 658C record. Therefore, the ODP 658C dust record is representative of an integrated signal of African dust export to the North Atlantic over the past 67 ka.

These records provide millennial-scale reconstructions of the flux of dust to the NW African margin over a timescale three times longer than that of previous high-resolution work, allowing further comparison of these dust flux records to high- and low-latitude climate records to explore relationships and drivers of North African climate. We now explore the implications of our new dust records by comparing them with high-latitude Northern Hemisphere records, summer insolation, and other records of North African climate.

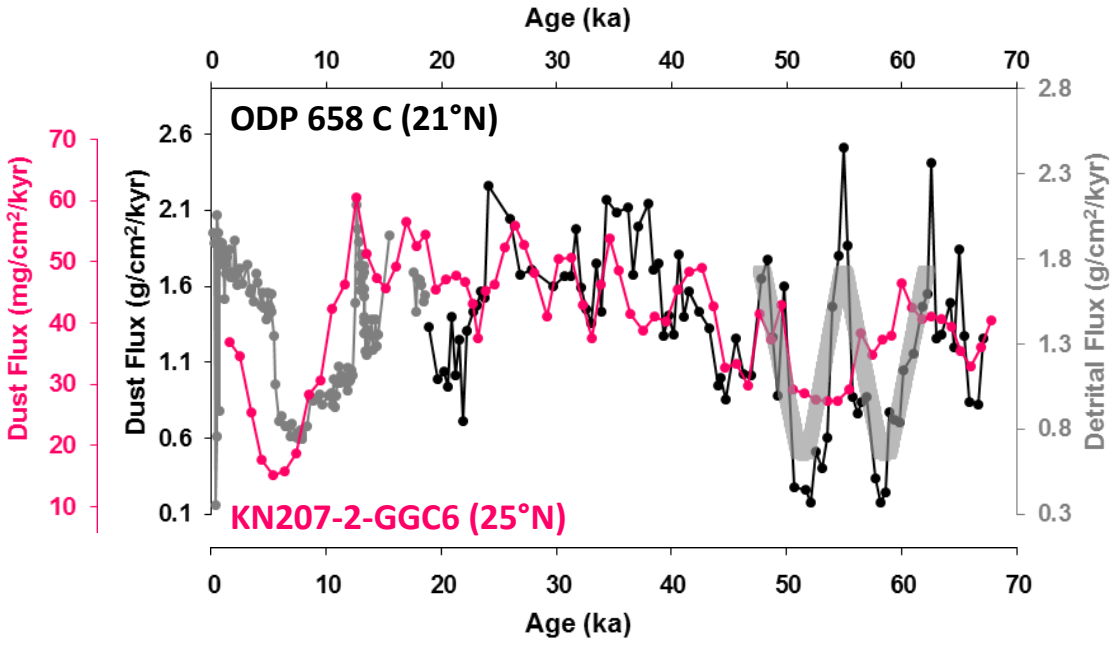

Figure 2-4. ODP 658C dust and detrital flux (black and grey lines, respectively) and KN207-2-GGC6 dust flux from the mid-Atlantic (Middleton et al., 2018) (pink line) records. Data <20 ka in ODP 658C from Adkins et al., (2006). "W-shape" structure of the dust flux record as referred to in main text is illustrated by a transparent w-shape from ~60-50 ka.

2.5.2 Links Between High-Latitude Climate and NW African Climate During MIS 2 through 4

In previous work focusing on the past 20 ka, North African hydroclimate has been shown to respond sensitively to high-latitude North Atlantic stadial cooling events, with millennial-scale dust flux increases along the margin during H1 and the YD. We use the extended CHEETA and ODP 658C dust records to explore the relationship between high-latitude climate and the dust expression of North African hydroclimate to the NW African margin during MIS 2 through 4, a time of sustained Northern Hemisphere ice and cooler temperatures than in modern times.

We begin by describing the broader-scale features of the records before turning to millennial-scale variability. At the onset of MIS 3 (around 60 ka) Northern Hemisphere temperatures increase, and during this time dust fluxes in ODP 658C drop to values comparable to those during the AHP (a direct comparison of dust fluxes is not possible because Adkins et al. (2006) reported total detrital fluxes, providing only an upper bound on dust fluxes). Over the next 30 ka, Northern Hemisphere high-latitude temperatures reflected in Greenland ice core records decrease gradually to minimum values between 30 and 25 ka, with multiple millennial-scale stadials superimposed on the background decrease (Figure 2-5). Dust fluxes over this interval show a gradual increase to sustained high values during MIS 2 and 3, with millennial-scale pulses of high dust flux superimposed on the background increase.

During MIS 2 Northern Hemisphere high-latitude temperatures (Seierstad et al., 2014) gradually increase after 24 ka leading into the LGM time slice commonly targeted for data-model comparisons (19-23 ka) (e.g., Waelbroeck et al., 2009). Dust fluxes over this interval decrease from the high values observed at the end of MIS 3 and beginning of MIS 2; as a result, the LGM is characterized by North African dust deposition rates that appear roughly similar to late Holocene fluxes. The broad scale features of the dust records from the end of MIS4 through the end of MIS2 show a strong correspondence over this interval between high latitude temperatures and dust fluxes to the margin, with lower temperatures associated with higher fluxes to the margin and higher temperatures associated with lower fluxes to the margin.

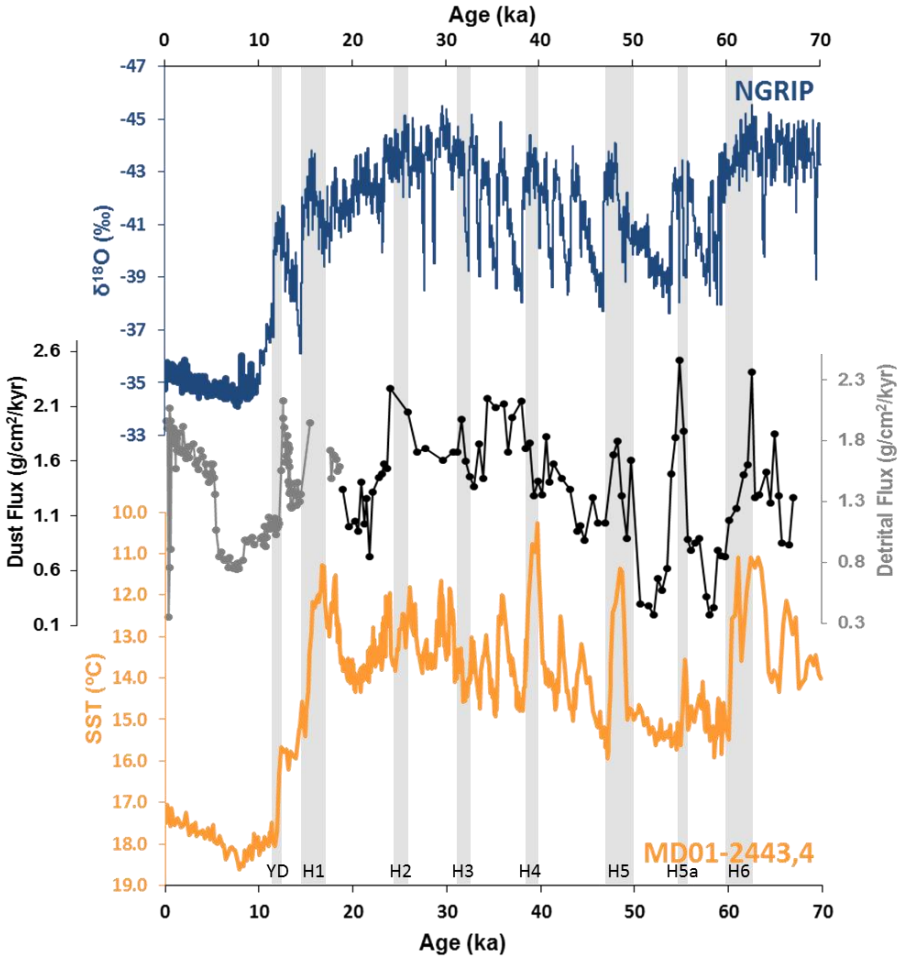

Figure 2-5. NGRIP $\delta^{18}O$ from Seierstad et al., (2014) (blue line), ODP 658C dust and detrital fluxes (black and grey lines, respectively), and MD01-2443,4 SST from Martrat et al., (2007) (orange line) records. Data <20 ka in ODP 658C from Adkins et al., (2006).

The high sedimentation rates and well-resolved radiocarbon-based age model for GC68 allows a more detailed comparison between dust flux variability and millennial-scale high latitude climate records over the last 26 ka. The millennial-scale features in the GC68 dust flux record associated with high-latitude climate fluctuations during H1, the Bølling-Allerød warm period, and the YD, previously described by McGee et al., (2013), show strong coherence between North Atlantic stadials and high fluxes of dust to the West African margin. Comparison of the earlier highly-resolved 26.5-20 ka portion of the GC68 flux record (Figure 2-6) with a proxy record of North Atlantic SSTs (Cacho et al., 1999) reveals that the three cold events at 25 ka, 24 ka (H2) and 21 ka are all associated with increases of dust flux to the margin. The amplitudes of dust flux over this interval do not have a clear correspondence with amplitude of SST (i.e. the largest dust flux peak does not occur at the time of coldest SST), which could be caused by variable bioturbation and smoothing of the peaks in the two records.

As the GC68 cored material ends at 26.5 ka, the older material from CHEETA cores GC37 and GC49, and ODP Core 658C can be examined and compared over a longer time period on a millennial-scale with high-latitude climate records. An examination of millennial-scale dust variability in these three cores reveals peaks of dust flux likely associated with millennial-scale North Atlantic stadial events. At 60 ka there is a pronounced stadial (including Heinrich event 6) in the North Atlantic with an accompanying millennial-scale peak in which dust fluxes at ODP 658C more than double. This signal of increased dust during stadials with associated Heinrich events is a robust response, with dust increases seen at H5a, H5, H3, and H2. The exception to this is H4 which occurs at a time in ODP 658C where dust is at a minimum; we suggest that this mismatch is due to age model error (see Appendices 2.A), and that the subsequent dust flux peak is a response to H4. A similar mismatch is evident in the mid-Atlantic record of Middleton et al. (2018). There are also stadial events (without accompanying H events) with pronounced peaks in flux of dust to the margin at 42 ka and 37 ka, showing that increased export of dust is observed during stadials both with and without H events. There are multiple instances in which stadials are observed in the SST record without discernible increases in dust flux (67 ka, 47 ka, 30 ka), perhaps due to aforementioned age model error, or increased smoothing by bioturbation during times of lower sedimentation rates (see Appendices 2.C).

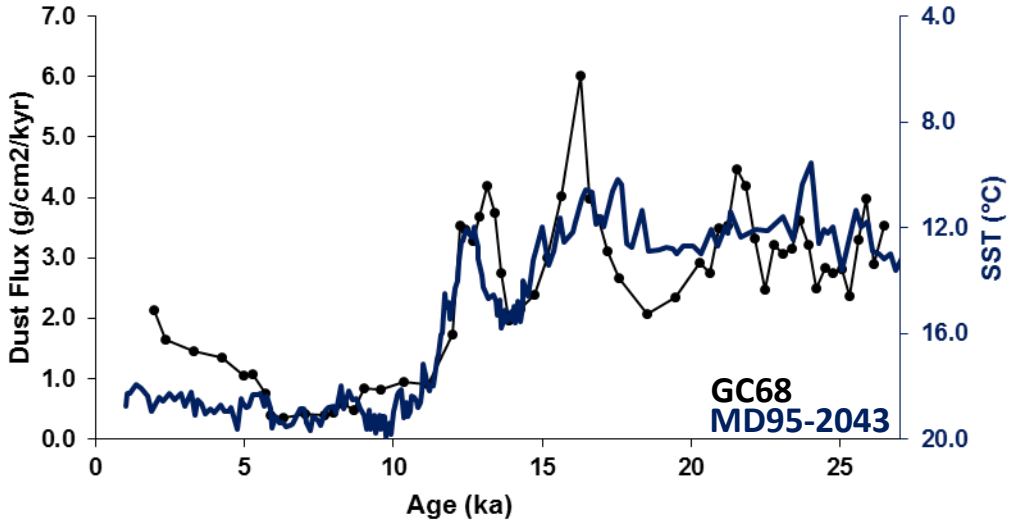

Figure 2-6. GC68 dust flux (black line) and MD95-2043 SST from Cacho et al., (1999) (blue line) records. Data <20 ka in GC68 from McGee et al., (2013).

Based upon the strong coherence between millennial-scale peaks in dust flux in our most robust record (GC68) with stadials in the North Atlantic, we suggest that the millennial-scale peaks in the longer dust flux records (ODP 658C, GC49, GC37) correspond to the millennial-scale stadial events in the North Atlantic SST records, and that any mismatches are likely due to issues with smoothing and age control. This conclusion, which could be strengthened by additional records with consistently high accumulation rates as in CHEETA core GC68, suggests that the impact of Heinrich events on West African climate was largely stable across varying orbital configurations and ice sheet extents during MIS2, 3, and 4.

The dust records reveal changes to hydroclimate and atmospheric circulation over the past 67 ka, and can aid in building a picture of climate changes over North Africa during this interval. Murphy et al. (2014) suggest that in areas that are already dry and dust producing like the Sahara, the only way to increase dust export is through an increase in wind speed; this conclusion is supported by studies supporting the dominant role of winds in modern decadal variability in Saharan dust emissions (Ridley et al., 2014; Wang et al., 2015). Consistent with this conclusion, our records show strong covariation of opal and organic carbon fluxes with dust fluxes throughout most of our records (Figure 2-7), providing firm evidence for intensification of northeasterly winds as a driver of increases in both coastal upwelling and dust deposition during stadials (Bradtmiller et al., 2016; McGee et al., 2018). A modeling study by Liu et al. (2014) highlights the importance of these wind anomalies in communicating stadial conditions to the West African monsoon, demonstrating that anomalous northeasterly winds resulting from high-latitude cooling advect cold, dry air into North Africa, weakening the west African monsoonal circulation and drying the Sahel. This cold air advection is amplified by water vapor feedbacks, which further cool the Sahara and raise surface pressures, increasing northeasterly winds even more (Liu et al., 2014). Our dust and biogenic flux records thus provide support for Liu et al.'s ventilation mechanism as a driver of the reductions in Sahel rainfall suggested by proxy data during stadials (e.g., Weldeab et al., 2007).

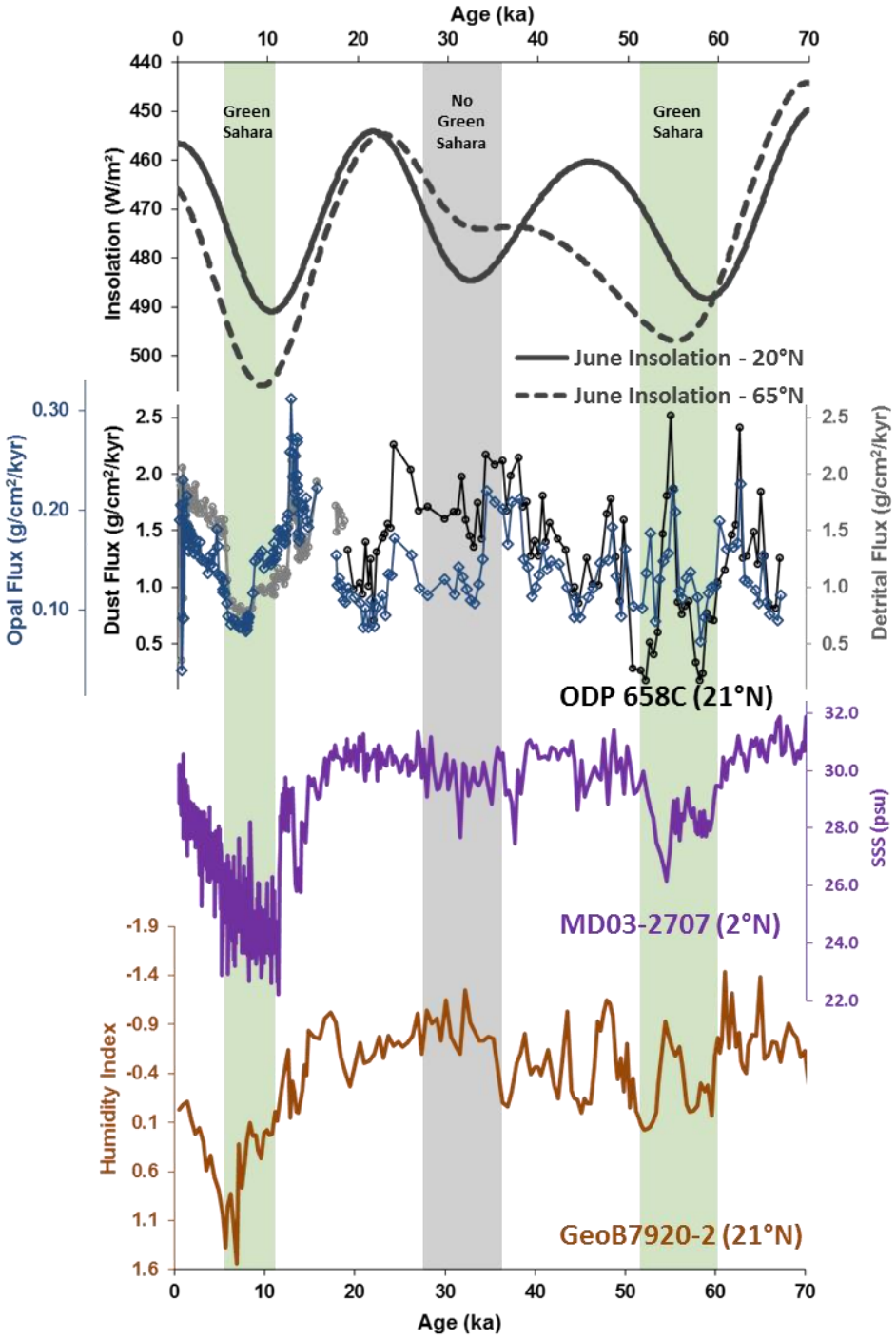

Figure 2-7. June insolation at 20°N and 65°N from Laskar et al., (2004) (dark grey solid and dark grey dashed lines, respectively), ODP 658C dust and detrital flux (black and light grey lines with open circles, respectively), MD03-2707 SSS from Weldeab et al., (2007) (purple line), and GeoB7920-2 Humidity Index from Tjallingii et al., (2008) (brown line) records. Data <20 ka in ODP 658C from Adkins et al., (2006).

2.5.3 Relationship Between Summer Insolation and NW African Climate During MIS 2 through 4

The impact of precessionally-paced changes in summer insolation on North African climate have been clearly documented in records of the last 20 ka. In NW African dust records, the response to the most recent ~20 kyr precessional cycle can generally be summarized as a transition from low summer insolation/high dust at the end of the LGM, to high summer insolation/low dust during the AHP (11-5 ka), to low summer insolation/high dust in the late Holocene (e.g., Adkins et al., 2006; deMenocal et al., 2000; McGee et al., 2013; Tjallingii et al., 2008; Williams et al., 2016). The low dust fluxes of the AHP occur in association with diverse proxy evidence of a "Green Sahara" interval with much higher rainfall supporting diverse vegetation, permanent lakes, and human populations (Gasse, 2000; Jolly et al., 1998; Kuper & Kröpelin, 2006; McGee & deMenocal, 2017; Tierney et al., 2017). We use the extended CHEETA and ODP 658C dust records to explore the relationship between summer insolation and dust emissions during MIS 2 through 4, allowing examination of insolation change over two additional cycles of orbital precession.

In the new extended ODP 658C dust record extremely low dust fluxes are observed during the insolation maximum centered on 55 ka (Figure 2-7). The values seen in terms of detrital flux are even lower than those recorded during the Green Sahara interval at 11-5 ka. The expression of the 60-50 ka low dust event differs from the AHP, however, in that it is punctuated by an abrupt millennial-scale increase in dust at 55 ka. Dust fluxes begin high at 60 ka (1.5 g/cm^3), decrease by a factor of three at 58 ka (0.5 g/cm^3), increase dramatically at 55 ka (2.5 g/cm^3), decrease to minimum values again at 52 ka (0.5 g/cm^3), before increasing gradually throughout the next 15 ka. This high dust flux event has been described above as associated with a North Atlantic stadial, an indication that high-latitude climate can exert a strong influence on African climate even during a time of high summer insolation and a strong West African monsoon.

Comparison of the dust flux record at 60-50 ka with other paleoclimate archives of North African climate allows further probing of the structure of the Green Sahara event and how the interplay of high-latitude climate forcing with high summer insolation affects North African hydroclimate. The

"W-shape" structure observed in the ODP 658C dust record is also observed in Sea Surface Salinity (SSS) reconstructions in the Gulf of Guinea (Weldeab et al., 2007) and continental humidity reconstructions off Cape Blanc (Tjallingii et al., 2008) suggesting a wetter African interior. The "W-shape" structure in these records differ however from the dust record, as they show wetter conditions following the 55 ka stadial event, while the dust record shows equal magnitude dust flux minima preceding and following the stadial. The salinity and grain size records both show their maximum proxy values of inferred wet conditions during the 11-5 ka interval, while the detrital flux record of ODP 658C shows maximum values of inferred wet conditions during the 60-50 ka time slice comparable to that of the 11-5 ka interval. Future work will be required to explore the variable expression of this MIS3 Green Sahara period in different regions of North Africa using different proxies.

Dust export to ODP 658C during the local summer insolation maximum from 28 to 35 ka has no discernible minimum in flux, as dust flux remains relatively high throughout this time at 1.5 g/cm^3, unlike the dust minima seen during the previous insolation maximum/Green Sahara interval from 60 to 50 ka, and the following insolation maximum/Green Sahara interval from 11 to 5 ka. The expression of this interval of insolation maximum (28-35 ka) in other records of North African hydroclimate is also as a time of aridity, with very high sea surface salinity (low freshwater runoff from North Africa) in the Gulf of Guinea (Weldeab et al., 2007) and very low humidity index (high ratio of eolian to fluvial sediments) in sediments near ODP 658C (Tjallingii et al., 2008). Skonieczny et al. (2019) similarly highlighted "skipped beats" of insolation during the last two glacial periods. In contrast, fluxes of C_{org} and opal decrease by a factor of ~2 over this time interval (Figure 2-7), but do not reach the minima observed in the earlier Green Sahara interval for both proxies, or during the AHP for opal. This discrepancy, with dust fluxes staying relatively high throughout the insolation maximum while biogenic proxies decrease, may reflect a decrease in wind strength without a substantial decrease in aridity. Alternatively, it may be that there are precessionally paced changes in the nutrient content of upwelled waters or effects on upwelling and productivity from changing shelf morphology due to sea-level lowering.

The latter part of this arid interval is coincident with the coldest high latitude temperatures during the past 70 ka as measured in Greenland ice, and the coldest North Atlantic SSTs. The precessional

beat of maximum local summer insolation at 35-28 ka thus occurs during a colder interval with higher ice volume than the preceding and subsequent Green Sahara intervals, suggesting that high latitude forcing during a time of high ice volume and cold temperatures may override the impact of increased summer heating of North Africa on the monsoon, keeping North Africa arid. Alternatively, the arid interval at 35 to 28 ka could be caused by reduced heating of high-latitude Northern Hemisphere continents, as this precessional extreme occurs at a time of low obliquity. Summer insolation at 65°N remains relatively low at ~30 ka, indicating a strengthened heating gradient in the Northern Hemisphere during this beat of insolation, potentially causing the lack of monsoon strengthening and greening of the Sahara as seen during the other summer insolation maxima. Modeling by Singarayer et al., (2017) appears to support the first suggestion. In their simulations, the summer rain belt over North Africa reaches similar latitudes during the summer insolation maxima at ~35 ka and ~55 ka when only orbital parameters and greenhouse gases are changed, but the rain belt is substantially farther south at 35 ka when ice sheets are included in the simulation.

2.6 Conclusions

Extended dust flux records from 19°N to 27°N along the West African margin show a coherent signal of dust export during overlapping intervals, from 37 ka to present in cores GC37, GC49, and ODP 658C, and additionally in core GC68 from 26 ka to present. These records show a peak in dust at 35-33 ka, with fluxes decreasing throughout MIS 2; these multi-millennial trends appear to correlate with high-latitude temperature changes indicated by Greenland ice cores, with dust peaking during the coldest conditions. Due to the decline in dust fluxes in MIS2, the LGM time slice commonly targeted in modeling experiments is marked by relatively moderate dust fluxes, with dust deposition similar to modern levels in most cores despite much steeper pole-to-equator temperature gradients.

There is also coherent millennial-scale variability throughout our records. In core GC68, which has the highest accumulation rates and best-constrained age model in MIS2, millennial-scale dust peaks correspond with reductions in North Atlantic SSTs. At other sites, most stadial events—including H2, H3, H5, H5a, and H6—correspond to periods of high dust fluxes. Due to this strong

coherence, we suggest that the few intervals in which high dust fluxes are not observed at the same time as low SSTs result from age model errors and/or bioturbation. Covariation of dust fluxes with fluxes of opal and organic carbon, taken here to represent coastal upwelling intensity, suggests that dust flux variations occur in association with (and are likely driven by) changes in northeasterly wind strength. This finding provides support for the role of northeasterly winds in ventilating the West African monsoon during stadial events, leading to the observed decreases in Sahel precipitation.

The longer dust flux record from ODP 658C reveals a "Green Sahara" interval at 50-60 ka marked by low dust fluxes. This period corresponds to a time of high NH summer insolation and relatively warm North Atlantic SSTs, suggesting a strong West African monsoon even in the presence of extended ice sheets and moderate atmospheric CO_2 concentrations. This interval differs from the AHP (11-5 ka), as there is a millennial-scale peak in dust flux during the interval that appears to correspond to H5a. The low latitude insolation maximum at 35 ka is a "skipped beat", in that there is no record of a strengthening of the West African monsoon and decrease in dust flux during this time, potentially due either to an increased gradient in insolation during this time of low obliquity, or to the influence of cold North Atlantic temperatures and large ice sheets in counteracting the local insolation forcing on North African climate.

Appendices

2.A ODP 658C Age Model

The MIS3 interval has a lower confidence age model compared to the younger portions of the records. During MIS3 ^{14}C-ages are infrequent and uncertainties are larger as age increases; in addition, the oldest portion of the ODP 658C age model is constructed from tie points to a nearby $CaCO_3$ % record (Tjallingii et al., 2008) lacking fine-scale age control (Figure 2-8).

2.B Grain Size Endmember Distributions

The MATLAB routine developed by McGee et al. (2013) was used on grain size measurements on the terrigenous fraction of ODP 658C samples to determine the Weibull distributions for three endmembers that provided the best fit to the grain size distribution, by minimizing the root-mean-square (RMS) deviation between the modeled and measured distributions (Figure 2-9).

2.C Sedimentation Rates

When probing the older ODP 658C, GC49, and GC37 records at millennial timescales lower sedimentation rates (Figures 2-10 and 2-11) mean core material is more susceptible to bioturbation and smoothing of climate signals.

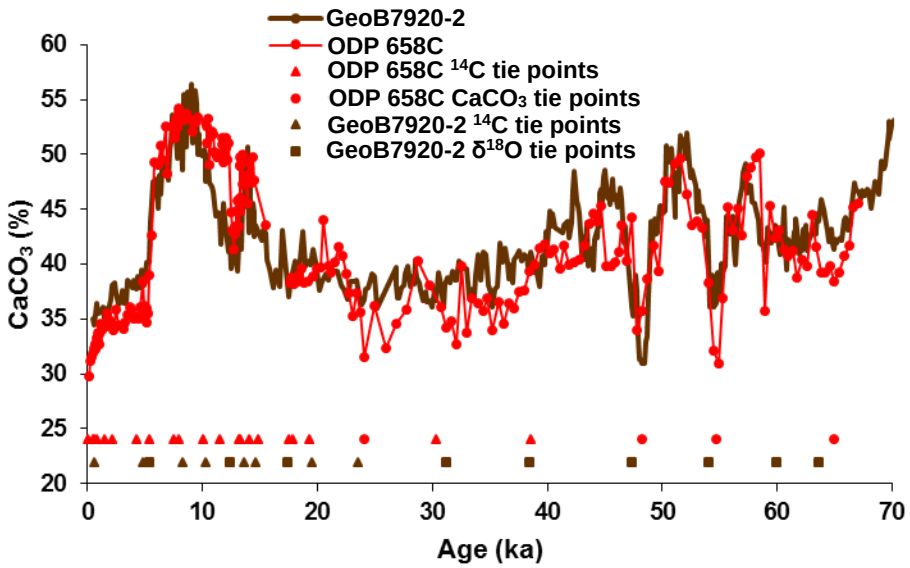

Figure 2-8. Comparison of calibrated XRF $CaCO_3$ Wt. % (brown line) from GeoB7920-2 with $CaCO_3$ Wt. % (red line) from ODP 658C. Red circles indicate tie points between the two records.

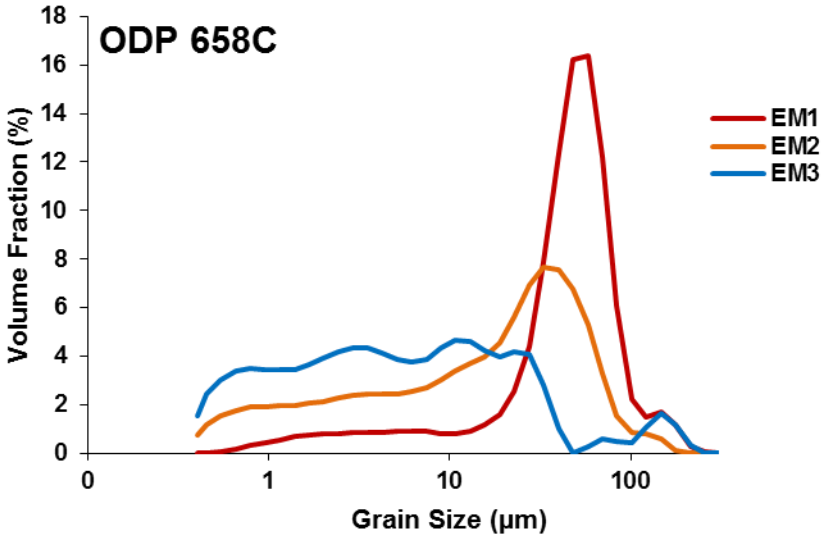

Figure 2-9. Endmember distributions in core ODP 658C.

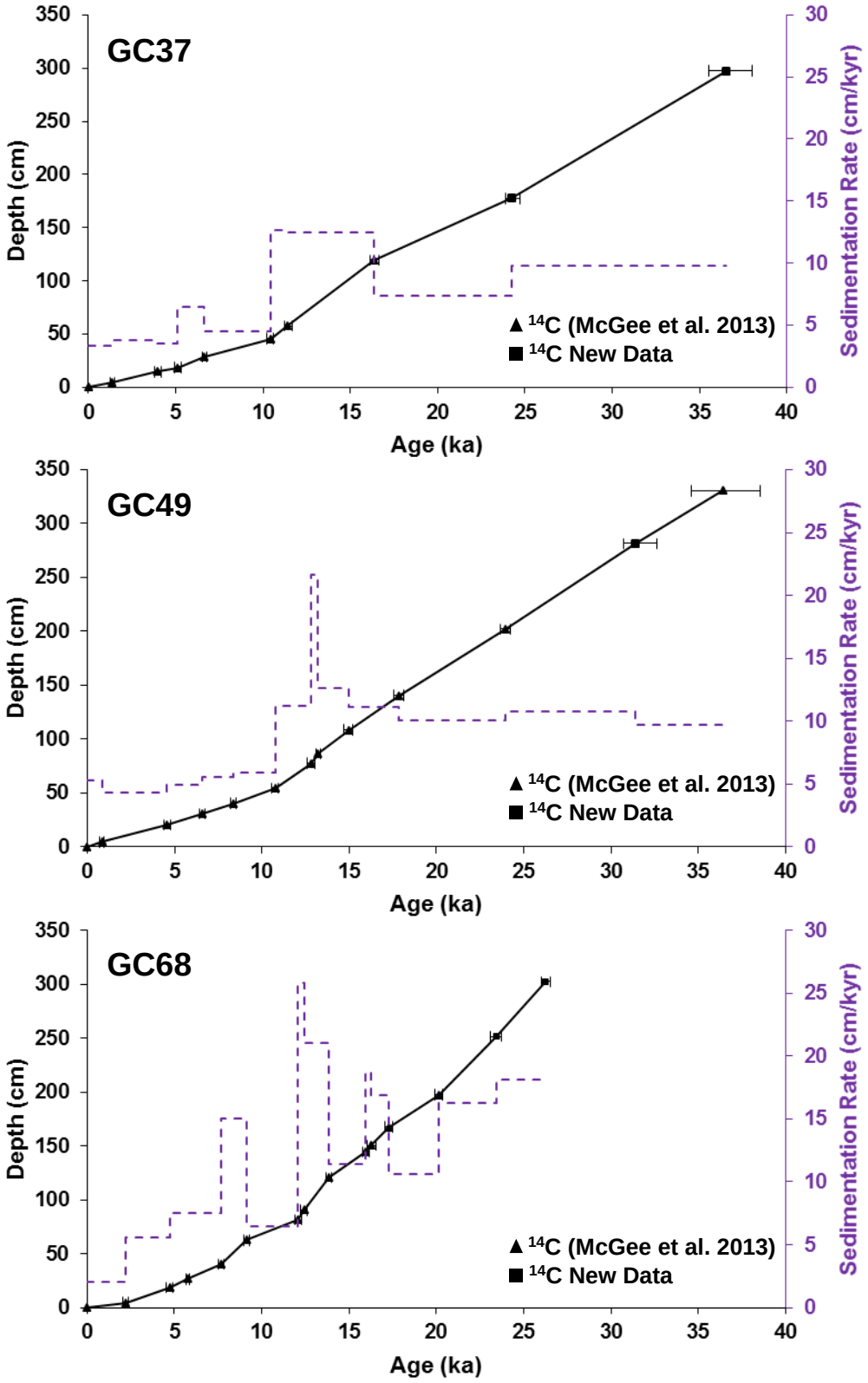

Figure 2-10. Age-depth plot and sedimentation rates for GC37, GC49, and GC68. 95% confidence intervals on calibrated ^{14}C ages are shown.

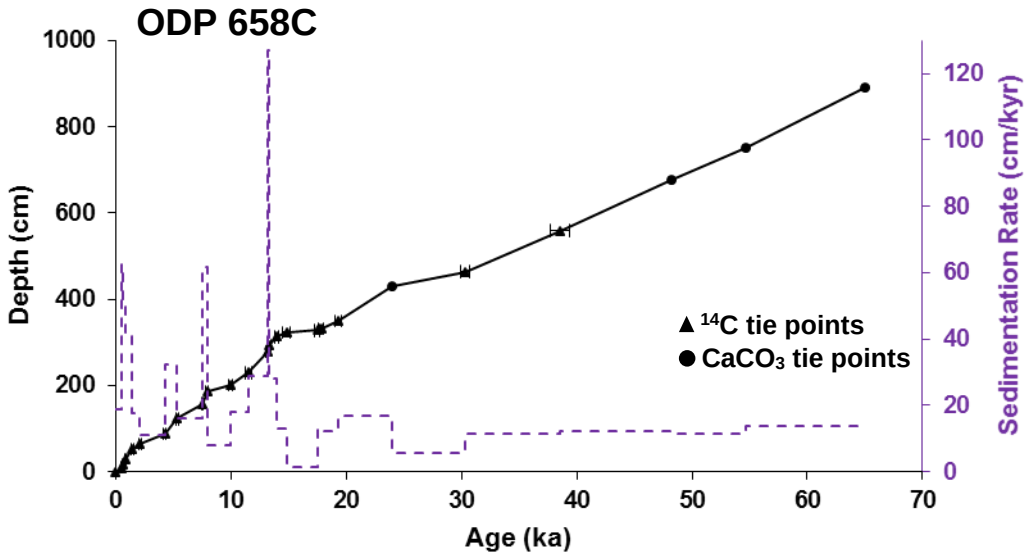

Figure 2-11. Age-depth plot and sedimentation rates for ODP 658C. 95% confidence intervals on calibrated ^{14}C ages are shown.

Chapter 3

North Pacific Dust Fluxes at ODP Site 1208 (Shatsky Rise) Over the Last 330 ka

3.1 Abstract

ODP Site 1208 is located on the Central High of Shatsky Rise in the midlatitudes of the western North Pacific Ocean, under the core of the Asian dust plume. We present a high resolution $^{230}Th_{xs}$-normalized dust flux record from the site over the last 330 ka to determine the effects of glacial-interglacial and orbital variability on atmospheric circulation and dust export from Asian source areas. We observe a clear glacial-interglacial signal with dusty glacials, and low dust fluxes during interglacials, with evidence for a precessionally-driven insolation control overriding the glacial-interglacial signal. This is most clear during glacial times where decreases in dust flux occur during maxima in June 21st insolation at 65°N, potentially driven by changes to the length of the dust season in East Asia, or less intense dust storms. We compare our record over the last 150 ka with other dust records from the western North Pacific to form a transect of $^{230}Th_{xs}$-normalized dust flux records spanning 0.5-50 °N. The transect shows that glacial-interglacial variability in dust supply varied coherently across the whole western North Pacific, suggesting that dust transport mechanisms did not vary over this timescale. The equatorial record shows more muted variability relative the midlatitude and subarctic records on orbital timescales, suggesting a change in dust transport across the North Pacific which does not reach the equator.

3.2 Introduction

In the modern climate dust is generated from Central Asian source areas during outbreak events prevalent in springtime due to strong temperature gradients and lee cyclogenesis (Roe, 2009), lofted and entrained into the atmosphere, and exported by the Westerly Jet, predominantly in spring dust storm events. As climate changes the impact on dust source areas, timing of seasonal

transitions, and atmospheric transport dynamics alters the long-range transport of Asian dust to the North Pacific and beyond. Thus dust records from North Pacific sediment cores can be utilized to reconstruct changing emission of dust from Asian sources as climate changes on glacial-interglacial, orbital, and millennial timescales. However dust records spanning multiple glacial-interglacial cycles from the midlatitude North Pacific are limited to those containing dust flux estimates based on linear sedimentation rates (e,g,, Hovan et al., 1991), which have been shown to contain potential biases due to the low resolution nature of age-depth tie points that the sedimentation rates are based on (e.g., Skonieczny et al., 2019).

We utilize sediments from ODP Site 1208 on Shatsky Rise, which is directly underneath the transport path of the Asian dust plume, to reconstruct $^{230}Th_{xs}$-normalized dust fluxes to the midlatitude North Pacific over the last 330 ka using. With the combination of published $^{230}Th_{xs}$-normalized dust records we map western North Pacific dust fluxes from the equatorial to subarctic North Pacific to examine dust export to the North Pacific from Asia on glacial-interglacial and orbital timescales.

3.3 Methods and Core Site

3.3.1 Core Location and Age Model

ODP Site 1208 was cored on ODP Leg 198 (Shipboard Scientific Party, 2002a) close to the center of the Central High of Shatsky Rise in the western North Pacific Ocean (36°7.630'N, 158°12.095'E), at 3346 meters water depth (Figure 3-1). The sampled core sections consist of a dark yellowish brown clay with nannofossils, followed by mainly olive gray nannofossil clay to clayey nannofossil ooze (Shipboard Scientific Party, 2002b).

The age model for ODP Site 1208 (Figure 3-2) was developed by tuning a benthic oxygen isotope record from the site to the LR04 benthic $\delta^{18}O$ stack profile (Lisiecki & Raymo, 2005) using ten tie points.

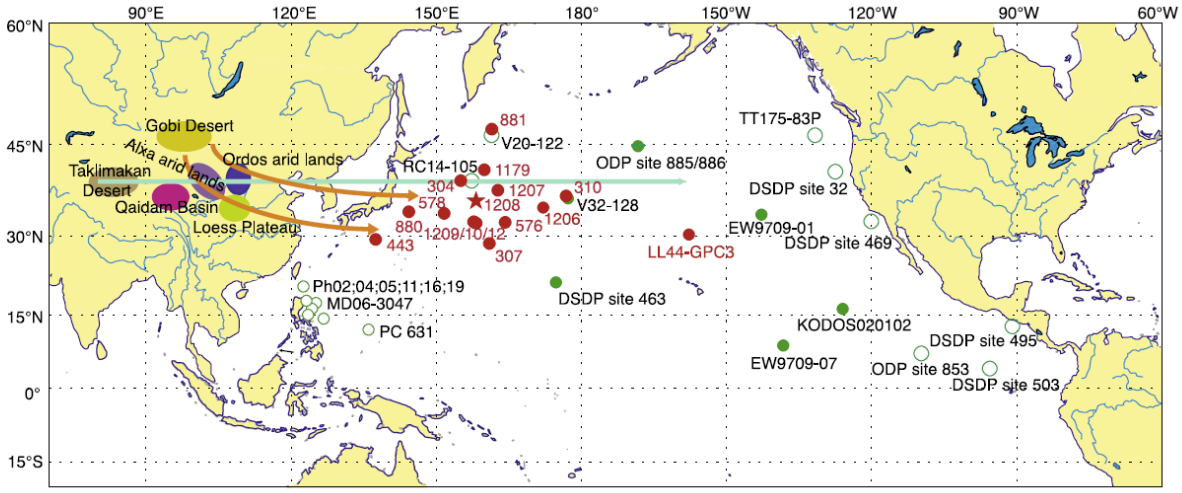

Figure 3-1. Map showing ODP Site 1208 in the North Pacific Ocean (red star) (36°7.630'N, 158°12.095'E) from Zhang et al., (2016). The site is located at 3346 m water depth, close to the center of the Central High of Shatsky Rise (Shipboard Scientific Party, 2002).

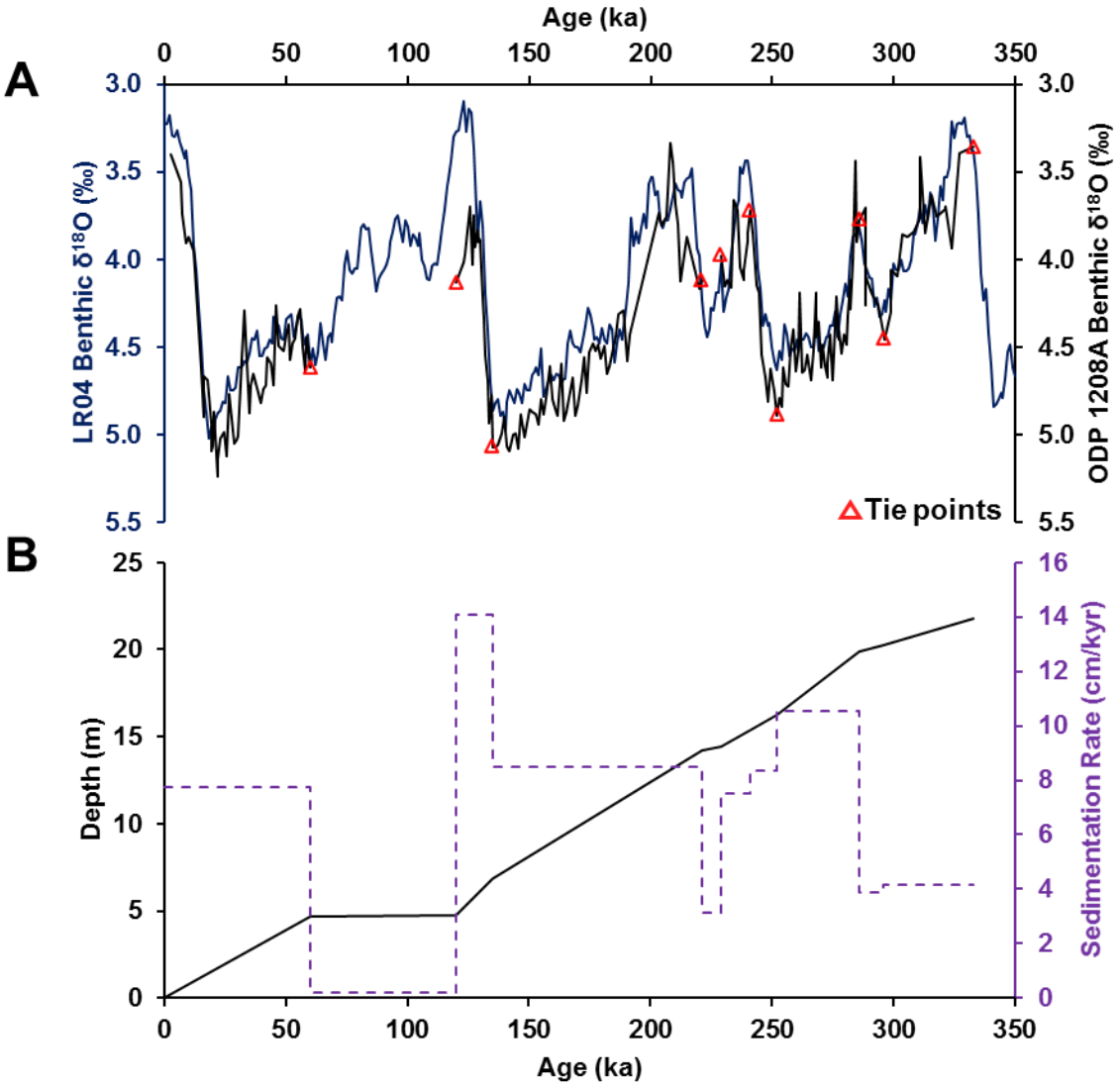

Figure 3-2. Panel A: ODP Site 1208 benthic oxygen isotope record plotted with tie points (red triangles) to the LR04 stack (Lisiecki & Raymo, 2005). Panel B: Age-depth plot and sedimentation rates for ODP Site 1208.

3.3.2 Geochemistry Methods

Eolian fluxes were calculated by multiplying the eolian fraction of the sediments by the vertical sediment flux, which was calculated using $^{230}Th_{xs}$-normalization (Bacon, 1984; Suman & Bacon, 1989) (see Chapter 2.3.4). The eolian fraction of the sediments was calculated by assuming all ^{232}Th was sourced from eolian material with an average ^{232}Th concentration of 14 μg/g (McGee et al., 2016). The samples were measured at MIT in separate runs for each isotope system (U, Th) on a Nu Plasma II-ES MC-ICP-MS. Each sample was bracketed by a standard in order to correct for mass bias drift.

Uncertainties in the final eolian fluxes are reported as 1 sigma error bars and reflect confidence limits associated with mass spectrometric measurements, the detrital U/Th ratio, and the eolian fraction of the sediments.

3.4 Results

A high resolution dust flux record was constructed for ODP Site 1208 spanning the last three glacial-interglacial cycles to 330 ka (Figure 3-3; see Appendix B for the data). Two core gaps exist from 229 to 221 ka, and from 120 to 60 ka, and are found at the transition depths between sediment cores 1208A-3H and 1208A-2H, and 1208A-2H and 1208A-1H respectively, indicating likely loss of core material during drilling. The dust flux record shows a general trend of dusty glacials, and low dust during interglacials.

Dust fluxes in ODP 1208 increase from the lowest recorded value over the record of 0.1 g cm^{-2} kyr^{-1} at MIS 9 (320 ka) to a maximum of 0.6 g cm^{-2} kyr^{-1} in the early portion of MIS 8 (280 ka). Fluxes decrease to 0.3 g cm^{-2} kyr^{-1}at 260 ka and remain relatively low throughout MIS 7. Dust fluxes begin to gradually rise at 200 ka to 0.6 g cm^{-2} kyr^{-1}, and then vary between 0.4-0.6 g cm^{-2} kyr^{-1} from 195 to 135 ka, spanning most of MIS 6. Fluxes exhibit an abrupt drop to 0.25 g cm^{-2} kyr^{-1} at the onset of MIS 5 (130 ka). Following the core gap from 120 to 60 ka, dust fluxes reach the highest sustained maximum values of the record of 0.7 g cm^{-2} kyr^{-1} during MIS 4, before dropping abruptly to 0.4 g cm^{-2} kyr^{-1} throughout MIS 3. Dust fluxes show a moderate increase at

the onset of MIS 2 (29 ka) to 0.6 g cm^{-2} $kyr^{-}1$, and fall from the onset of MIS 1 throughout the Holocene to a value of 0.2 g cm^{-2} kyr^{-1} at 0.3 ka.

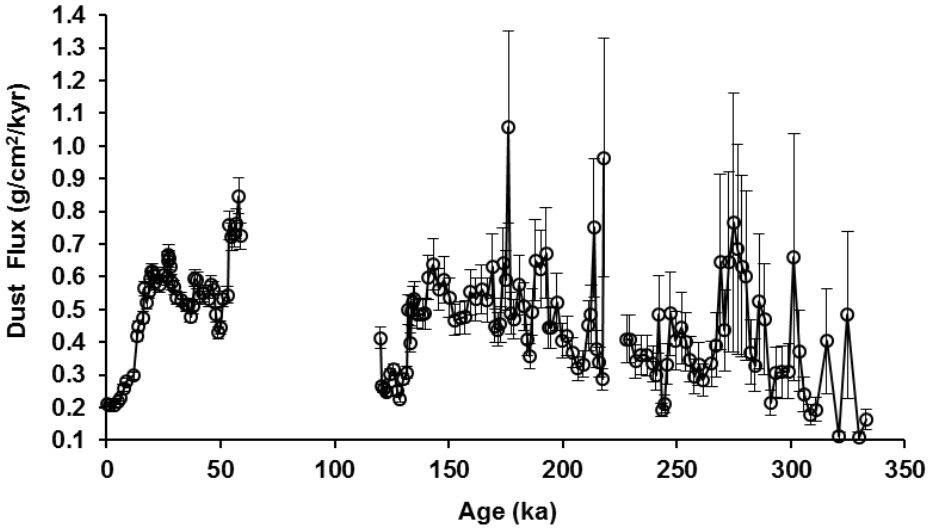

Figure 3-3. ODP Site 1208 dust flux record (black line, open circles) with 1σ uncertainties.

3.5 Discussion

This work has generated the first $^{230}Th_{xs}$-normalized dust record from the midlatitudes of the western Pacific Ocean at ODP Site 1208 on Shatsky Rise, situated within the heart of the Asian dust plume, spanning the last three glacial-interglacial cycles (330-0 ka). To assess the reliability of the ODP 1208 record given the significant core gaps at 229-221 ka and 120-60 ka we compared the dust flux record at a nearby sediment core site, V21-146, located on the Northern High of Shatsky Rise (37°41'N, 163°02'E) (Hovan et al., 1991). The V21-146 dust flux record is at a lower resolution than the ODP 1208 record, with flux measurements calculated using linear sedimentation rates rather than $^{230}Th_{xs}$-normalization, but crucially displays a continuous record for the last 330 ka. Considering the differing methodology in calculation of the fluxes, the two records show remarkable agreement in the absolute values and amplitudes of change to dust fluxes (Figure 3-4). The records also show strong coherent agreement in the overall trends in dust flux they display, with dusty glacials and lower fluxes during interglacials, with some offsets in timing of events (e.g., the dust flux peak at 280 ka during MIS 8) likely due to uncertainties in the older age model of V21-146. The higher resolution record at ODP 1208 contains some features not present in the V21-146 record, for example during the low flux interval from 250-210 ka in the V21-146 record there is an orbital-scale dust flux peak from 250-240 ka in the ODP 1208 record. The good agreement between the ODP 1208 and V21-146 dust flux records where there are overlapping samples over the last 330 ka gives confidence that the ODP 1208 record can be utilized as a reliable midlatitude western Pacific Ocean dust flux record during this time, despite the existing gaps in the record.

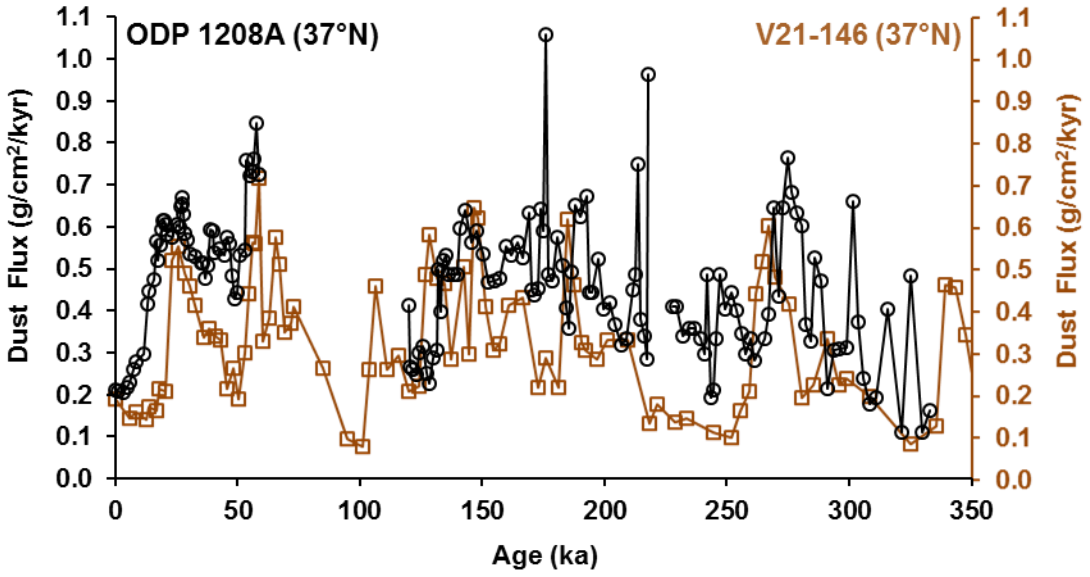

Figure 3-4. Dust flux record comparison from two sites on Shatsky Rise. V21-146 (brown line, open squares) is located on the Northern High of Shatsky Rise (37°41'N, 163°02'E; 3968 m water depth) (Hovan et al., 1991), while ODP Site 1208 (black line, open circles) is located on the Central High. The records show good agreement in broad trends, but differ in timing of some millennial-scale events and magnitude over the whole record.

Recent work in dust reconstruction utilizing $^{230}Th_{xs}$-normalization from the western North Pacific has generated records from the subarctic North Pacific at ODP Site 882 (50.4°N, 167.6°E; Serno et al., 2017) and the equatorial North Pacific at site ML1208-17PC (0.48°N, 156.45°W; Jacobel et al., 2017) spanning the last 150 ka. The ODP 1208 dust flux record thus adds to this meridional transect with a record from the midlatitudes at 37°N, within the heart of the Asian dust plume, allowing for a more complete view of the history of dust export to the North Pacific over the last 150 ka. To aid in comparison the North Pacific dust flux records from each of these three sites, forming a meridional transect from 50.4-0.48 °N, are plotted relative to the average dust flux over the length of each record as the amplitude changes in flux and absolute flux values are markedly different in each record (Figure 3-5). The three records show broad scale similarities in trend on glacial-interglacial timescales with high dust fluxes during glacials (MIS 6 and MIS 2), transitions to low fluxes during the last two glacial terminations at MIS 6/MIS5e (130 ka) and at MIS 2/MIS 1 (18 ka). This implies that dust variability across the whole of the N Pacific varies coherently on G-IG timescales, at least over the last G-IG cycle, suggesting that dust transport mechanisms did not change over these timescales. However the amplitude of variability on orbital timescales varies across the records, with the equatorial Pacific record exhibiting muted variability over most of the record, except during the end of MIS 6 where the record reaches the maximum flux recorded over the last 150 ka, over 1.5 times the average value. In comparison both the midlatitude and subarctic Pacific records show a similar variation in amplitude change relative to the average value of each record, reaching both lower and higher relative dust flux extremes than the equatorial Pacific record. This may suggest a change in dust transport across the N. Pacific at orbital timescales, with the sites at 37°N and 50°N being affected while the equatorial Pacific sees less variation.

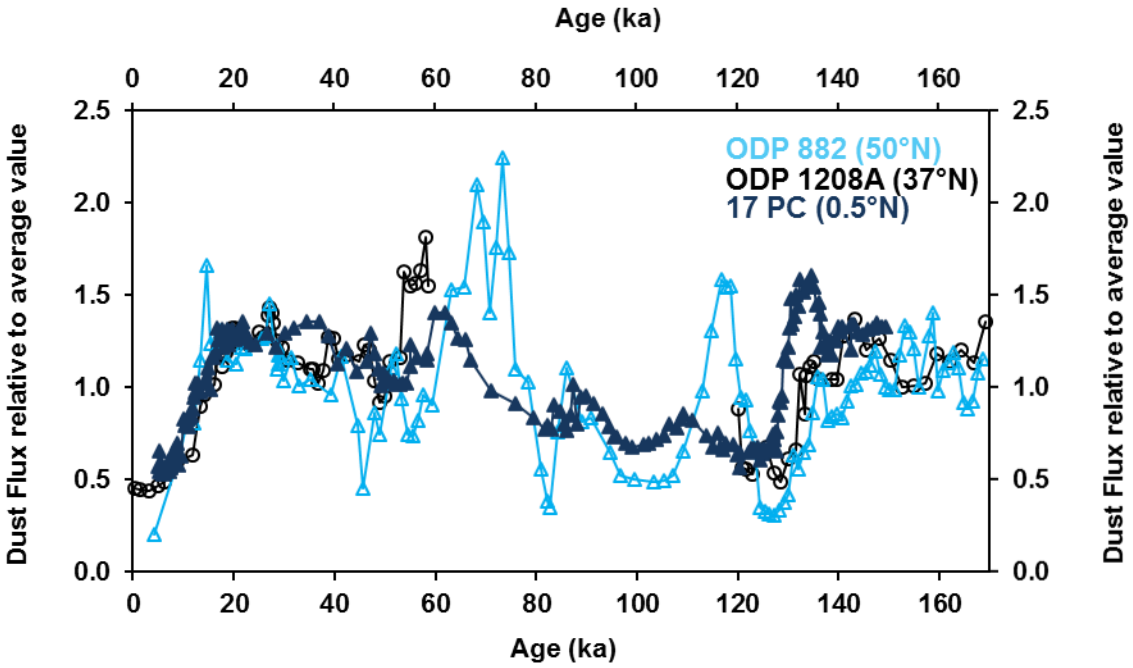

Figure 3-5. Comparison of dust fluxes in the Western Pacific from north to south. ODP Site 882 (light blow line, open triangles) is located in the North Pacific (50.4°N, 167.6°E; 3244 m water depth) (Serno et al., 2017), ODP Site 1208 (black line, open circles) is located on the Central High of Shatsky Rise, and ML1208-17PC (dark blue line, closed triangles) is located in the Equatorial Pacific (0.48°N, 156.45°W; 2926 m water depth (Jacobel et al., 2017). Each dust flux record is plotted relative to the average dust flux over the length of the each record shown.

Orbital scale trends in the ODP 1208 dust flux record are also seen in the older part of the record, at times potentially overprinting the G-IG control on dust. This can be most clearly seen during the interval from 290-240 ka (Figure 6). From 280-250 ka during the core of MIS 8 dust fluxes are high in the early part of the glacial but decrease to a minimum at 260 ka, before increasing again in the late part of the glacial. The decrease in dust flux occurs at the same time as a precesionally-driven maximum in summer (June 21st) insolation at 65°N. A similar, but more muted, response to insolation forcing during a glacial can be seen during the core of MIS 6 where at 155 ka at dust flux minimum occurs at the same time as a precesionally-driven maximum in summer (June 21st) insolation at 65°N. Thus there is some clear evidence for an insolation control on dust flux export from East Asia overriding the G-IG control, potentially related to the length of the dust season in East Asia, or more intense dust storms.

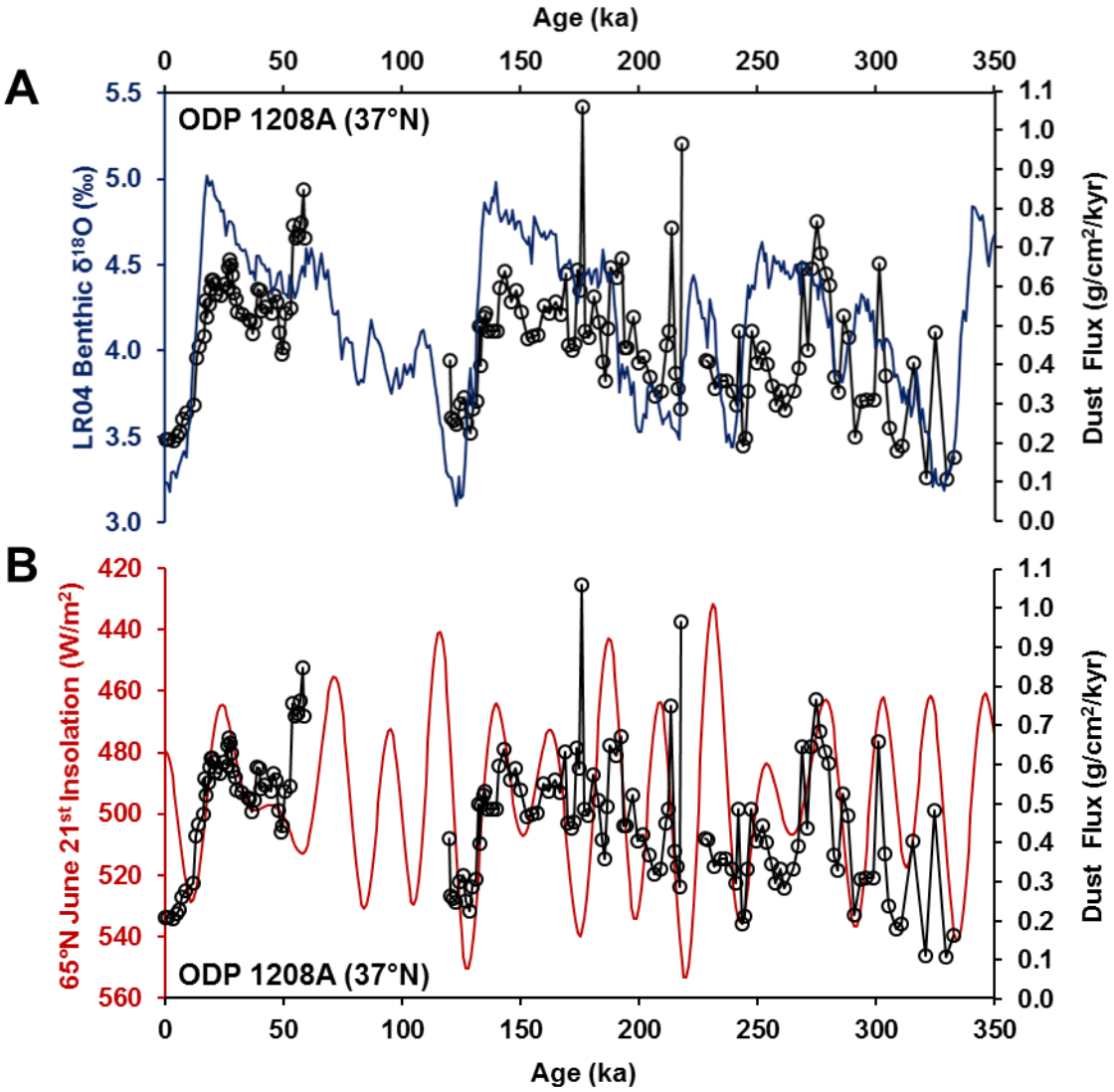

Figure 3-6. Panel A: Comparison of dust fluxes at ODP Site 1208 (black line, open circles) with LR04 benthic oxygen isotope stack (blue line) (Lisiecki & Raymo, 2005). Panel B: Comparison of dust fluxes at ODP Site 1208 (black line, open circles) with June 21 insolation at 65°N (red line) (Laskar et al., 2004)

3.6 Conclusions

A new high resolution $^{230}Th_{xs}$-normalized dust flux record from ODP Site 1208 on Shatsky Rise in the midlatitudes of the western North Pacific (37°N) shows good agreement with the nearby flux record of V21-146, providing confidence for using the site to reconstruct dust export from Asian source areas over the past 330 ka. The record shows a strong glacial-interglacial signal with dusty glacials, and low dust export during interglacials. This G-IG signal is observed in a transect of $^{230}Th_{xs}$-normalized dust flux records from the western North Pacific, spanning from the equatorial (ML1208-17PC; 0.5°N) to the subarctic (ODP Site 882; 50.4°N) North Pacific, with ODP Site 1208 (37°N) forming a key spatial component of the transect in the midlatitudes at the heart of the Asian dust plume. Coherence of the glacial-interglacial signal of dust flux to the North Pacific across the whole transect over the past 150 ka suggests that dust transport mechanisms did not change over these timescales. However on orbital timescales the equatorial record shows more muted variability relative the midlatitude and subarctic sites, suggesting a change in dust transport across the North Pacific which does not reach the equator. Close inspection of the G-IG variability over the full 330 ka record at ODP 1208 shows intervals where an insolation control on dust flux export from East Asia overrides the G-IG control. This is particularly pronounced during glacial times (MIS 8 and MIS 6), when decreases in dust flux occur at the same time as precesionally-driven increases in summer (June 21st) insolation at 65°N, potentially driven by changes to the length of the dust season in East Asia, or more intense dust storms.

Chapter 4

Eolian Dust Provenance Changes Recorded in Japan Sea Sediments (IODP Site U1430) Over the Past 200 ka by Radiogenic Pb, Nd, and Sr Isotopes

4.1 Abstract

Dynamics of the Westerly Jet in the Asian interior—specifically changes to the seasonal meridional position of the Westerly Jet relative to the Tibetan Plateau—have been hypothesized to drive hydroclimate change in the East Asian Monsoon on millennial- to orbital-timescales. Reconstruction of Westerly Jet behavior, by using radiogenic isotopes to fingerprint the changing source region of dust using downwind sediment archives, and comparison with complementary records reflecting East Asian Monsoon intensity and extent may allow the examination of Westerly Jet mean state and variability, and its coupling with the East Asian Monsoon. Here, we present records spanning the last 200 ka of the lead, neodymium, and strontium isotopic composition of isolated eolian material from IODP Site U1430 (Sea of Japan) to validate the feasibility of this approach, and lay a foundation for future work examining millennial- and orbital-scale variability of Westerly Jet behavior, and the impact these dynamics have on East Asian hydroclimate.

Comparison of the lead, neodymium, and strontium isotopic data from U1430 with the composition of potential source regions reveals that the $^{143}Nd/^{144}Nd$ signal is the most robust out of these radiogenic isotope systems for fingerprinting the provenance of eolian material at the core site. The $^{143}Nd/^{144}Nd$ composition shows resolvable orbital-scale variability from 200 to 100 ka, with muted variability from 100 to 0 ka. The orbital-scale variability shows a coherent signal of a positive shift in neodymium values (higher proportion of eolian material sourced from north of 42°N) with high summer insolation at 65°N and a strong Asian monsoon, and a negative shift in neodymium values (lower proportion of eolian material sourced from north of 42°N) with low summer insolation at 65°N and a weak Asian monsoon. This finding implies a quicker shift of the

Westerly Jet to the north of the Tibetan Plateau during times of a strong Asian monsoon, offering support for Chiang et al.'s (2015) Jet-Transition Hypothesis. The neodymium provenance record also reveals the absence of a clear glacial-interglacial signal in the seasonal position of the Westerly Jet.

4.2 Introduction

The East Asian Summer Monsoon (EASM) rains provide freshwater to about a quarter of the world's population, vital for agriculture and for human use. The dynamics that control the EASM are poorly understood in modern climatology, meaning that the future of this resource is hard to constrain under climate change scenarios, which is vital to planning efforts. Recent work has aimed to develop a better understanding of the large scale structure of the rainfall regime over East Asia and the driving forces behind year to year variation over the past 50 years in the EASM. It has been shown that East Asian hydroclimate is intimately linked to the Westerly Jet (WJ), the subtropical jet stream over East Asia (e.g., Molnar et al., 2010), and its position relative to the Tibetan Plateau (e.g., Schiemann et al., 2009). Occurrences of the WJ, identified as local maxima in latitude–pressure cross sections of the horizontal wind field (Schiemann et al., 2009), to the south of the plateau are associated with light persistent rains in south China during spring. As the jet transitions to the north of the plateau occurrences are associated with development of a strong convective rainfall front (the Meiyu-Baiyu) which moves northward through late spring into central China. At the onset of summer, the jet occurrences shift far to the north of the plateau, and this is associated with dispersement of the Meiyu-Baiyu front and transition to lighter rains to the north of China (Chiang et al., 2015; Schiemann et al., 2009).

Association of the meridional WJ position and East Asian rainfall in modern day climatology has led to the development of a framework to explain changes to rainfall on paleoclimate time scales, as driven by seasonal changes to the WJ. This was presented by Chiang et al. (2015), building on the work of Nagashima and colleagues (2011; 2013) as the "Jet Transition Hypothesis", stating that "changes to the seasonal meridional position of the westerlies relative to the Tibetan Plateau drive rainfall climate changes over East Asia on paleoclimate timescales" (Figure 4-1, Panel A). The aim of this hypothesis was to posit a mechanism for explaining changes to Asian rainfall over

paleoclimate time scales, but inherently also makes predictions for WJ behavior with changing climate. For example, the hypothesis would predict that at times of high (low) northern hemisphere summer insolation (due to precessional changes) the WJ will move more (less) quickly in the season to a position far to the north of the Tibetan Plateau, thus reducing (increasing) spring rains in south and central China, and increasing (decreasing) rains in the north of China (Figure 4-1, Panel B).

Speleothem archives have been utilized to reconstruct rainfall over eastern China due to their ability to record proxies of rainfall (e.g., calcite $\delta^{18}O$) with high precision age constraints utilizing U-Th dating over the past >500 ka (e.g., Wang et al., 2008). These records show strong precession control on Asian rainfall with no strong glacial-interglacial (G-IG) signal observed (Cheng et al., 2016). Less is known about WJ behavior over the same time interval, in part due to the fact that changes in winds leave a less clearly observable rock record to study. North Pacific records of dust accumulation rates, taken to be generally representative of export of Asian dust, over the past >500 ka have conversely shown a G-IG signal with low dust in interglacial times, and dusty glacials (Hovan et al., 1989; Winckler et al., 2008). Nagashima et al. (2007, 2011, 2013) have used the electron spin resonance (ESR) intensity and the crystallinity index (CI) of quartz as provenance indicators in an attempt to hone in on changes to transport pathways of Asian dust to the Sea of Japan, and interpret records of the past 140 ka (with a focus on the Holocene and millennial-scale change in MIS3) as mainly representative of changes in the contribution of Taklimakan Desert vs. Gobi Desert sourced material. They interpret this to show that, for example, northward shifts of the WJ during late summer occurred during interstadials (Nagashima et al., 2011). Targeted work to increase our understanding of spatial changes to the WJ pathway and seasonal movement over time through expansion of proxy development in this region is key to resolving differences in the nature of the response of rainfall and the WJ to external forcing, and testing the predictions made by the WJ hypothesis.

The sedimentary record of the Sea of Japan provides a high resolution archive of Asian dust, with the potential for reconstructing WJ behavior (Irino & Tada, 2003; Nagashima et al., 2007). We wish to explore WJ behavior using other proxy records from the Sea of Japan, namely radiogenic isotopes which are well tested for provenance fingerprinting, and push these records back further

in time to expand the record of WJ behavior over longer cycles of orbital scale climate variability. Chinese deserts and sandy lands have different Pb-Nd-Sr isotopic compositions dependent on the lithology and age of the country rocks from which their sediments are derived (e.g., Chen et al., 2007; Li, 2007), allowing for the potential use of these radiogenic isotope systems to be applied on a sediment archive downwind of these source areas to distinguish different isotopic mixing ratios through time indicating changes to the seasonal position of the WJ. Site U1430 located in the central western part of the Sea of Japan was cored by Integrated Ocean Drilling Program (IODP) Expedition 346 in 2013, providing prime material for testing the efficacy of radiogenic isotopes as a proxy for tracing WJ behavior (Tada et al., 2013). Recent work on U1430 has shown that the silicate component of the sediment over the past is windblown dust from Chinese deserts, with a minor component (6-7 %) of material from Korea over the Plio-Pleistocene, with no discernible volcanic input or material sourced from the Japanese islands (Anderson et al., 2019), which makes it a good site for attempting to reconstruct Asian dust provenance. Limited radiogenic isotope work (Pb-Nd-Sr) has been carried out on the clay fraction (<2 micron) of 7 samples of U1430 sediments over the Plio-Pleistocene (Shen et al., 2017), with targeted analysis of the Nd-Sr data interpreted by the authors as showing mixing of a major component (Asian eolian dust) and minor component (fluvial input from Japan). This work shows the promise of utilizing radiogenic isotopes on this core site for reconstructing provenance change from Asian dust source areas, while highlighting a potential issue in the clay fraction as it contains a minor component of Japan-sourced material. We make Pb, Nd, and Sr isotopic measurements on the leached (to remove carbonate, organics, and Fe-Mn oxyhydroxides) and grain size separated (2-16 micron) fraction of 28 downcore sediment samples from U1430 spanning the last 200 ka. Focused interpretation is paid to the Nd data as it shows the clearest resolvable provenance signal, which we use to test predictions that the WJ hypothesis makes over G-IG and precessional cycles.

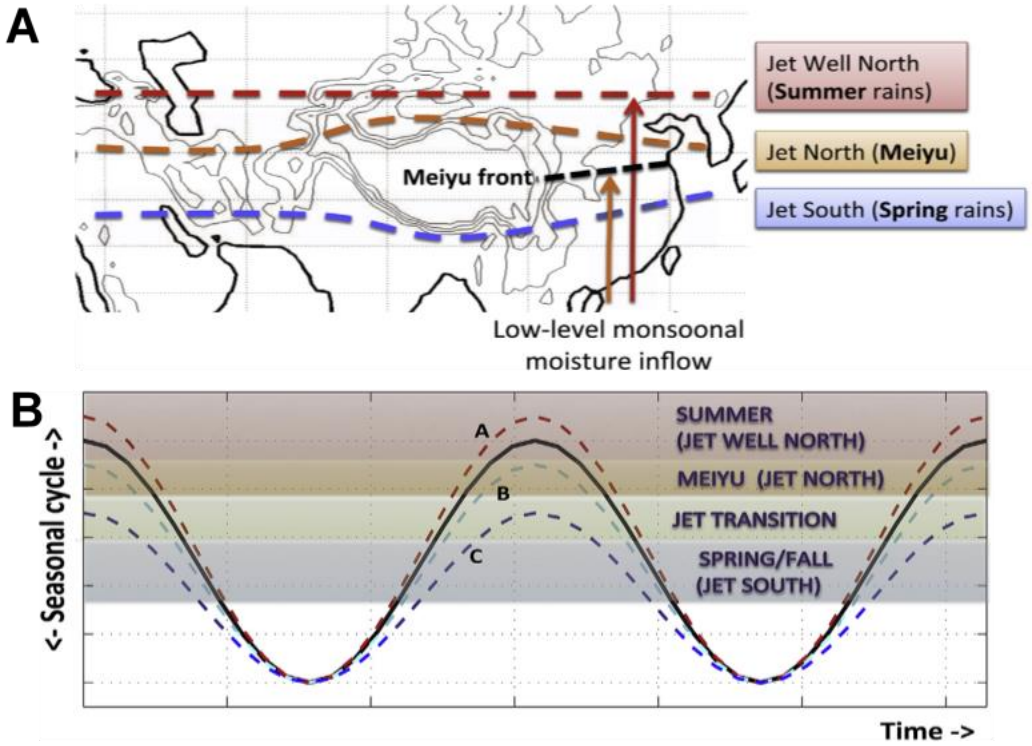

Figure 4-1. Panel A: Idealized map of the "normal" East Asian seasonal cycle. In spring the WJ lies to the south of the Tibetan Plateau (blue dashed line), associated with light persistent rains in south China. As the jet transitions in late spring to the north of the plateau (orange dashed line) development of a strong convective rainfall front (the Meiyu-Baiyu; black line) moves northward into central China (orange arrow). At the onset of summer, the WJ shifts far to the north of the plateau (red dashed line), associated with dispersement of the Meiyu-Baiyu front (red arrow) and transition to lighter rains to the north of China. Panel B: Idealized schematic of the "normal" East Asian seasonal cycle relative to rainfall/jet transitions (black line). The WJ hypothesis posits a mechanism for explaining changes to Asian rainfall over paleoclimate time scales, but inherently also makes predictions for WJ behavior. For example, the hypothesis would predict that at times of high northern hemisphere summer insolation (due to precessional changes) that the WJ will move more quickly in the season to a position far to the north of the Tibetan Plateau, thus reducing spring rains in south and central China, and increasing rains in the north of China (Scenario A; red dashed line). Adapted from Chiang et al. (2015).

4.3 Methods and Core Site

4.3.1 Core Location and Age Model

Site U1430 was cored as part of IODP Expedition 346 (Tada et al., 2013) in the Ulleung Basin of the Sea of Japan (37°54.16'N, 131°32.25'E), at 1072 meters water depth (Figure 4-2). The material at this core site over the past 4 Ma is sourced predominantly from Asian deserts as windblown detritus, with a minor component from Korean rivers (Anderson et al., 2019).

The age model for U1430 (Figure 4-2) over the last 1.45 Ma is based on visual correlation of marker dark layers in the sediment with corresponding marker dark layers at IODP Site U1424 in the eastern Sea of Japan (Figure 4-3) (Irino et al., 2018; Tada et al., 2015), which has an existing age model. The U1424 age model (Tada et al., 2018) is based on tephra-chronology and magnetostratigraphy, further tuned by correlation of the gamma ray attenuation (GRA) and natural gamma radiation (NGR) profiles to the LR04 benthic $\delta^{18}O$ stack profile (Lisiecki & Raymo, 2005) to assign ages based on the stack's tuned $\delta^{18}O$ timescale (Figure 4-4).

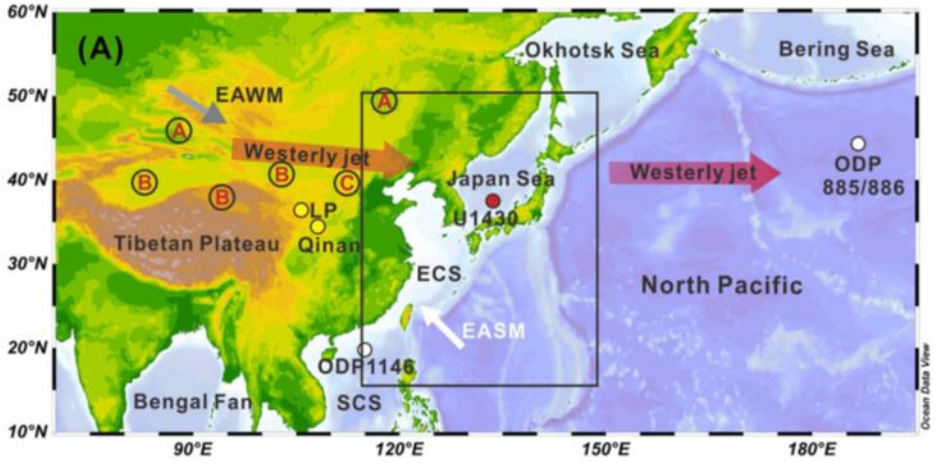

Figure 4-2. Map showing U1430 core site in the Ulleung Basin of the Sea of Japan (37°54.16'N, 131°32.25'E), at 1072 meters water depth (red dot), and potential Asian desert source areas for eolian material (red letters) from Shen et al. (2017).

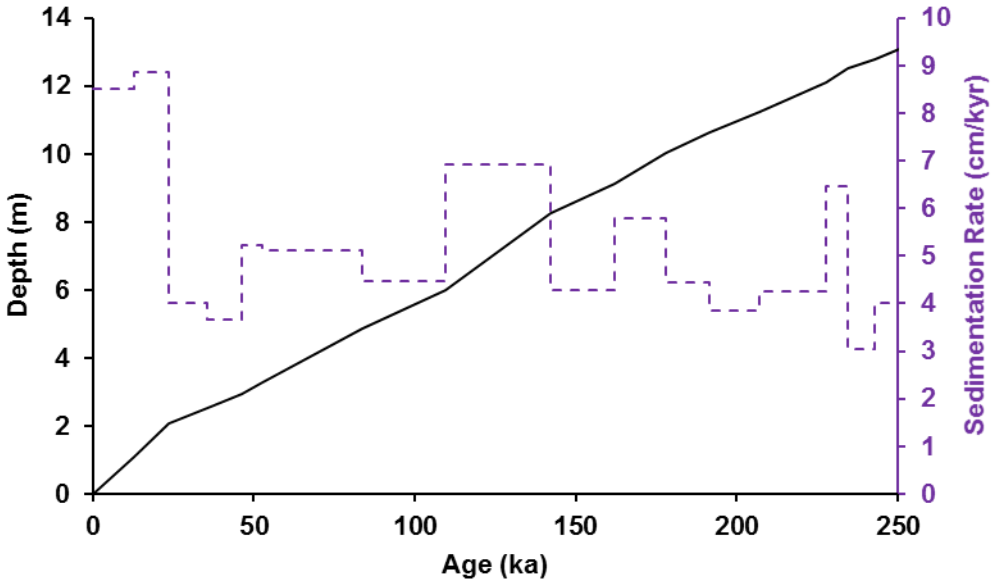

Figure 4-3. Age-depth plot and sedimentation rates for IODP Site U1430.

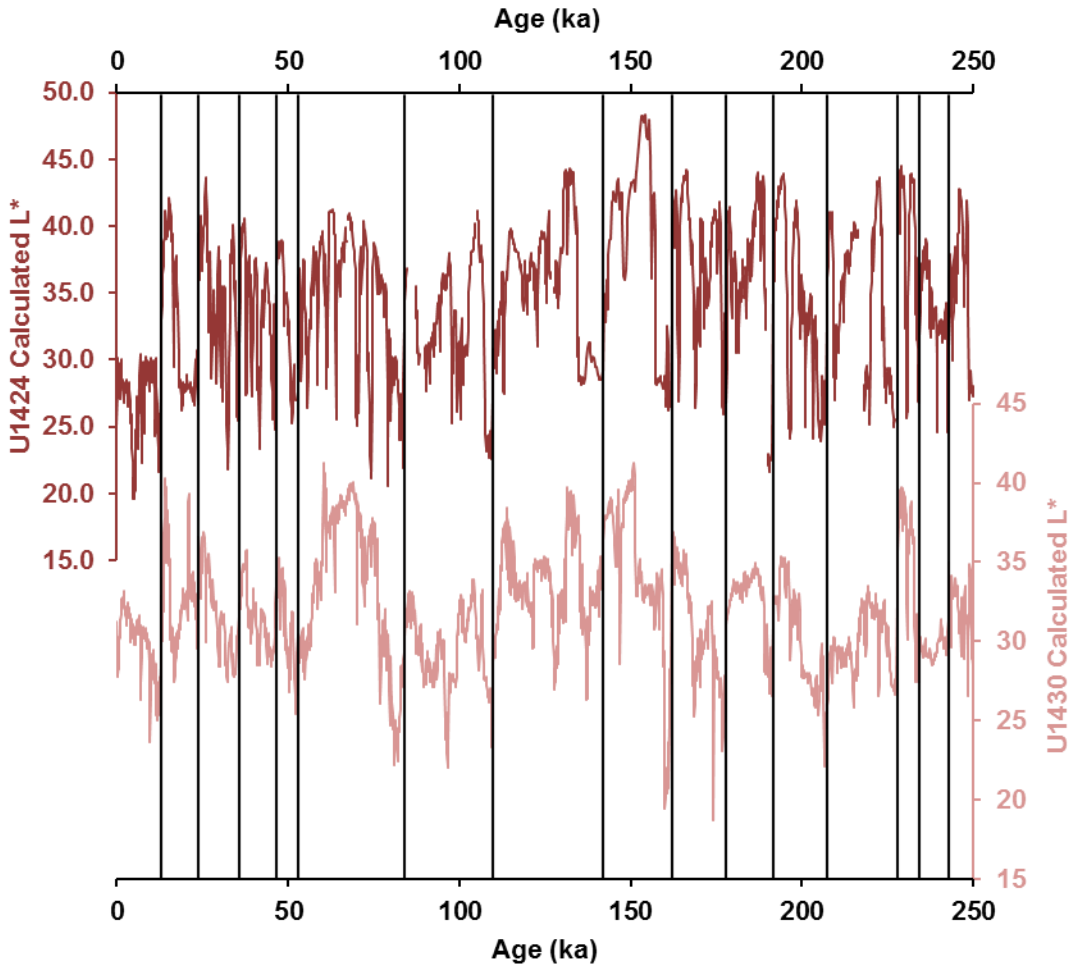

Figure 4-4. IODP Site U1424 and U1430 calculated L* (Tomohisa Irino et al., 2018). Marker dark layers from Site U1424 are assigned ages and then correlated to marker dark layers at Site U1430 (shown as black lines), and thus a projected age can be assigned to the dark layers at Site U1430 (Tada et al., 2018).

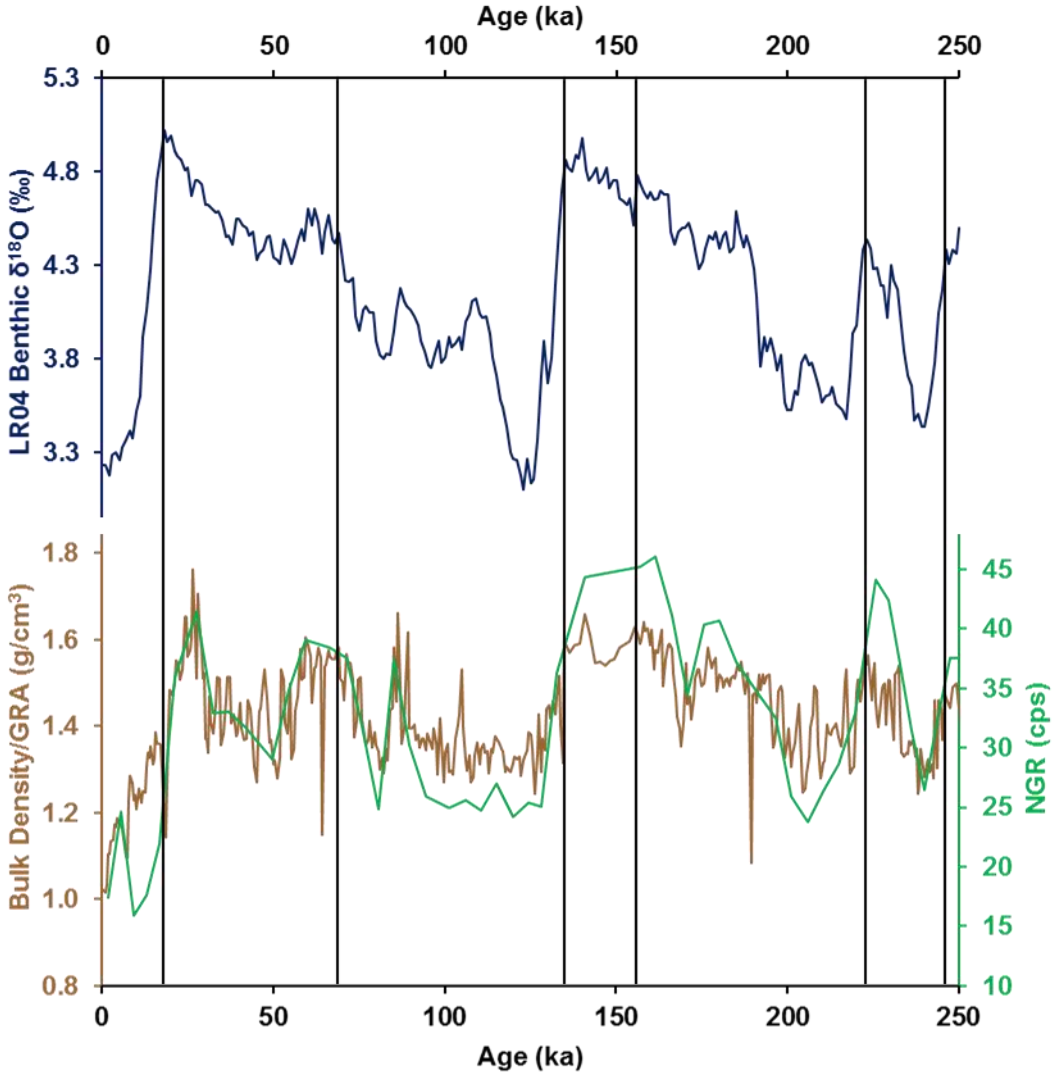

Figure 4-5. IODP Site U1424 NGR and GRA (Tomohisa Irino et al., 2018), plotted with LR04 stack (Lisiecki & Raymo, 2005). Age model for U1424 is constructed by tuning to LR04 and dating of tiepoints to the stack which are shown as black lines (Tada et al., 2018).

4.3.2 Geochemistry Methods

4.3.2.1 Labwork Procedure

Protocols for isolation and measurement of Pb, Nd, and Sr isotopes from ocean sediment samples were set up in the McGee Lab to apply to samples from U1430. The procedure for the measurement of these radiogenic isotopes was designed as a combined procedure whereby a sediment sample was leached, grain-size separated, dissolved, and put through a series of columns in sequence, to isolate and purify Pb, Nd, and Sr respectively, for mass spectrometry measurement (Figure 4-6, Panel A). This stepwise procedure means that each sample only needs to be dissolved once, and minimizes the mass of sample needed to measure the isotopes of all three elements. The labwork was carried out in a laminar flow hood in the outer room of the McGee Lab. Full procedural blank measurements were made using clean 2% nitric acid to verify that we can make low blank, and thus uncontaminated and primary signal, measurements. The full procedural total lead blank was 222 pg, total neodymium blank was 112 pg, and total strontium blank was 122 pg.

In order to confirm that the column chemistry and mass spectrometry protocols were giving precise and accurate data for comparison with other records, two geostandards (BCR-2 and MAG-1) which have published values for Pb, Nd, and Sr were taken through the procedure and treated as unknown samples. Measurement of BCR-2 gave $^{208}Pb/^{204}Pb = 38.6507$, $^{143}Nd/^{144}Nd = 0.512658$, and $^{87}Sr/^{86}Sr = 0.705491$. Accepted values for BCR-2 are $^{208}Pb/^{204}Pb = 38.691$ (Woodhead & Hergt, 2000), $^{143}Nd/^{144}Nd = 0.512633$ (Raczek et al., 2003), and $^{87}Sr/^{86}Sr = 0.704958$ (Raczek et al., 2003). Measurement of MAG-1 gave $^{208}Pb/^{204}Pb = 38.7650$, $^{143}Nd/^{144}Nd = 0.512110$, and $^{87}Sr/^{86}Sr = 0.723428$. Accepted values for BCR-2 are $^{208}Pb/^{204}Pb = 38.792$ (Nath et al., 2009),$^{143}Nd/^{144}Nd = 0.512046$ (Nath et al., 2009), and $^{87}Sr/^{86}Sr = 0.722739$ (Nath et al., 2009). It can be seen that our measurements are close to within uncertainty of the published geostandards for all of the isotopic systems.

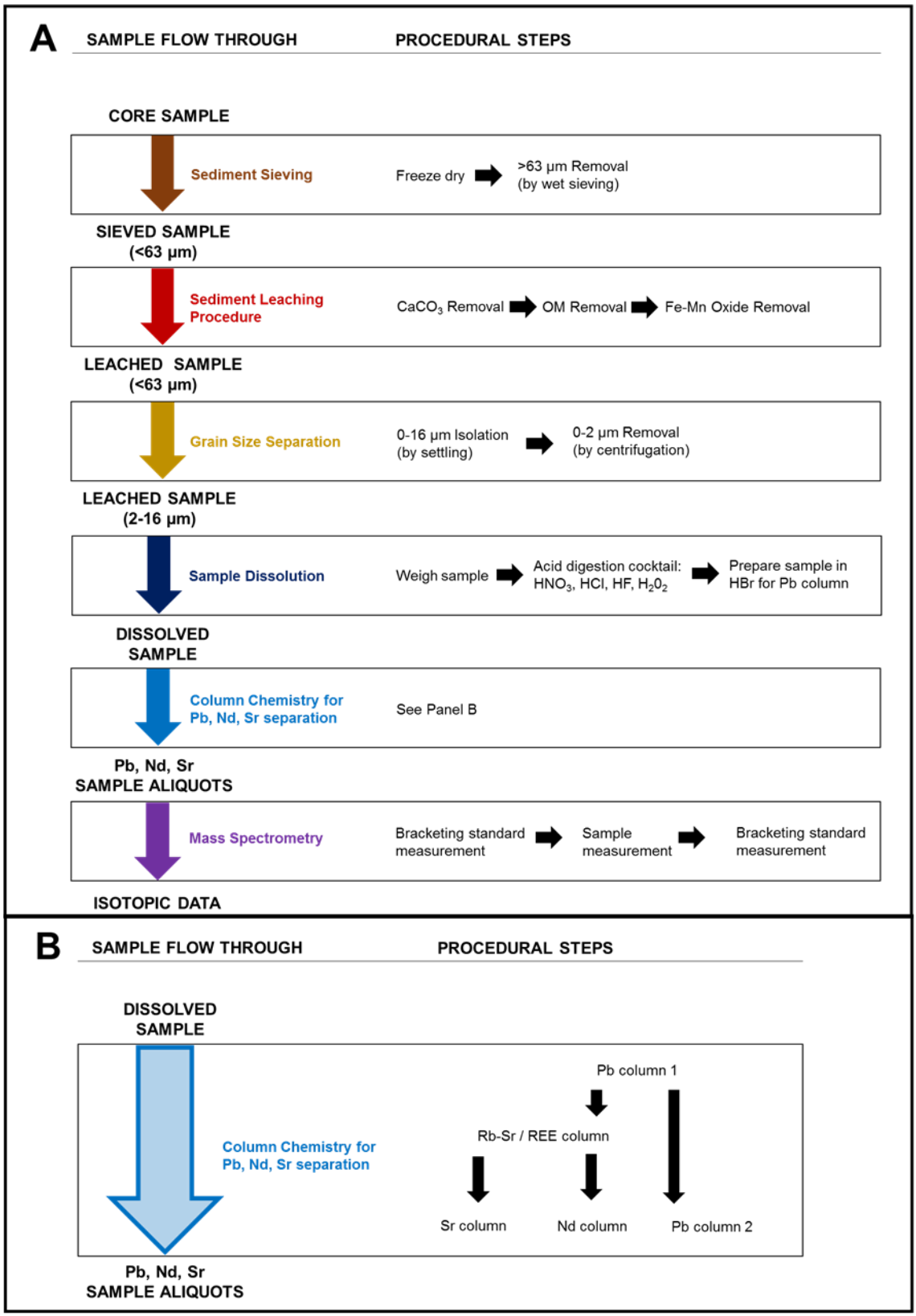

Figure 4-6. Panel A: Flowchart of full lab procedure, taking sample from initial starting material from sediment core through to analyzed lead, neodymium, and strontium isotopic data. Panel B: Details of the column chemistry procedure for the lead, neodymium, and strontium separation step.

4.3.2.2 Initial sample preparation and leaching

Sediment samples of U1430 core material were frozen overnight in their sample bags from the IODP Kochi Core Center, Japan, and freeze-dried for 24 hours to remove water. One gram of sample was weighed into a 50 ml c-tube and 20 ml of MQ was added and placed on a shaker table for 24 hours, at an angle to minimize sediment settling, to disaggregate the sediment. The sample was poured onto a 63 μm sieve, with a 250 ml Pyrex beaker underneath to catch the MQ and <63 μm sediment particles below. MQ was sprayed with a spray bottle over the remaining material on the sieve, and lightly brushed with a fine paint brush to disaggregate any remaining sediment. This process is continued until only clear MQ is dripping into the glass beaker from the sieve, indicating that there is no more <63 μm sediment getting through the sieve. The >63 μm sediment fraction on the sieve was dried at 60°C in an oven and swept off the sieve using a soft bristled brush into a 2 ml glass vial for archival purposes. The <63 μm sediment fraction in MQ was poured back into the 50 ml c-tube it was originally in, and centrifuged at 5000 rpm for 10 minutes. A 5 ml pipette was used to decant the MQ, being very careful not to disturb the sediment at the bottom of the tube. This process was repeated, rinsing the 250 ml beaker with a spray bottle of MQ until all of the sediment was back in the c-tube. The c-tube of sediment (<63 μm fraction) was then frozen overnight and freeze-dried for 24 hours, and subsequently weighed by pouring the sediment out onto weighing paper. The sample was put back into the c-tube ready for chemical leaching.

Chemical leaching was carried out on the <63 μm fraction of the sediment samples in order to remove material that could contaminate the terrestrial material with Pb, Nd, and Sr isotopes from marine sources. The material targeted for removal was carbonate, organic matter, and Fe-Mn oxide coatings, following adapted methods from Bayon et al. (2002; 2015).

25 ml of 5 % acetic acid was added to the sample, which was then put overnight lightly capped on a shaking table, at an angle to minimize sediment settling, to dissolve the calcium carbonate in the sediment. The c-tube was then sealed and centrifuged at 5000 rpm for 10 minutes and the acetic acid supernatant decanted carefully using a 5ml pipette to waste. 25 ml of MQ was added to the tube, mixed using a vortex mixer to ensure all sediment was mixed into the MQ after it had been compacted by centrifugation, and centrifuged for 10 minutes at 5000 rpm, and the supernatant

carefully decanted using a 5ml pipette. This process was repeated another 2 times so that in total the sample was rinsed 3 times with MQ.

25 ml of 5 % hydrogen peroxide was added to the sample, which was then put overnight loosely capped on a shaking table, at an angle to minimize sediment settling, to dissolve the organic matter in the sediment. The c-tube was then sealed and centrifuged at 5000 rpm for 10 minutes and the hydrogen peroxide supernatant decanted carefully using a 5 ml pipette to waste. 25 ml of MQ was added to the tube, mixed using a vortex mixer to ensure all sediment was mixed into the MQ after it had been compacted by centrifugation, and centrifuged for 10 minutes at 5000 rpm, and the supernatant carefully decanted using a 5ml pipette. This process was repeated another 2 times so that in total the sample is rinsed 3 times with MQ.

25 ml of 0.05 M hydroxylamine hydrochloride in 15% acetic acid was added to the sample, which was then put overnight loosely capped on a shaking table, at an angle to minimize sediment settling, to dissolve the Fe-Mn oxide coatings in the sediment. The c-tube was then sealed and centrifuged at 5000 rpm for 10 minutes and the hydroxylamine hydrochloride in acetic acid supernatant decanted carefully using a 5 ml pipette to waste. 25 ml of MQ was added to the tube, mixed using a vortex mixer to ensure all sediment was mixed into the MQ after it had been compacted by centrifugation, and centrifuged for 10 minutes at 5000 rpm, and the supernatant carefully decanted using a 5ml pipette. This process was repeated another 2 times so that in total the sample is rinsed 3 times with MQ.

The c-tube was then frozen overnight and freeze-dried for 24 hours, and the sample weighed by pouring the sediment onto weighing paper.

4.3.2.3 Grain Size Separation

Grain size separation was carried out on the <63 μm fraction of the leached sediment samples in order to isolate a specific grain size fraction of the sediments. The leaching protocol removed material from marine sources leaving only terrestrial material, however this may be a mixture of eolian dust, shelf-derived sediments, and volcanic material. The grain size distribution of eolian

dust fall sampled in Japan has a range of 4-16 μm (Nagashima et al., 2007). Sediment with a smaller grain size than this range can be windblown but is also likely to be shelf-derived or from riverine input. Sediment with a larger grain size than this is likely to be of volcanic origin. Thus we decided to nominally target the 2-16 μm fraction of the sediment to remove the clays and coarse silts. Removal of the >16 μm fraction was achieved through settling, while the method used for removing the clays follows the procedure of Bayon et al. (2015).

The sample was put back into the c-tube and 25 ml of MQ was added and vortexed to mix the sediment with the MQ again and ensure it was well disaggregated. The sample was poured into a 100 ml graduated cylinder, and the tube was rinsed with MQ into the cylinder until all of the sample was transferred to the cylinder. The cylinder was filled up to the 100 ml mark with MQ, sealed with Parafilm, sonicated for 5 minutes to aid sediment disaggregation, and shaken and inverted to mix the sediment-MQ mixture thoroughly. The cylinder was then placed upright and a timer started to measure 4 minutes and 29 seconds of settling time. This was calculated from Stoke's law (Hathaway, 1956) as the time that it would take a spherical particle that is >16 μm in diameter to settle 6 cm from the top of the graduated cylinder. At the elapsed time, the sediment-MQ mixture that is within the top 6 cm of the graduated cylinder (in the specific graduated cylinder used in this study this equates to 20 ml of mixture) was rapidly removed via pipetting into a new clean c-tube. This mixture contains only particles that are <16 μm as all larger particles settle by gravity in the mixture to below the 6 cm line. However, as the sediment is thoroughly mixed with the MQ it means that finer-grained particles (<16 μm) will already have been in the lower part (below 6 cm from the top) of the cylinder prior to the settling wait time. Thus the process was repeated multiple times until the top 6 cm of sediment-MQ mixture that was being removed was clear, meaning that there was no sediment left in the graduated cylinder that was <16 μm. The <16 μm c-tube was centrifuged at 5000 rpm for 10 minutes and all MQ decanted via pipette after each addition of sediment-MQ mixture after settling. Once the top 6 cm of mixture removed was clear the <16 μm c-tube was taken to the clay (< 2 μm) removal step. The >16 μm sediment fraction remaining in the graduated cylinder was poured into the original c-tube and centrifuged for 10 minutes at 5000 rpm and the MQ was decanted. The >16 μm fraction was transferred to a Whirlpak for archival purposes after being frozen, freeze-dried, and weighed.

The <16 μm fraction was taken through a clay removal process, to separate the particles <2 μm in diameter from the remaining grain size fraction, according to the methods of Bayon et al., (2015), who calculated time and angular velocities required to separate clays using a formula derived from Stoke's law (Hathaway, 1956). 25 ml MQ was added to the c-tube with the <16 μm fraction, shaken vigorously and sonicated, and centrifuged at 1000 rpm for 2 minutes (133 g). The supernatant containing clays was decanted using a 5 ml pipette into a new 50 ml c-tube for the <2 μm fraction. Another 25 ml of MQ was added to the c-tube containing the <16 μm fraction, shaken vigorously and sonicated, and centrifuged for 2.5 minutes at 800 rpm (85 g). The supernatant containing clays was decanted using a 5 ml pipette into the <2 μm c-tube. The fine silt fraction (2-16 μm) was centrifuged for 10 minutes at 5000 rpm and the MQ was decanted. This fraction was transferred to a Whirlpak after being frozen, freeze-dried, and weighed, and taken on to the dissolution step. The clay (<2 μm) fraction of sediment was centrifuged for 10 minutes at 5000 rpm and the MQ was decanted, before the sample was frozen, freeze-dried, and weighed, prior to archival in a Whirlpak.

4.3.2.4 Sediment Dissolution

Following the leach and grain size separation steps, the 2-16 μm leached sediment sample was taken through the dissolution procedure in preparation for column chemistry. 500 μl of MQ was pipetted into a clean Savillex PFA beaker, and the beaker was tared on a scale. Sample was scooped with a compressed-air cleaned metal spatula and 20 mg were poured directly into the beaker on the scale. 500 μl of concentrated clean nitric acid was pipetted into the beaker, making sure to rinse down the sides to ensure all sediment was in the acid solution. The sample was dried down on a hotplate at 150 °C. 1 ml of concentrated clean nitric acid and 500 μl of concentrated clean hydrochloric acid were pipetted into the beaker to form reverse aqua regia, and the beaker was capped and set aside for 1 hour to react. 500 μl of concentrated clean hydrofluoric acid was added to the beaker, and the beaker was capped and refluxed on a hotplate at 95 °C for 24 hours to dissolve silicate matter. The beaker was taken off the hotplate to cool, and placed in an ultrasonic bath to be sonicated for 1 hour to aid in sediment digestion. A dropper bottle was used to add 500 μl (16 drops) of clean concentrated hydrogen peroxide drop by drop. Samples were left uncapped until they stop reacting. The beakers were tightly sealed and refluxed for 6 hours at 95 °C. Beakers

were uncapped, and a pipette with MQ was used to rinse down the inside of the beakers to ensure all solution was at the bottom of the beaker. The beaker was put on the hotplate at 150 °C uncapped to dry down the sample to incipient dryness. 500 µl of clean concentrated nitric acid was added with a pipette to each sample, and the sample was again dried down to incipient dryness at 150 °C. 500 µl of clean concentrated nitric acid was added with a pipette to each sample followed by 500 µl (16 drops) of clean concentrated hydrogen peroxide drop by drop, and the sample was again dried down to incipient dryness at 95 °C. A dropper bottle was used to add 30 drops (1 ml) of clean concentrated hydrobromic acid to each sample, and dried down at 150 °C. 15 drops (0.5 ml) of 0.7 N clean hydrobromic acid was added to each sample and beakers were sealed and refluxed overnight at 95 °C. The supernatant solution was then transferred via pipette to the lead column chemistry.

4.3.2.5 Column Chemistry

The samples were successively taken through 4 sets of column chemistry protocol (Figure 4-6, Panel B) to isolate Pb, Nd, and Sr for mass spectrometry. The column chemistry methods for the separation of the Pb, REE, and Sr aliquots were set up using methods from Brown University (Soumen Mallick), MIT (Bowring Lab), and the Isotope Geology Laboratory, Boise State University. The column chemistry methods for the separation of the Nd aliquot were set up with help from Charlotte Skonieczny.

The stepwise procedure used a first column chemistry method (Table 4-1) to isolate the Pb aliquot from the sample, while the non-Pb aliquot from the column still contained the Nd and Sr. A second pass of the first column chemistry method purified the Pb aliquot, ready for mass spectrometric measurement. The Pb cut from the first column is dried down at 150 °C, dissolved in 30 drops of concentrated hydrobromic acid, dried down at 95 °C, dissolved in 15 drops of 0.7N hydrobromic acid, and beakers were sealed and refluxed overnight at 95 °C. At this point samples were checked for any black solids, and if present the sample was transferred via pipette to a clean 2 ml c-tube and centrifuged to drive the solids to the bottom of the tube. The supernatant solution was then transferred via pipette to the second pass of the lead column chemistry. A second column chemistry method (Table 4-2) applied to the aliquot containing Nd and Sr isolated the REE aliquot

(containing Nd), while the non-REE aliquot contained the Sr. A third column chemistry method (Table 4-3) applied to the REE aliquot isolated and purified the Nd, ready for mass spectrometric measurement. A fourth column chemistry method (Table 4-4) applied to the non-REE aliquot isolated and purified the Sr, ready for mass spectrometric measurement. To prepare an aliquot for mass spectrometry for all elements the sample beaker was taken from the final column elution step, dried down at 95 °C to incipient dryness, 1 ml of concentrated clean nitric was added by dropper bottle, dried down at 95 °C to incipient dryness, 1 ml of 2% clean nitric acid was added, the sample was refluxed at 95 °C for 2 hours, cooled, then transferred into a clean 2 ml c-tube and was ready for measurement.

Step Description	Volume (µl)	Acid	Element Elution
Cleaning	1000	Milli-Q	
Cleaning	1000	6 N HCl	
Cleaning	1000	6 N HCl	
Cleaning	500	Milli-Q	
Conditioning	500	0.7N HBr	
Load sample	500	0.7N HBr	Collect Sr and REE
Elute	500	0.7N HBr	Collect Sr and REE
Elute	500	0.7N HBr	Collect Sr and REE
Rinse	300	2N HCL	Discard
Elute	1000	6N HCL	Collect Pb

Table 4-1. First column chemistry for lead separation. The process uses AG1-X8, 100-200 mesh, resin to separate lead from the other elements in the sample, as lead has an affinity for the resin under weak hydrobromic acid conditions while other elements pass over the column, and is eluted from the resin with hydrochloric acid. This column procedure is set up on a "lazy susan" to enable 16 columns at a time to be processed at once. The column volume is 100 µl, and is constructed from 3/8" 4:1 shrink teflon (PTFE). The columns are inserted into white plastic holders in order for the column itself to be kept as clean as possible as it is not handled.

Step Description	Volume (µl)	Acid	Element Elution
Cleaning	1000	1 N HCl	
Conditioning	500	1N HNO_3	
Load sample	500	1N HNO_3	Collect Rb, Sr
Elute	250	1N HNO_3	Collect Rb, Sr
Elute	250	1N HNO_3	Collect Rb, Sr
Elute	250	1N HCL	Collect REE
Elute	250	1N HCL	Collect REE

Table 4-2. Second column chemistry for separation of the REE and strontium. The process uses TR-B25A, 100-150 micron mesh, resin to separate the REEs from the other elements in the sample, as the REEs have an affinity for the resin under weak nitric acid conditions while other elements pass over the column, and are eluted from the resin with hydrochloric acid. This column procedure is set up on a "lazy susan" to enable 16 columns at a time to be processed at once. The column volume is 100 µl, and is constructed from 3/8" 4:1 shrink teflon (PTFE). The columns are inserted into white plastic holders in order for the column itself to be kept as clean as possible as it is not handled.

Step Description	Volume (µl)	Acid	Element Elution
Cleaning	1000	6N HCl	
Conditioning	500	0.25N HCl	
Conditioning	500	0.25N HCl	
Load sample	100	0.25N HCl	Discard
Rinse	100	0.25N HCl	Discard
Rinse	100	0.25N HCl	Discard
Elute	800	0.25N HCl	Collect Nd

Table 4-3. Third column chemistry for neodymium separation. The process uses Ln-B25S, 50-100 micron mesh, resin to separate neodymium from the other REE in the sample. All REE have a weak affinity for the resin under weak hydrochloric acid, and as it is sequentially added to the column the REE are eluted in order of increasing mass, with the lighter REE eluting from the column first. This column procedure is set up using two column racks that enable 20 columns at a time to be processed at once in a single line. The column volume is 900 µl, and is constructed from a 3ml VWR Disposable Graduated Transfer Pipette (polyethylene).

Step Description	Volume (µl)	Acid	Element Elution
Cleaning	1000	Milli-Q	
Cleaning	1000	Milli-Q	
Conditioning	500	3N HNO_3	
Load sample	500	3N HNO_3	Discard
Rinse	200	3N HNO_3	Discard
Rinse	200	3N HNO_3	Discard
Rinse	200	3N HNO_3	Discard
Elute	1000	Milli-Q	Collect Sr

Table 4-4. Fourth column chemistry for strontium separation. The process uses TR-B25A, 100-150 micron mesh, resin to separate strontium from the other elements in the sample, as strontium has an affinity for the resin under weak nitric acid conditions while other elements pass over the column, and is eluted from the resin with MQ. This column procedure is set up on a "lazy susan" to enable 16 columns at a time to be processed at once. The column volume is 100 µl, and is constructed from 3/8" 4:1 shrink teflon (PTFE). The columns are inserted into white plastic holders in order for the column itself to be kept as clean as possible as it is not handled.

4.3.2.6 Mass Spectrometry

The samples were measured at MIT in separate batches for each isotope system (Pb, Nd, and Sr) on a Nu Plasma II-ES MC-ICP-MS with an Aridus II Desolvating Nebulizer System utilizing a C-Flow PFA microconcentric nebulizer (100 μl/min.). Each sample was bracketed by a standard in order to correct for mass bias drift.

The methods created for measurement of lead were termed "Pb_Tl_Hg-IC2", and used the cup configuration shown in Table 4-5. This was carried out with mass separation of 1. All isotopes were measured on Faraday cups, except ^{202}Hg which was measured on an ion counter due to the very low signal. Prior to measurement for lead isotopic composition the samples were sipped by taking up the sample for 15 seconds until a stable lead signal was obtained in order to estimate the lead concentration. This was used to calculate how much of a spike solution created using a BDH Thallium ICP standard to dope each sample with to attain a (total Pb):(total Tl) ratio of 5:1. This was used to internally correct for mass bias using an exponential law with a ^{203}Tl/^{205}Tl = 0.418922. The isobaric interference of ^{204}Hg (which is found in the argon gas) on ^{204}Pb was corrected for by measuring the ^{202}Hg signal and calculating the contribution of ^{204}Hg using the natural abundance ratio of ^{204}Hg/^{202}Hg = 0.229. Samples were analyzed for 10 measurements of 2 second integration time, with a blank measurement made in 2% nitric acid removed during data processing.

Repeated measurements of 50 ng/g Pb standard NIST SRM 981 yield an average of ^{206}Pb/^{204}Pb = 16.9341 ± 13, ^{207}Pb/^{204}Pb = 15.4877 ± 12, ^{208}Pb/^{204}Pb = 36.6862 ± 26 (2σ, n = 14). Accepted values for NIST SRM 981 are ^{206}Pb/^{204}Pb = 16.9356, ^{207}Pb/^{204}Pb = 15.4891, ^{208}Pb/^{204}Pb = 36.7006 (Todt et al., 1996).

Detector	**H6**	**H5**	**H4**	**H3**	**H2**	**H1**	**Ax**	**L1**	**L2**	**L3**	**L4**	**IC2**	**L5**
Isotope						**^{208}Pb**	**^{207}Pb**	**^{206}Pb**	**^{205}Tl**	**^{204}Pb**	**^{203}Tl**	**^{202}Hg**	

Table 4-5. Detector configuration for lead mass spectrometry.

The methods created for measurement of neodymium were termed "Nd_Ce_Sm", and used the cup configuration shown in Table 4-6. This was carried out with mass separation of 1. All isotopes were measured on Faraday cups. The $^{146}Nd/^{144}Nd = 0.7219$ natural abundance ratio was used to internally correct for mass bias using an exponential law. The isobaric interferences of ^{142}Ce on ^{142}Nd and ^{144}Sm on ^{144}Nd were monitored by measuring the ^{140}Ce and ^{147}Sm signals respectively. Samples were analyzed for 10 measurements of 2 second integration time, with a blank measurement made in 2% nitric acid removed during data processing.

Repeated measurements of 50 ng/g Nd standard JNd-i yield an average of $^{143}Nd/^{144}Nd = 0.512125 \pm 19$ (2σ, n = 33). The accepted value for JNd-i is $^{143}Nd/^{144}Nd = 0.512115$ (Tanaka et al., 2000).

Detector	**H6**	**H5**	**H4**	**H3**	**H2**	**H1**	**Ax**	**L1**	**L2**	**L3**	**L4**	**IC2**	**L5**
Isotope	**^{150}Nd**		**^{148}Nd**	**^{147}Sm**	**^{146}Nd**	**^{145}Nd**	**^{144}Nd**	**^{143}Nd**	**^{142}Nd**		**^{140}Ce**		

Table 4-6. Detector configuration for neodymium mass spectrometry.

The methods created for measurement of strontium were termed "Sr H4_samp", and used the cup configuration shown in Table 4-7. This was carried out with mass separation of 0.5. All isotopes were measured on Faraday cups. The $^{86}Sr/^{88}Sr = 0.1194$ natural abundance ratio was used to internally correct for mass bias using an exponential law. The isobaric interference of any remaining ^{87}Rb on ^{87}Sr was corrected for by measuring the ^{85}Rb signal and calculating the contribution of ^{87}Rb using the natural abundance ratio of $^{87}Rb/^{85}Rb = 0.3857$. The isobaric interference of ^{86}Kr (which is found in the argon gas) on ^{86}Sr was monitored by measuring the ^{83}Kr signal. Samples were analyzed for 10 measurements of 2 second integration time, with a blank measurement made in 2% nitric acid removed during data processing.

Repeated measurements of 50 ng/g Sr standard NIST SRM 987 yield an average of $^{87}Sr/^{86}Sr = 0.710295 \pm 67$ (2σ, n = 22). The accepted value for NIST SRM 987 $^{87}Sr/^{86}Sr = 0.710248$ (McArthur et al., 2002).

Detector	H6	H5	H4	H3	H2	H1	Ax	L1	L2	L3	L4	IC2	L5
Isotope			^{88}Sr		^{87}Sr		^{86}Sr		^{85}Rb		^{84}Sr		^{83}Kr

Table 4-7. Detector configuration for strontium mass spectrometry.

Uncertainties from the mass spectrometry measurements for each element were calculated as 2 sigma errors based on the replicate measurements of the standard for that element.

4.4 Results

Lead, neodymium, and strontium isotopic measurements were made on the leached 2-16 μm fraction of 28 downcore sediment samples from IODP Site U1430 spanning the last 200 ka, with an average sampling resolution of 7 kyr. $^{87}Sr/^{86}Sr$ values vary between 0.716527 and 0.720063. ε_{Nd} values vary between -10.49 and -7.50. $^{207}Pb/^{204}Pb$ and $^{208}Pb/^{204}Pb$ values vary between 15.6204-15.6562, and 38.8183-38.9607, respectively.

The new isotopic data of the leached 2-16 μm fraction of U1430 sediments clusters tightly showing limited variability compared to the isotopic composition of the potential source areas (the Loess Plateau and Chinese and Mongolian Deserts and arid lands) (Figure 4-7; see Appendix C for the data). In $^{207}Pb/^{204}Pb$ vs. $^{208}Pb/^{204}Pb$ space the U1430 samples overlap with the composition of Chinese Loess, and exhibit a linear trend toward the composition of Inner Mongolian and Northern Chinese deserts and arid lands. In ε_{Nd} vs. $^{87}Sr/^{86}Sr$ space the U1430 samples overlap with the composition of the <75 μm silicate fraction of sediments from the Taklimakan, Qaidam, Badain Jaran, and Tengger Deserts, and the Loess Plateau. The samples exhibit a linear trend to more positive ε_{Nd} values similar to the Gurbantanggut Desert, and Onqin Daga, Horqin, and Hunlun Buir Sandy Lands, and to more negative ε_{Nd} values similar to the Hobq and Mu Us Deserts. Shen et al. (2017) measured the Pb, Nd, and Sr isotopic composition of the <2 μm silicate fraction of U1430 sediments, although at very coarse time resolution over the last 15 Ma, meaning that there is one sample from that study which overlaps with this study, albeit on a finer grain size fraction. In $^{207}Pb/^{204}Pb$ vs. $^{208}Pb/^{204}Pb$ the <2 μm U1430 sample directly overlaps with the cluster of samples from this study. In ε_{Nd} vs. $^{87}Sr/^{86}Sr$ space the <2 μm U1430 sample overlaps very closely with the ε_{Nd} composition of one of the samples from this study, but is offset to a more positive $^{87}Sr/^{86}Sr$ as may be expected due to the effect of grain size on the strontium isotopic composition of silicates (Chen et al., 2007).

The lead, neodymium, and strontium data can also be considered in the time domain to examine any trends throughout the last 200 ka (Figure 4-8). The $^{208}Pb/^{204}Pb$ and $^{87}Sr/^{86}Sr$ data show no discernible trend, but do exhibit cyclic variability of peaks and troughs. The ε_{Nd} data also has no discernible trend, but does show a marked change in variability at ~100 ka, from cyclic variability of peaks and troughs to a very muted signal of cyclic variability of peaks and troughs. The ε_{Nd} data exhibits a shift to more negative values in the most modern sample.

Figure 4-7. Provenance discrimination plots of Pb-Nd-Sr isotopic data of the leached 2-16 μm fraction of U1430 sediments are from this study. For comparison, the Pb-Nd-Sr isotopic data of the <2 μm silicate fraction of U1430 sediments (Shen et al., 2017), the clay fraction and bulk material from the Loess Plateau (Biscaye et al., 1997; Ferrat et al., 2012), the <75 μm and <5 μm silicate fractions of sediments from Chinese desert isotopic regions A, B, and C (Chen et al., 2007), and multiple other desert regions from China and Mongolia (Biscaye et al., 1997; Bory et al., 2014; Ferrat et al., 2012; Li, 2007), are plotted. Panel A: All $^{207}Pb/^{204}Pb$ vs. $^{208}Pb/^{204}Pb$ data. Panel B: Zoom in of the $^{207}Pb/^{204}Pb$ vs. $^{208}Pb/^{204}Pb$ data around the values of the U1430 data cluster. Panel C: All ε_{Nd} vs. $^{87}Sr/^{86}Sr$ data. Panel D: Zoom in of the ε_{Nd} vs. $^{87}Sr/^{86}Sr$ data around the values of the U1430 data cluster.

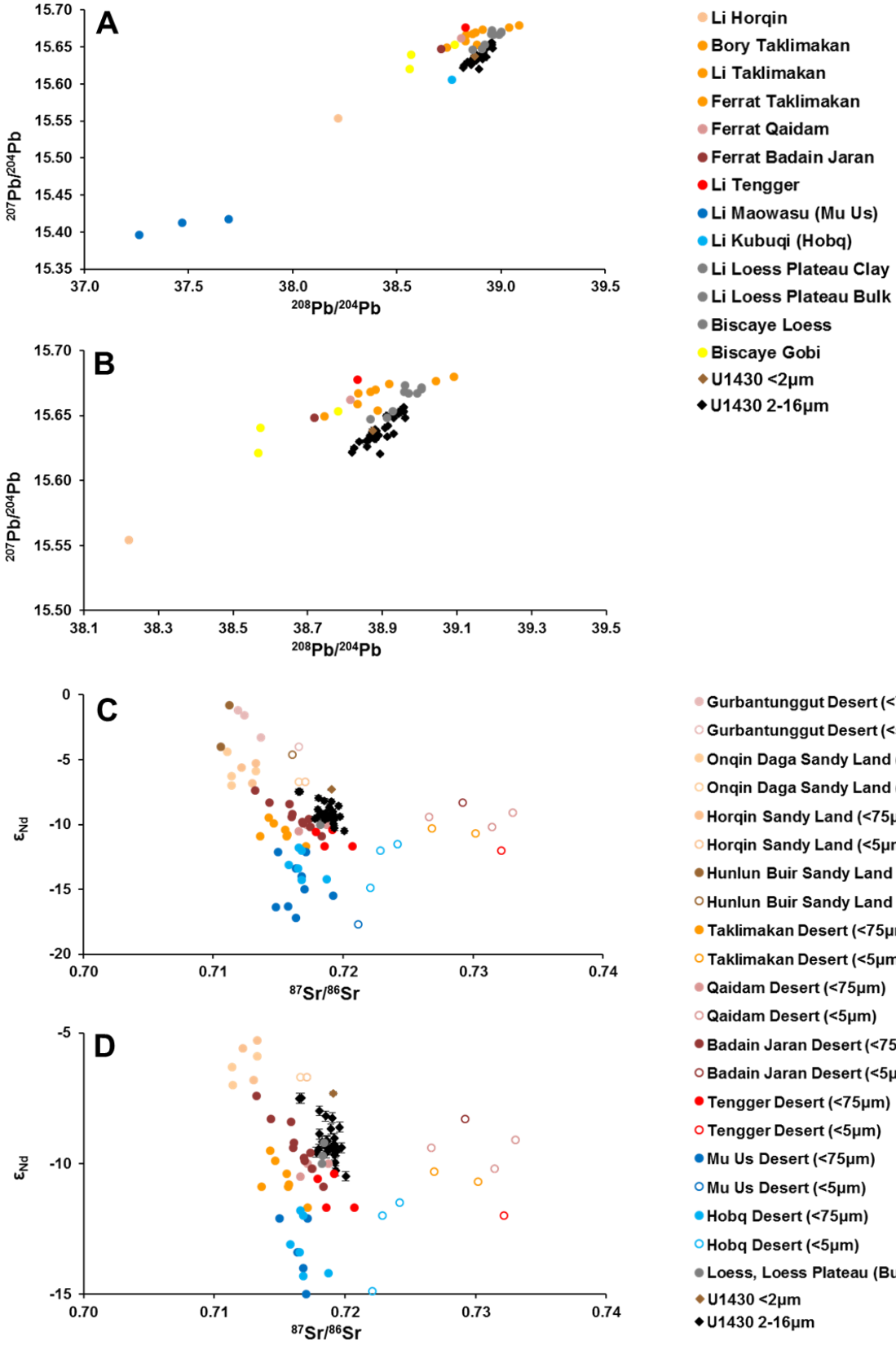
A
B
C
D
$^{207}Pb/^{204}Pb$
$^{208}Pb/^{204}Pb$
ε_{Nd}
$^{87}Sr/^{86}Sr$
Li Horqin
Bory Taklimakan
Li Taklimakan
Ferrat Taklimakan
Ferrat Qaidam
Ferrat Badain Jaran
Li Tengger
Li Maowasu (Mu Us)
Li Kubuqi (Hobq)
Li Loess Plateau Clay
Li Loess Plateau Bulk
Biscaye Loess
Biscaye Gobi
U1430 <2μm
U1430 2-16μm
Gurbantunggut Desert (<75μm)
Gurbantunggut Desert (<5μm)
Onqin Daga Sandy Land (<75μm)
Onqin Daga Sandy Land (<5μm)
Horqin Sandy Land (<75μm)
Horqin Sandy Land (<5μm)
Hunlun Buir Sandy Land (<75μm)
Hunlun Buir Sandy Land (<5μm)
Taklimakan Desert (<75μm)
Taklimakan Desert (<5μm)
Qaidam Desert (<75μm)
Qaidam Desert (<5μm)
Badain Jaran Desert (<75μm)
Badain Jaran Desert (<5μm)
Tengger Desert (<75μm)
Tengger Desert (<5μm)
Mu Us Desert (<75μm)
Mu Us Desert (<5μm)
Hobq Desert (<75μm)
Hobq Desert (<5μm)
Loess, Loess Plateau (Bulk)
U1430 <2μm
U1430 2-16μm

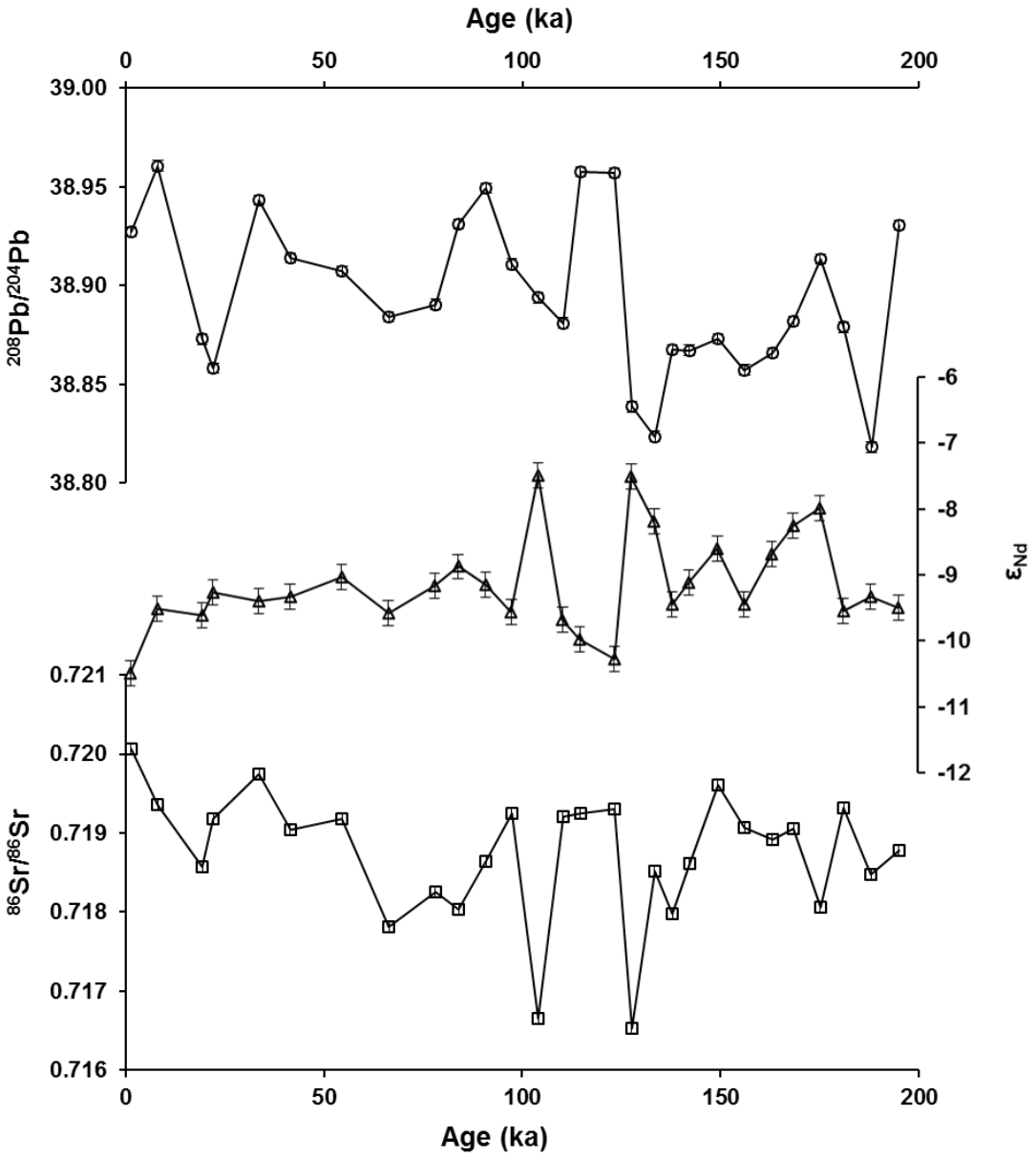

Figure 4-8. Variations in the $^{208}Pb/^{204}Pb$ (black open circles), ε_{Nd} (black open triangles), and $^{87}Sr/^{86}Sr$ (black open squares) isotopic composition of the leached 2-16 μm fraction of U1430 sediments from 200 ka to present. 2 sigma uncertainties on the isotopic measurements are shown as black bars on each sample.

4.5 Discussion

Pb, Nd, and Sr isotopes were measured on each sample in this study to provide a framework for understanding the utility of these radiogenic isotope systems as a detrital sediment provenance tracer in the Sea of Japan over the last 200 ka. The results portion of this paper (Figure 4-7, Panel A and Panel C) reveals good agreement between our new data and a compilation of published PSA measurements of Pb, Nd, and Sr isotopic composition of a variety of grain size fractions. Both the ε_{Nd} vs. $^{87}Sr/^{86}Sr$ and $^{207}Pb/^{204}Pb$ vs. $^{208}Pb/^{204}Pb$ crossplots show direct overlap between our samples and potential desert source regions. In particular the U1430 samples are most similar in composition in all 3 isotope systems to the Loess Plateau compilation, which is a mixture of material from different Asian source areas of eolian material. Provenance work carried out on the bulk material from this core site by Anderson et al. (2019) showed that in the Pleistocene the main sources of material to the core site were the Loess Plateau, the Taklimakan and Gobi Deserts, and a minor component from the Korean Peninsula. Shen et al. (2017) carried out provenance work using Pb, Nd, and Sr isotopes on the clay fraction of U1430 sediments, and while only one sample overlapped in the time domain with this study, it directly overlaps with our spread of sample compositions in this study. The provenance work of Shen et al. (2017) also pointed out a volcanic source in their provenance determination, which they attribute to volcanics from the Japanese Islands. Our data trends in all 3 isotope systems do not indicate the need for a volcanic provenance endmember, which is potentially due to the fact that we are analyzing at a coarser grain size (> 2 microns) and thus not sampling any redistributed material from the shelf. Thus the data from the past 200 ka in this study is consistent with previous work, indicating that the detrital fraction of sediment at IODP Site U1430 is dominantly East Asian dust.

Following the establishment that our data are generally consistent with published provenance data from the Sea of Japan, and Site U1430 in particular, and that the 2-16 micron detrital fraction provenance is predominantly East Asian dust with composition similar to the Loess Plateau or a mixed signal of Asian Deserts with little to no volcanic input, a closer examination of each of the isotope systems is warranted. In $^{207}Pb/^{204}Pb$ vs. $^{208}Pb/^{204}Pb$ space (Figure 4-7, Panel B) apart from a few extreme values, most of the PSAs are clustered very closely with limited distinguishing variability that would allow easy provenance fingerprinting. The U1430 samples exhibit only

moderate variability within this broader context and thus do not have good utility as a provenance tracer of the dust in this core site. In ε_{Nd} vs. $^{87}Sr/^{86}Sr$ space (Figure 4-7, Panel D) our samples exhibit a good range (from -11 to -6) in ε_{Nd} space and directly overlap with the values of PSA samples, but in $^{87}Sr/^{86}Sr$ space our samples are very tightly clustered at ~0.72, showing lower variability compared to the PSA range than ε_{Nd}. A complicating factor with the $^{87}Sr/^{86}Sr$ data is that the PSA sample compilation shows a range of grain sizes (bulk, clay, <5 micron, <75 microns), none of which overlap with our targeted grain size of 2-16 microns. For strontium this is an issue as there are higher $^{87}Sr/^{86}Sr$ ratios in small grain size fractions, potentially due to enrichment of clay minerals with high rubidium content and accompanying characteristically high $^{87}Sr/^{86}Sr$ ratios (Chen et al., 2007). This means that our samples fall in the middle of the range of values of the published PSA samples and thus are offset from both the isotopically heavier (coarse grain sizes) and lighter (fine grain sizes). This makes direct comparison to the PSAs more complicated as we do not have PSA measurements of the same grain size fraction, and combined with the fact that Sr shows lower variability than ε_{Nd} we choose to focus on ε_{Nd} as a provenance tracer.

In terms of assessing provenance change down core through time over the last 200 ka we will focus on ε_{Nd} as our most promising geochemical fingerprinting proxy. As discussed in the results, the ε_{Nd} time series shows cyclic variability between values of -11 and -7 at an orbital frequency (Figure 4-8), similar to a precessional timescale of ~20 kyr. At some parts of the time series these peaks and troughs are abrupt in nature due to the low resolution of the dataset; for example, the peak at 100 ka and the trough at 160 ka are each only defined by one data point. Other peaks and troughs are defined by two or more data points, such as the peak at 140 ka followed by the trough at 130 ka. Targeted measurement of samples during intervals where a peak or trough is defined by only one data point would increase the confidence in the signal of the time series during these times, and also better resolve the timing and nature of the peaks/troughs themselves. The amplitude of variability of the ε_{Nd} record changes significantly at 100 ka, from pronounced cyclic variability to very muted variability with no discernible trend around an average ε_{Nd} value of 9.5, interrupted only by a shift to an ε_{Nd} value of -11 in the most recent sample at 1 ka. Due to the low sampling resolution it is possible that higher amplitude peaks and troughs were missed from the sediment record and that the low variability is simply an artifact of sampling. Increased measurement resolution could help test this possibility. Comparison of the U1430 Nd provenance record with

the well-dated Asian Monsoon $\delta^{18}O$ record from speleothems over the past 200 ka (Figure 4-9) reveals a strong association of strong monsoon intervals (negative $\delta^{18}O$) with peaks in the Nd record (positive ε_{Nd} shift), and association of weak monsoon intervals (positive $\delta^{18}O$) with troughs in the Nd record (negative ε_{Nd} shift). The largest amplitude variability in the Nd record occurs during the largest amplitude 65°N summer insolation change of the last 200 ka (Figure 4-9), from a precessional maximum at 120 ka to a minimum at 110 ka, followed by a precessional maximum again at 100. The lowest amplitude variability in the Nd record occurs during the lowest amplitude 65°N summer insolation changes of the last 200 ka, from a precessional maximum at 50 ka to a muted minimum at 40 ka, followed by a muted maximum at 30 ka. This may indicate a high northern latitude insolation control on the ε_{Nd} variability similar to what is seen in the Asian Monsoon $\delta^{18}O$ record. The portion of the record that shows some discrepancy is at the insolation minimum/monsoon minimum at 115 ka where the measurements defining this trough in ε_{Nd} appear to reach a minimum about 8 kyr early at 123 ka. Close examination of the age control (Figure 4-5) over this interval reveals that the tie points over this time are at 69 ka and 135 ka, via correlation ties between the LR04 stack and bulk density/GRA measurements from U1424, and correlated via color measurements (L*) to U1430. Thus there is a great degree of flexibility in which the bulk density record could be shifted younger by multiple thousands of years to match the LR04 stack within the bounds of these tie points, meaning that the current discrepancy at the 123 ka interval of the U1430 ε_{Nd} record could feasibly be due to age model error.

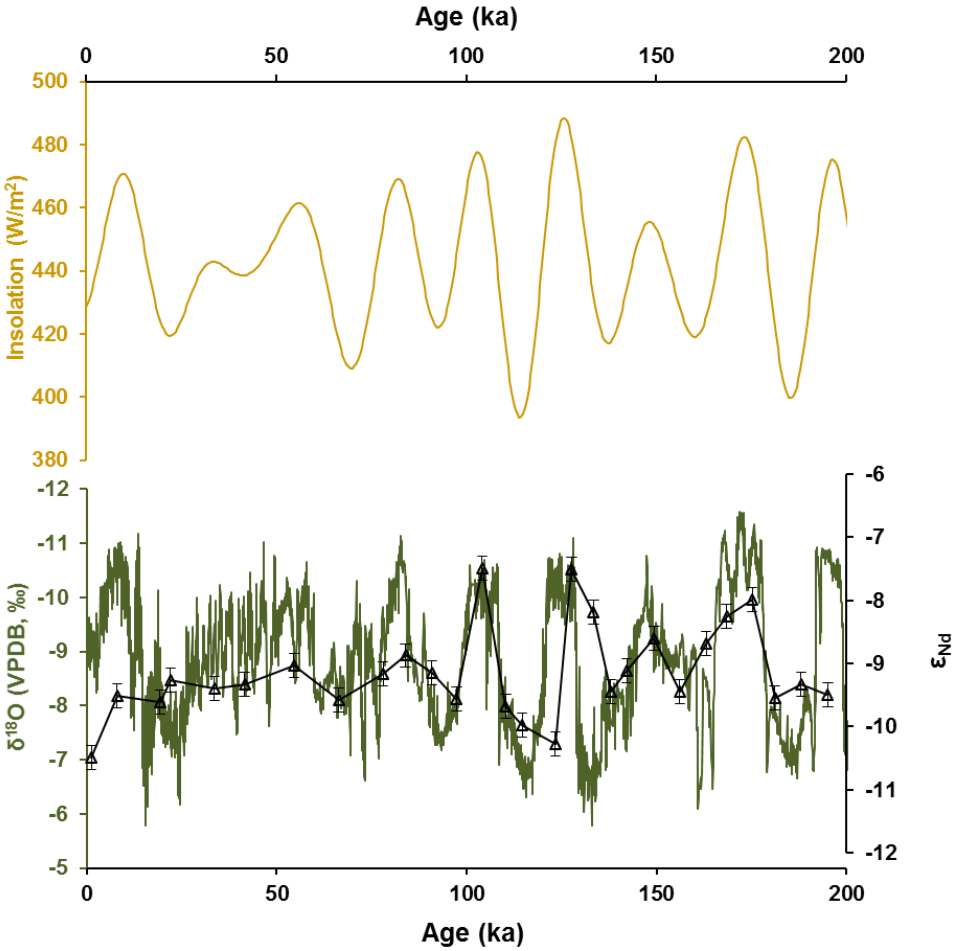

Figure 4-9. July 21 insolation at 65°N (yellow; Laskar et al., (2004), variations in the ε_{Nd} isotopic composition of the leached 2-16 μm fraction of U1430 sediments (black open triangles; this study), and the composite AM $\delta^{18}O$ record (green; Cheng et al., (2016). 2 sigma uncertainties on the neodymium isotopic measurements are shown as black bars on each sample.

The spatial pattern of the ε_{Nd} isotopic composition of the PSAs of Asian dust is key to interpretation of any provenance changes that the U1430 ε_{Nd} may imply, and thus the mechanistic relationship between atmospheric dynamical changes over Asia and changing climate. An examination of the PSA compilation of ε_{Nd} data in the spatial domain (Figure 4-10) reveals a distinct trend, with sandy lands north of 42°N having a more positive ε_{Nd} composition (between -6 and -1) and the sandy lands and deserts south of 42°N having a more negative ε_{Nd} composition (between -18 and -6). Thus mixing of eolian material from these distinct regions would produce an inferred signal that in ε_{Nd} space in the downwind aggregated sediment an increased (decreased) proportion of material from sites north (south) of 42°N would lead to more positive (negative) ε_{Nd} values. The ε_{Nd} time series from U1430 exhibits more positive values during intervals of summer insolation maxima and a strong Asian monsoon, with the implication of a greater proportion of material sourced from areas north of 42°N being transported to the Japan Sea during these times.

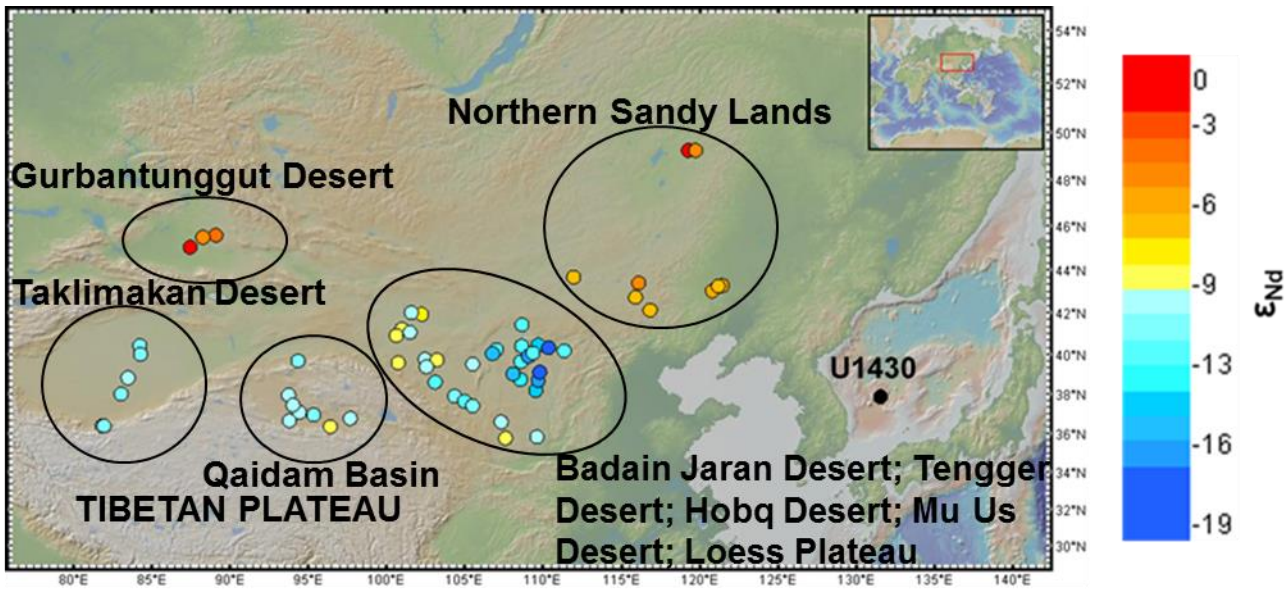

Figure 4-10. Map of ε_{Nd} isotopic composition of potential Asian dust source area samples (Biscaye et al., 1997; Bory et al., 2014; Chen et al., 2007; Ferrat et al., 2012) and IODP Site U1430 (black). Desert regions shown within black boundaries and labeled.

Nagashima et al. (2013) distinguish two major dust source areas to the Japan Sea, the Mongolian Gobi and Taklimakan Deserts (Figure 4-11). According to their work, in spring conditions there are severe dust storms in the Mongolian Gobi due to strong cold fronts from Siberia, which transports the dust eastward in near-surface northwesterly winds to the Japan Sea. In summer conditions the spring-time dust storm event frequency in the Gobi decreases due to the weaker latitudinal temperature gradient; concurrently the WJ moves north of the Tibetan Plateau and dust is entrained from the Taklimakan and transported eastward to the Japan Sea at high altitudes by the jet. Thus an earlier transition to summer conditions where the WJ is north of the Tibetan Plateau means an increase in material sourced from the Taklimakan vs. the Mongolian Gobi. Nagashima et al. (2011) note that during interstadial of Dansgaard-Oeschger (D-O) events that there is an increase in Taklimakan sourced material to the Japan Sea, indicative of an earlier transition to summer conditions; and that during D-O stadials there is an increase in Gobi sourced material to the Japan Sea indicative of a later transition to summer conditions. The Jet-Transition Hypothesis framework (Chiang et al., 2015) shows that there is a seasonal transition of the WJ and associated rainfall from south of the TP (Spring rains), to north of the TP with associated Meiyu rainfall in early summer, to very north of the TP with associated summer rains (Figure 4-1; Panel B). The hypothesis posits that, for example, during a time of increased summer insolation that the WJ would transition more quickly to the north of the TP and into the regime of summer rains, thus decreasing the Meiyu rainfall and increasing summer rainfall. Using this hypothesis and testing it using our new ε_{Nd} record from U1430 we would expect that during higher insolation times that the WJ should transition to its northern summer rainfall regime more quickly and remain there for longer, thus increasing the fraction of dust sourced from the more northern dust source areas. As described in the previous paragraph this is broadly consistent with our observations of a greater proportion of material sourced from areas north of 42°N being transported to the Japan Sea during times of higher summer insolation.

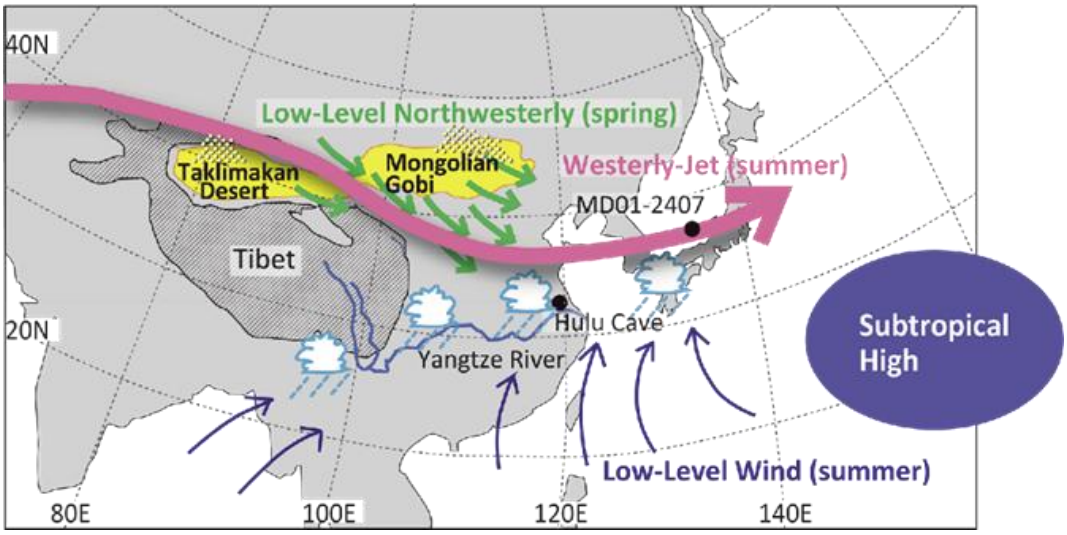

Figure 4-11. Map showing proposed main source areas of dust exported to the Sea of Japan, the Taklimakan and Mongolian Gobi Deserts (in yellow) (Nagashima & Tada, 2012). In spring low-level winds export dust predominantly from the Mongolian Gobi (green arrows). In summer the WJ moves north of the Tibetan Plateau (pink arrow) and dust is entrained from the Taklimakan and transported eastward to the Japan Sea at high altitudes by the jet.

The main discrepancy at this point between our records and those of Nagashima and colleagues is that their data show the Taklimakan and Gobi Deserts to be the main dust source regions to the Japan Sea core, whereas our provenance does not directly show this (nor does it contradict this as the Taklimakan and Gobi have similar ε_{Nd} values). Instead we focus on the more general difference between deserts north and south of 42°N. In order to strengthen our conclusions it is vital to understand exactly where the dust generation is occurring during the different seasons that Chiang et al. (2015) formalize, how this dust is transported to the Japan Sea (i.e., whether it is related to the WJ at all times), and the ε_{Nd} isotopic composition of these exact areas.

A convoluting factor not yet taken into account in this study is consideration of the flux of dust being exported from Asian source areas to the Japan Sea, and beyond. It can be hypothesized that a change in flux of one component/source area (e.g., decrease in southern sourced dust with a very negative ε_{Nd} signal), due to a weakening of the WJ while it is south or a decrease in erodibility of the land surface due to increased vegetation or soil moisture, while keeping the other component/source area input constant (e.g., the northern sourced dust with a less negative ε_{Nd} signal) could lead to a more positive ε_{Nd} isotopic composition of Japan Sea material without the need to invoke a source area change due to timing of the jet transition. ODP Site 1208A on the Shatsky Rise records high-resolution changes in dust flux from the Asian interior over the last 200 ka (Chapter 3), exhibiting a marked G-IG signal with high dust flux during glacial times and low dust flux during interglacial times. Comparison of this flux record with the ε_{Nd} record of Site U1430 (Figure 4-12) shows very little similarity in signal on a G-IG timescale. During the penultimate deglacial (Termination II) dust fluxes transition from high to low while ε_{Nd} values become more positive; during the last deglacial dust fluxes again transition from high to low while the muted ε_{Nd} signal becomes more negative. Thus there is no clear relationship between G-IG changes to dust flux from the Asian interior and ε_{Nd} shifts, supporting our interpretation that changes in the ε_{Nd} composition of Japan Sea material reflect changes in the timing of seasonal shifts of the WJ. The absence of a clear G-IG signal in the seasonal position of the WJ is also reflected in the absence of a strong G-IG signal in the Asian Monsoon $\delta^{18}O$ records (e.g., Figure 4-9), suggesting that the precessional forcing is the driving mechanism behind Asian climate even on longer orbital timescales. This lack of G-IG signal could be further explored my measuring

more samples for ε_{Nd} over more G-IG samples past 200 ka, and by confirming this with other provenance tools.

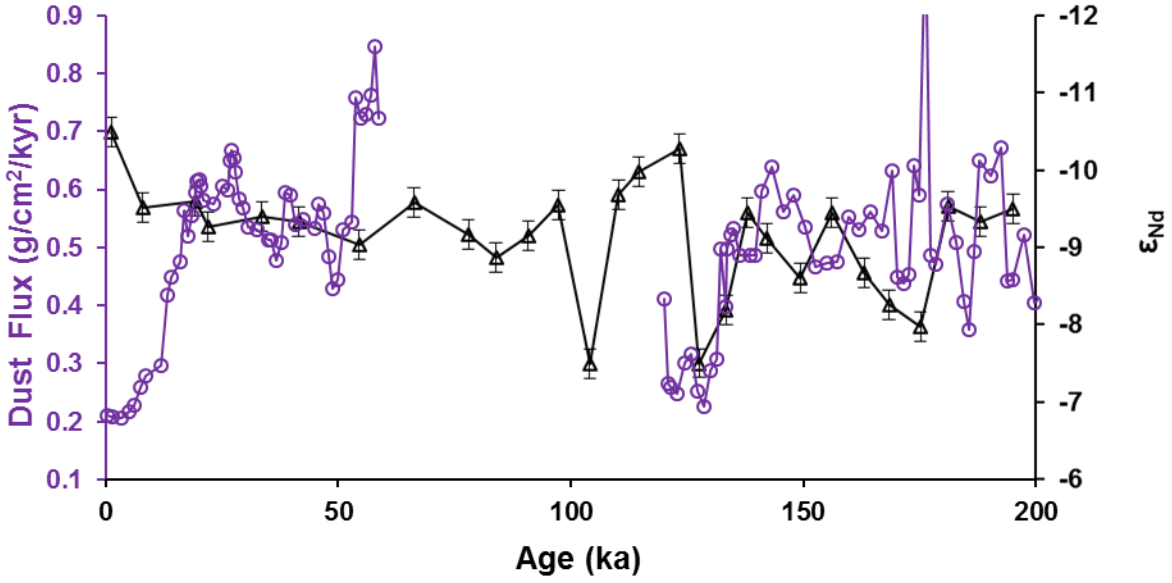

Figure 4-12. Variations in the ε_{Nd} isotopic composition of the leached 2-16 μm fraction of U1430 sediments (black open triangles; this study), and North Pacific ODP 1208A dust flux record (purple; Chapter 3). 2 sigma uncertainties on the neodymium isotopic measurements are shown as black bars on each sample.

4.6 Conclusions

Lead, neodymium, and strontium isotopic measurements made on isolated eolian material from IODP Site U1430 in the Sea of Japan show strong agreement with isotopic data from clays at the same core site, and overlap with the composition of the expected potential source areas for the eolian material at the site. This agreement builds confidence that these radiogenic isotope systems can be used in this region to track provenance change to the core site. The lead and strontium isotopic compositions over the last 200 ka were not utilized as discriminatory provenance tracers as the Pb isotopes did not show large enough variability compared to source area values, and for Sr isotopes interpretation was complicated by grain size concerns. The neodymium isotopic composition over the last 200 ka exhibited larger variability compared to source area values and thus was utilized to trace changing Asian dust provenance to Site U1430.

The neodymium isotopic record from Site U1430 shows precessional-scale variability from 200 to 100 ka, and more muted variability from 100 to 0 ka. The precessional-scale variability is coherent with times of strong (weak) Asian monsoon and high (low) summer insolation at 65°N while neodymium isotopes show a shift to more positive (negative) values and thus a higher (lower) proportion of eolian material sourced from north of 42°N. This indicates that during times of high summer insolation and a strong Asian Monsoon that the Westerly Jet shifts more quickly to the far north of the Tibetan Plateau, thus increasing the proportion of eolian material sourced from the northern source areas. This broadly aligns with the Jet-Transition Hypothesis posited by Chiang et al., (2015) attempting to link dynamics of the Westerly Jet and Asian rainfall on paleoclimate timescales. The neodymium record also reveals a clear lack of glacial-interglacial signal over the last 200 ka suggesting that precessional forcing is the driving mechanism behind Asian climate even on longer orbital timescales.

Chapter 5

Conclusions

Worldwide monsoon systems are affected by changing climate, on glacial-interglacial, orbital, and millennial timescales, impacting atmospheric circulation and associated rainfall. Reconstruction of these past changes to atmospheric circulation and rainfall is vital to understanding the impacts of external forcings on monsoon regions, but changes in winds do not leave a clear observable rock record to study. Thus marine sediment cores have been utilized to measure the accumulation rate of eolian dust exported from the continental interiors of monsoon regions in an effort to reconstruct changes to atmospheric circulation due to climate forcing.

This thesis generated new high resolution dust flux and provenance records over the past 330 ka from the West African and East Asian monsoon systems to investigate changes to these systems over multiple timescales. In Chapter 2 we extended a transect of dust flux records spanning the West African margin from 19-27 °N back to 35 ka, and back to 67 ka at ODP Hole 658C. These records showed a strong insolation control on West African climate, with multiple millennial-scale peaks in dust flux associated with cool events in the North Atlantic, superimposed on the orbital-scale trends. The records also exhibited a skipped precessional "beat" from 35-20 ka potentially due either to an increased gradient in insolation during this time of low obliquity, or to the influence of cold North Atlantic temperatures and large ice sheets in counteracting the local insolation forcing on North African climate. In Chapter 3 we constructed a 330 ka dust flux record from ODP Site 1208 on Shatsky Rise in the midlatitude western North Pacific, probing changes to atmospheric circulation and dust export from Asian source areas. The record showed a clear glacial-interglacial signal with dusty glacials, and low dust fluxes during interglacials, with evidence for a precessionally-driven insolation control overriding the glacial-interglacial signal predominantly during glacial times. Decreases to dust fluxes during glacial times occurred during maxima in June 21st insolation at 65°N, potentially driven by changes to the length of the dust season in East Asia, or less intense dust storms. This new record also allowed for a transect of dust flux records from the equatorial to subarctic North Pacific to be examined, suggesting a constant

glacial-interglacial dust transport mechanisms over this timescale. However the equatorial record showed more muted variability relative the midlatitude and subarctic records on orbital timescales, suggesting a change in dust transport across the North Pacific which does not reach the equator.
In Chapter 4 we showed the feasibility of using neodymium isotopes in the Sea of Japan at IODP Site 1208 to reconstruct Westerly Jet behaviour over East Asia by fingerprinting the changing source region of dust downwind. We then generated a neodymium provenance record spanning the last 200 ka which showed resolvable orbital-scale variability from 200 to 100 ka, and muted variability from 100 to 0 ka. The orbital-scale variability implied a quicker shift of the Westerly Jet to the north of the Tibetan Plateau during times of a strong Asian monsoon, offering support for Chiang et al.'s (2015) Jet-Transition Hypothesis. The neodymium provenance record also reveals the absence of a clear glacial-interglacial signal in the seasonal position of the Westerly Jet.

Comparing the broad findings from the dust flux and provenance records from the West African and East Asian Monsoon regions over the last 330 ka allows an integrated view of changes to atmospheric circulation due to climate forcing in these Northern Hemisphere areas affected by monsoon systems. The dust records all exhibit a direct response associated with high-latitude (65 °N) summer insolation forcing, with decreased dust export from West Africa during times of high insolation and a strong summer monsoon, decreased dust export from East Asia during times of high insolation which occur in glacial times, and a faster jet-transition to the north of the Tibetan Plateau during times of high insolation. The dust records also exhibit a response associated with changing high-latitude boundary conditions. In the North Atlantic during Greenland stadials there are abrupt increases in dust export from West Africa, and potential evidence that cold North Atlantic temperatures can counteract the direct insolation forcing on North African climate, while the East Asian dust flux record shows that glacial times are dusty. Thus, taken together, these records exemplify that changes to atmospheric circulation in the West African and East Asian Monsoon regions are controlled by a balance of climate forcing from a high-latitude direct response to insolation and high-latitude boundary condition changes.

The findings of this thesis can be strengthened with targeted future work to improve the robustness and resolution of the findings. The correlations between opal and dust fluxes at the West African margin sites have potential bias due to ^{230}Th-normalized sedimentation rates being used to calculate both opal and dust fluxes. Using an independent method to calculate opal fluxes, and comparing those to ^{230}Th-normalized dust fluxes would improve the reliability of the correlation. For the ODP 1208 core, interpretation of the data is limited due to unreliable portions of the age model at intervals where core gaps exist. Building multiple potential age models using the available age control data, and comparing the effect that differing age models have on the interpretation of the dust flux record would provide a way to test the validity of the dust flux record interpretation over the intervals with unreliable age control. The neodymium provenance record from IODP Site U1430 shows a resolvable association of positive shifts in ε_{Nd} with increased high-latitude summer insolation, however the record is at low temporal resolution such that some of the positive shifts are only defined by one data point calling the validity of the interpretation into question. Increasing the resolution of ε_{Nd} data from the core site, in particular over the intervals of largest change in existing ε_{Nd} data, would greatly enhance the robustness of the record. Future research beyond the scope of this thesis which would strengthen future Asian dust provenance work should focus on producing a data set of the radiogenic isotopic composition of potential Asian dust source areas, using sample preparation methods (leach protocol and grain size selection) aligned with sample preparation methods for the sediment samples in downwind archives.

Appendices

A. Chapter 2 Data

GC37										
Age (cal ka - BP1950)	Detrital Flux (g/cm2/kyr)	± (1 sigma)	Dust Flux (g/cm^2/ka)	± (1 sigma)	CaCO3 Flux (g/cm^2/ka)	± (1 sigma)	Corg Flux (g/cm^2/ka)	± (1 sigma)	Opal Flux (g/cm^2/ka)	± (1 sigma)
1.538	0.976	0.028	0.332	0.052	0.840	0.026	0.013	0.019	0.072	0.019
4.213	0.895	0.024	0.199	0.046	0.768	0.022	0.012	0.017	0.052	0.017
6.222	0.804	0.022	0.093	0.040	0.836	0.023	0.010	0.017	0.049	0.017
8.197	0.774	0.023	0.115	0.039	0.937	0.025	0.010	0.018	0.052	0.018
10.447	0.887	0.028	0.161	0.045	1.139	0.031	0.014	0.021	0.085	0.021
11.254	1.009	0.032	0.236	0.052	1.208	0.035	0.020	0.023	0.095	0.023
12.040	0.986	0.032	0.396	0.053	1.155	0.035	0.017	0.023	0.127	0.023
12.847	0.985	0.037	0.467	0.055	1.125	0.040	0.024	0.023	0.126	0.023
13.657	0.804	0.028	0.362	0.043	1.309	0.035	0.024	0.022	0.100	0.022
14.467	0.743	0.025	0.302	0.039	1.245	0.032	0.025	0.021	0.098	0.021
14.872	0.776	0.026	0.357	0.041	1.233	0.032	0.030	0.021	0.103	0.022
15.276	0.693	0.024	0.319	0.037	1.166	0.029	0.034	0.020	0.096	0.020
15.679	0.716	0.025	0.336	0.038	1.176	0.032	0.022	0.020	0.122	0.021
16.076	0.641	0.022	0.327	0.034	1.127	0.028	0.021	0.019	0.096	0.019
16.489	0.667	0.021	0.373	0.037	0.918	0.024	0.019	0.017	0.103	0.017
17.155	0.468	0.016	0.238	0.025	0.867	0.020	0.019	0.014	0.070	0.014
17.843	0.668	0.021	0.374	0.037	0.914	0.024	0.023	0.017	0.096	0.017
18.533	0.520	0.018	0.286	0.028	0.902	0.022	0.018	0.015	0.071	0.015
19.223	0.607	0.020	0.328	0.033	0.964	0.024	0.025	0.017	0.081	0.017
19.915	0.523	0.017	0.272	0.028	0.891	0.021	0.018	0.015	0.064	0.015
20.605	0.467	0.016	0.262	0.025	0.857	0.020	0.017	0.014	0.072	0.014
21.986	0.531	0.018	0.276	0.029	0.909	0.023	0.019	0.015	0.078	0.015
23.360	0.573	0.019	0.281	0.031	0.928	0.024	0.016	0.016	0.071	0.016
24.028	0.604	0.020	0.290	0.033	0.907	0.024	0.021	0.016	0.090	0.016
24.563	0.668	0.021	0.334	0.037	0.850	0.024	0.012	0.016	0.102	0.016
25.587	0.660	0.021	0.330	0.036	0.793	0.023	0.020	0.016	0.086	0.016
26.618	0.666	0.022	0.320	0.036	0.895	0.025	0.022	0.017	0.080	0.017
27.650	0.705	0.023	0.352	0.039	0.913	0.027	0.007	0.017	0.096	0.017
28.683	0.679	0.023	0.332	0.037	0.905	0.026	0.012	0.017	0.100	0.017
29.714	0.742	0.025	0.386	0.042	0.862	0.027	0.032	0.017	0.093	0.017
30.230	0.806	0.027	0.436	0.046	0.887	0.028	0.017	0.018	0.109	0.018
30.745	0.840	0.031	0.429	0.047	1.197	0.038	0.036	0.022	0.105	0.022
31.260	0.771	0.027	0.416	0.043	1.035	0.032	0.034	0.019	0.098	0.020
31.774	0.944	0.035	0.510	0.053	1.206	0.040	0.046	0.023	0.120	0.023
32.288	0.802	0.028	0.417	0.045	1.081	0.033	0.033	0.020	0.095	0.020
32.800	1.007	0.037	0.524	0.056	1.344	0.045	0.051	0.025	0.132	0.026
33.313	0.779	0.028	0.421	0.044	1.058	0.033	0.033	0.020	0.091	0.020
33.823	0.879	0.032	0.448	0.049	1.267	0.040	0.050	0.023	0.113	0.023
34.839	0.870	0.033	0.487	0.049	1.224	0.041	0.025	0.022	0.124	0.023
35.840	0.860	0.032	0.447	0.047	1.278	0.040	0.049	0.023	0.145	0.024
36.873	0.834	0.031	0.459	0.047	1.231	0.038	0.015	0.022	0.133	0.022

GC49										
Age	Detrital Flux	±	Dust Flux	±	CaCO3 Flux	±	Corg Flux	±	Opal Flux	±
(cal ka - BP1950)	(g/cm2/kyr)	(1 sigma)	(g/cm^2/ka)	(1 sigma)	(g/cm^2/ka)	(1 sigma)	(g/cm^2/ka)	(1 sigma)	(g/cm^2/ka)	(1 sigma)
0.558	1.096	0.035	0.581	0.058	0.837	0.030	0.021	0.020	0.089	0.021
1.004	1.032	0.031	0.525	0.054	0.842	0.028	0.017	0.020	0.084	0.020
2.212	0.967	0.031	0.484	0.051	0.821	0.028	0.021	0.019	0.060	0.019
3.438	0.850	0.024	0.378	0.044	0.756	0.023	0.020	0.017	0.061	0.017
4.556	0.742	0.022	0.274	0.038	0.814	0.023	0.020	0.016	0.057	0.016
5.569	0.489	0.015	0.108	0.025	0.843	0.018	0.014	0.014	0.042	0.014
6.571	0.498	0.016	0.114	0.025	0.896	0.019	0.012	0.015	0.048	0.015
7.473	0.435	0.015	0.083	0.022	0.927	0.018	0.012	0.014	0.047	0.014
8.374	0.400	0.015	0.076	0.020	0.931	0.018	0.015	0.014	0.049	0.014
9.205	0.438	0.017	0.110	0.022	1.060	0.023	0.012	0.016	0.060	0.016
10.110	0.490	0.018	0.186	0.025	1.011	0.022	0.022	0.016	0.066	0.016
10.834	0.622	0.025	0.305	0.033	1.210	0.035	0.028	0.020	0.108	0.020
11.280	0.822	0.026	0.378	0.043	1.106	0.029	0.044	0.021	0.135	0.021
11.738	0.785	0.028	0.448	0.042	1.148	0.034	0.029	0.021	0.161	0.022
12.196	0.781	0.031	0.430	0.043	1.248	0.041	0.035	0.022	0.153	0.023
12.645	0.989	0.035	0.524	0.053	1.035	0.036	0.049	0.023	0.210	0.024
12.950	1.058	0.039	0.698	0.059	1.157	0.042	0.040	0.025	0.197	0.025
13.181	1.266	0.061	0.836	0.075	1.293	0.062	0.056	0.028	0.220	0.030
13.517	1.034	0.041	0.672	0.058	1.317	0.048	0.043	0.026	0.204	0.027
13.921	0.769	0.027	0.454	0.042	1.220	0.034	0.044	0.022	0.186	0.023
14.326	0.941	0.033	0.536	0.051	1.436	0.041	0.053	0.026	0.201	0.027
15.122	0.843	0.029	0.531	0.046	1.031	0.033	0.034	0.021	0.161	0.021
15.565	0.798	0.038	0.511	0.047	1.030	0.047	0.023	0.020	0.165	0.021
16.023	0.874	0.027	0.595	0.047	0.992	0.029	0.029	0.021	0.162	0.021
16.943	0.939	0.033	0.648	0.052	0.956	0.034	0.030	0.021	0.149	0.021
17.835	0.883	0.028	0.574	0.048	0.867	0.028	0.038	0.019	0.148	0.020
18.808	0.868	0.047	0.564	0.053	0.930	0.050	0.033	0.020	0.128	0.021
19.813	0.836	0.032	0.552	0.047	0.857	0.032	0.035	0.018	0.088	0.018
20.822	0.783	0.030	0.517	0.044	0.831	0.031	0.038	0.018	0.105	0.018
21.831	0.804	0.037	0.530	0.047	0.863	0.039	0.034	0.018	0.102	0.018
22.839	0.786	0.026	0.511	0.043	0.827	0.027	0.029	0.018	0.124	0.018
23.828	0.936	0.032	0.637	0.052	0.914	0.031	0.028	0.020	0.118	0.020
24.271	0.902	0.031	0.631	0.050	0.875	0.031	0.024	0.019	0.133	0.020
24.739	0.885	0.030	0.611	0.049	0.964	0.031	0.032	0.020	0.141	0.021
25.212	0.890	0.032	0.632	0.050	0.829	0.030	0.025	0.019	0.128	0.019
25.687	0.875	0.031	0.604	0.049	0.916	0.031	0.024	0.020	0.142	0.020
26.163	0.854	0.030	0.592	0.047	0.765	0.028	0.028	0.018	0.120	0.018
26.636	0.839	0.027	0.585	0.046	0.771	0.026	0.028	0.017	0.109	0.018
27.110	0.780	0.025	0.546	0.043	0.672	0.023	0.039	0.016	0.107	0.016
27.587	0.867	0.029	0.624	0.048	0.790	0.027	0.036	0.018	0.113	0.018
28.059	0.857	0.029	0.617	0.048	0.739	0.026	0.026	0.017	0.116	0.018
28.532	0.888	0.031	0.631	0.049	0.803	0.029	0.033	0.019	0.124	0.019
29.002	0.922	0.032	0.654	0.051	0.733	0.028	0.019	0.018	0.134	0.019
29.470	0.935	0.032	0.645	0.052	0.692	0.027	0.034	0.018	0.155	0.019
29.938	0.890	0.031	0.650	0.050	0.788	0.029	0.028	0.018	0.122	0.019
30.400	0.910	0.033	0.655	0.051	0.951	0.034	0.019	0.020	0.153	0.021
30.852	0.877	0.032	0.649	0.050	0.897	0.032	0.035	0.019	0.111	0.019
31.291	0.867	0.031	0.641	0.049	0.905	0.032	0.048	0.019	0.120	0.020
31.801	0.844	0.030	0.616	0.047	0.893	0.031	0.046	0.019	0.114	0.019
32.324	0.912	0.034	0.657	0.052	0.983	0.035	0.045	0.021	0.130	0.021
32.844	0.935	0.037	0.692	0.054	1.031	0.039	0.050	0.021	0.126	0.022
33.361	0.905	0.034	0.661	0.052	0.916	0.034	0.043	0.020	0.116	0.020
33.875	0.975	0.038	0.692	0.056	0.973	0.038	0.047	0.021	0.134	0.022
34.391	0.900	0.034	0.630	0.051	0.991	0.037	0.056	0.021	0.129	0.021
34.903	0.845	0.032	0.600	0.048	0.945	0.034	0.045	0.020	0.124	0.020
35.415	0.968	0.037	0.688	0.055	0.955	0.037	0.042	0.021	0.143	0.022
35.925	1.075	0.050	0.763	0.064	1.084	0.050	0.046	0.024	0.174	0.025
36.434	1.035	0.038	0.745	0.059	0.926	0.036	0.055	0.022	0.147	0.022

GC68										
Age	Detrital Flux	±	Dust Flux	±	CaCO3 Flux	±	Corg Flux	±	Opal Flux	±
(cal ka - BP1950)	(g/cm2/kyr)	(1 sigma)	(g/cm^2/ka)	(1 sigma)	(g/cm^2/ka)	(1 sigma)	(g/cm^2/ka)	(1 sigma)	(g/cm^2/ka)	(1 sigma)
1.968	3.008	0.339	2.136	0.282	0.961	0.116	0.111	0.044	0.189	0.048
2.361	2.314	0.186	1.643	0.174	1.028	0.089	0.089	0.037	0.163	0.038
3.292	2.143	0.170	1.446	0.156	1.001	0.085	0.082	0.034	0.157	0.036
4.239	2.094	0.155	1.361	0.144	1.022	0.081	0.079	0.034	0.148	0.035
4.978	1.738	0.107	1.051	0.107	0.907	0.061	0.072	0.029	0.131	0.030
5.267	1.844	0.140	1.079	0.122	0.991	0.080	0.082	0.031	0.142	0.032
5.696	1.696	0.117	0.755	0.099	0.930	0.068	0.070	0.029	0.129	0.030
5.896	1.169	0.058	0.394	0.061	0.692	0.038	0.051	0.020	0.096	0.021
6.306	1.128	0.077	0.361	0.061	0.695	0.050	0.049	0.020	0.085	0.020
7.015	1.142	0.179	0.411	0.086	0.712	0.112	0.051	0.022	0.102	0.026
7.663	0.968	0.054	0.407	0.053	0.839	0.048	0.041	0.019	0.077	0.020
7.987	0.937	0.039	0.447	0.050	0.829	0.036	0.037	0.019	0.082	0.019
8.330	1.121	0.047	0.597	0.061	0.811	0.037	0.048	0.021	0.085	0.021
8.673	0.994	0.040	0.487	0.053	0.811	0.034	0.045	0.019	0.091	0.020
9.008	1.471	0.081	0.846	0.086	0.865	0.052	0.057	0.025	0.123	0.026
9.556	1.424	0.091	0.826	0.088	0.939	0.063	0.051	0.026	0.124	0.026
10.363	1.695	0.127	0.941	0.109	1.009	0.079	0.048	0.029	0.141	0.031
11.172	1.613	0.095	0.895	0.095	0.857	0.055	0.048	0.027	0.128	0.027
11.963	2.690	0.248	1.722	0.207	1.002	0.100	0.064	0.040	0.212	0.044
12.229	4.657	0.764	3.539	0.624	1.396	0.237	0.103	0.067	0.370	0.089
12.427	4.600	0.679	3.473	0.560	1.238	0.193	0.131	0.066	0.389	0.085
12.654	4.338	0.590	3.275	0.494	1.089	0.159	0.104	0.061	0.360	0.076
12.894	4.487	0.605	3.679	0.543	1.199	0.172	0.095	0.063	0.354	0.078
13.137	5.188	0.888	4.202	0.763	1.456	0.258	0.077	0.072	0.366	0.094
13.381	4.636	0.716	3.755	0.623	1.400	0.225	0.087	0.066	0.364	0.086
13.623	3.832	0.544	2.759	0.435	1.126	0.167	0.068	0.054	0.240	0.063
13.854	3.059	0.326	1.958	0.257	1.030	0.117	0.075	0.044	0.191	0.048
14.276	3.041	0.398	2.159	0.320	1.107	0.151	0.041	0.044	0.167	0.049
14.726	3.410	0.394	2.387	0.323	1.041	0.128	0.054	0.047	0.195	0.052
15.179	3.803	0.621	3.004	0.525	1.140	0.193	0.056	0.053	0.217	0.063
15.629	4.918	0.589	4.032	0.540	1.044	0.139	0.086	0.064	0.257	0.070
16.282	6.991	1.174	6.013	1.067	1.198	0.218	0.081	0.087	0.321	0.101
16.577	4.867	0.776	3.991	0.680	1.167	0.196	0.036	0.063	0.229	0.073
16.878	4.429	0.816	3.632	0.704	0.941	0.182	0.055	0.057	0.203	0.068
17.175	3.887	0.449	3.109	0.407	0.893	0.114	0.039	0.050	0.195	0.055
17.550	3.565	0.484	2.674	0.403	1.060	0.151	0.051	0.048	0.125	0.051
18.511	2.728	0.415	2.073	0.343	0.576	0.094	0.037	0.035	0.131	0.040
19.478	2.936	0.325	2.349	0.298	0.563	0.072	0.036	0.037	0.132	0.039
20.296	3.655	0.480	2.924	0.424	0.604	0.091	0.050	0.045	0.158	0.049
20.599	3.240	0.232	2.754	0.254	0.672	0.063	0.030	0.041	0.138	0.042
20.908	3.974	0.395	3.497	0.399	0.735	0.088	0.039	0.049	0.155	0.051
21.217	3.967	0.331	3.531	0.354	0.674	0.074	0.038	0.048	0.157	0.050
21.526	5.078	0.628	4.469	0.607	0.872	0.124	0.043	0.062	0.197	0.066
21.835	4.831	0.713	4.203	0.665	0.874	0.142	0.061	0.060	0.203	0.067
22.145	3.854	0.352	3.315	0.358	0.704	0.080	0.040	0.048	0.154	0.050
22.454	3.026	0.241	2.481	0.248	0.611	0.061	0.037	0.038	0.145	0.040
22.763	3.880	0.534	3.220	0.483	0.751	0.114	0.053	0.049	0.187	0.055
23.069	3.529	0.317	3.070	0.327	0.553	0.065	0.045	0.043	0.149	0.045
23.376	3.794	0.457	3.149	0.423	0.749	0.102	0.055	0.048	0.169	0.052
23.650	4.358	0.638	3.617	0.571	0.806	0.129	0.057	0.055	0.192	0.061
23.924	3.963	0.505	3.210	0.453	0.731	0.105	0.046	0.050	0.180	0.054
24.202	3.123	0.305	2.498	0.289	0.610	0.071	0.040	0.040	0.179	0.043
24.481	3.556	0.392	2.844	0.359	0.654	0.084	0.044	0.044	0.165	0.048
24.761	3.304	0.279	2.742	0.283	0.618	0.066	0.040	0.041	0.158	0.043
25.041	3.396	0.377	2.818	0.355	0.627	0.081	0.039	0.042	0.124	0.044
25.320	2.808	0.226	2.358	0.235	0.570	0.057	0.030	0.035	0.126	0.037
25.599	3.842	0.328	3.304	0.340	0.658	0.073	0.037	0.047	0.132	0.048
25.875	4.800	0.746	3.984	0.663	0.885	0.149	0.048	0.060	0.180	0.065
26.144	3.457	0.368	2.904	0.353	0.710	0.087	0.039	0.044	0.145	0.046
26.459	4.154	0.502	3.531	0.473	0.816	0.111	0.045	0.052	0.163	0.055

ODP658C										
Age	Detrital Flux	±	Dust Flux	±	CaCO3 Flux	±	Corg Flux	±	Opal Flux	±
(cal ka - BP1950)	(g/cm2/kyr)	(1 sigma)	(g/cm^2/ka)	(1 sigma)	(g/cm^2/ka)	(1 sigma)	(g/cm^2/ka)	(1 sigma)	(g/cm^2/ka)	(1 sigma)
0.158	1.952	0.110			0.909	0.058			0.189	0.032
0.263	1.896	0.077			0.953	0.047			0.205	0.031
0.369	0.353	0.009			0.180	0.007			0.038	0.006
0.474	0.759	0.024			0.398	0.016			0.090	0.013
0.506	2.060	0.118			1.093	0.069			0.230	0.036
0.621	1.955	0.078			1.052	0.050			0.206	0.033
0.660	0.904	0.030			0.472	0.020			0.090	0.015
0.699	1.899	0.084			1.015	0.052			0.194	0.032
0.776	1.867	0.083			1.025	0.052			0.186	0.032
0.883	1.772	0.089			0.990	0.055			0.167	0.030
0.931	1.892	0.139			1.037	0.081			0.214	0.035
0.980	1.764	0.100			0.938	0.058			0.166	0.030
1.028	1.840	0.079			1.024	0.050			0.183	0.031
1.149	1.564	0.047			0.914	0.035			0.164	0.027
1.198	1.847	0.094			1.050	0.059			0.177	0.032
1.246	1.714	0.085			0.964	0.053			0.157	0.029
1.295	1.809	0.081			1.045	0.053			0.179	0.031
1.368	1.716	0.083			0.997	0.053			0.176	0.030
1.529	1.858	0.132			1.060	0.080			0.173	0.033
1.642	1.695	0.140			1.027	0.088			0.171	0.032
1.755	1.721	0.068			1.011	0.046			0.156	0.029
1.868	1.689	0.082			0.970	0.052			0.161	0.029
1.981	1.911	0.115			1.105	0.072			0.169	0.033
2.276	1.647	0.083			0.927	0.052			0.153	0.028
2.458	1.742	0.064			1.064	0.046			0.166	0.030
2.641	1.653	0.093			0.949	0.058			0.149	0.029
3.096	1.766	0.100			0.992	0.061			0.147	0.030
3.278	1.602	0.064			0.923	0.043			0.136	0.027
3.460	1.628	0.092			0.973	0.059			0.151	0.029
3.642	1.553	0.065			0.959	0.045			0.145	0.027
3.825	1.712	0.112			1.044	0.072			0.156	0.031
4.007	1.664	0.106			0.972	0.066			0.142	0.029
4.342	1.529	0.058			0.932	0.041			0.180	0.027
4.404	1.600	0.058			0.949	0.041			0.163	0.028
4.529	1.513	0.063			0.931	0.044			0.134	0.026
4.746	1.449	0.052			0.988	0.040			0.132	0.026
4.902	1.603	0.082			0.984	0.055			0.130	0.028
4.964	1.473	0.090			0.890	0.058			0.117	0.026
5.026	1.529	0.057			0.904	0.039			0.120	0.026
5.088	1.516	0.064			0.868	0.042			0.118	0.025
5.150	1.598	0.105			0.970	0.067			0.127	0.028
5.213	1.491	0.075			0.884	0.049			0.115	0.025
5.399	1.351	0.047			0.929	0.037			0.105	0.024
5.522	1.061	0.037			0.858	0.032			0.093	0.020
5.830	0.845	0.042			0.904	0.044			0.084	0.019
6.077	0.881	0.025			0.933	0.026			0.089	0.019
6.385	0.818	0.035			0.936	0.038			0.087	0.019
6.508	0.821	0.023			0.888	0.023			0.083	0.018
6.816	0.759	0.022			0.928	0.024			0.081	0.018
6.939	0.835	0.024			0.853	0.024			0.081	0.018
7.371	0.748	0.028			0.919	0.032			0.084	0.018
7.543	0.778	0.022			0.933	0.024			0.083	0.018
7.575	0.779	0.036			0.909	0.040			0.077	0.018
7.608	0.779	0.026			0.939	0.028			0.079	0.018
7.640	0.742	0.025			0.907	0.028			0.082	0.017
7.673	0.746	0.023			0.928	0.025			0.086	0.018
7.705	0.769	0.024			0.976	0.027			0.090	0.018
7.738	0.795	0.026			1.010	0.029			0.093	0.019
7.770	0.774	0.023			0.962	0.025			0.089	0.018
7.803	0.746	0.022			0.916	0.024			0.087	0.018
7.835	0.772	0.025			0.971	0.028			0.093	0.018
7.868	0.747	0.026			0.976	0.031			0.092	0.018
7.900	0.750	0.023			0.993	0.026			0.091	0.018
8.329	0.818	0.024			1.057	0.026			0.115	0.020
8.582	0.984	0.033			1.315	0.039			0.148	0.025
8.836	0.965	0.032			1.273	0.037			0.150	0.024
9.089	0.986	0.047			1.238	0.056			0.155	0.025
9.343	1.007	0.037			1.306	0.044			0.158	0.025
9.596	0.946	0.041			1.242	0.050			0.141	0.024
10.196	0.995	0.036			1.284	0.042			0.148	0.025

ODP658C										
Age	Detrital Flux	±	Dust Flux	±	CaCO3 Flux	±	Corg Flux	±	Opal Flux	±
(cal ka - BP1950)	(g/cm2/kyr)	(1 sigma)	(g/cm^2/ka)	(1 sigma)	(g/cm^2/ka)	(1 sigma)	(g/cm^2/ka)	(1 sigma)	(g/cm^2/ka)	(1 sigma)
10.306	0.998	0.041			1.268	0.049			0.145	0.025
10.416	1.011	0.034			1.207	0.038			0.149	0.024
10.526	0.942	0.040			1.249	0.048			0.157	0.024
10.636	1.092	0.035			1.214	0.037			0.166	0.025
10.746	0.929	0.032			1.150	0.036			0.149	0.023
10.856	1.000	0.037			1.255	0.043			0.154	0.024
10.966	1.074	0.041			1.325	0.048			0.159	0.026
11.076	1.170	0.046			1.360	0.051			0.179	0.028
11.186	1.072	0.047			1.249	0.052			0.172	0.026
11.296	1.116	0.050			1.284	0.055			0.178	0.027
11.585	1.103	0.038			1.276	0.041			0.168	0.026
11.654	1.079	0.036			1.330	0.040			0.173	0.026
11.723	1.072	0.035			1.293	0.038			0.175	0.026
11.793	1.161	0.039			1.304	0.041			0.180	0.027
11.862	1.029	0.050			1.243	0.058			0.166	0.025
11.931	1.077	0.037			1.260	0.040			0.168	0.025
12.000	1.111	0.065			1.317	0.075			0.174	0.028
12.069	1.091	0.044			1.351	0.050			0.181	0.027
12.138	1.147	0.052			1.311	0.058			0.191	0.028
12.207	1.115	0.053			1.364	0.062			0.195	0.028
12.449	1.546	0.064			1.458	0.062			0.258	0.034
12.622	2.116	0.176			1.839	0.155			0.311	0.050
12.691	1.977	0.106			1.582	0.088			0.272	0.041
12.760	1.902	0.153			1.615	0.131			0.257	0.043
12.829	1.761	0.119			1.528	0.105			0.232	0.038
12.899	1.617	0.091			1.400	0.080			0.217	0.034
12.968	1.667	0.069			1.540	0.065			0.230	0.035
13.037	1.830	0.137			1.760	0.132			0.254	0.043
13.191	1.699	0.076			1.508	0.070			0.267	0.036
13.207	1.758	0.092			1.695	0.089			0.272	0.039
13.222	1.626	0.070			1.585	0.068			0.234	0.036
13.238	1.458	0.064			1.616	0.070			0.224	0.034
13.254	1.429	0.089			1.581	0.097			0.223	0.035
13.270	1.365	0.063			1.553	0.069			0.206	0.032
13.285	1.580	0.060			1.524	0.058			0.209	0.034
13.301	1.726	0.095			1.585	0.088			0.219	0.037
13.373	1.256	0.050			1.415	0.054			0.177	0.029
13.444	1.386	0.060			1.582	0.066			0.196	0.032
13.516	1.239	0.045			1.263	0.046			0.168	0.027
13.588	1.249	0.087			1.312	0.090			0.172	0.030
13.874	1.444	0.082			1.375	0.079			0.202	0.032
13.946	1.349	0.061			1.439	0.064			0.203	0.031
14.058	1.266	0.101			1.425	0.112			0.199	0.033
14.211	1.450	0.063			1.497	0.064			0.212	0.033
14.363	1.291	0.090			1.462	0.101			0.188	0.032
14.515	1.354	0.052			1.401	0.054			0.182	0.030
15.489	1.938	0.101			1.666	0.089			0.222	0.040
17.573	1.722	0.086			1.164	0.062			0.153	0.031
17.727	1.488	0.070			1.019	0.051			0.124	0.027
17.887	1.686	0.086			1.123	0.061			0.131	0.030
18.052	1.679	0.092			1.117	0.065			0.124	0.030
18.217	1.644	0.096			1.102	0.067			0.119	0.029
18.383	1.547	0.078			1.056	0.057			0.108	0.028
18.548	1.585	0.101			1.109	0.073			0.106	0.029
18.879	1.473	0.063	1.335	0.093	1.090	0.051	0.165	0.029	0.121	0.029
19.621	1.403	0.060	0.989	0.082	1.059	0.048	0.153	0.028	0.111	0.028
20.248	1.375	0.052	1.041	0.079	1.077	0.044	0.152	0.028	0.105	0.027
20.562	1.093	0.042	0.943	0.065	1.037	0.040	0.144	0.024	0.081	0.024
20.875	1.553	0.072	1.399	0.101	1.205	0.059	0.170	0.031	0.100	0.031
21.189	1.212	0.049	1.013	0.073	0.926	0.040	0.138	0.024	0.081	0.024
21.503	1.592	0.067	1.250	0.096	1.267	0.057	0.183	0.032	0.109	0.032
21.816	1.126	0.043	0.714	0.062	0.959	0.038	0.139	0.023	0.083	0.023
22.130	1.432	0.058	1.309	0.089	1.175	0.051	0.172	0.029	0.101	0.029
22.757	1.586	0.073	1.437	0.103	1.117	0.055	0.170	0.031	0.114	0.030
23.071	1.486	0.060	1.477	0.095	0.943	0.043	0.149	0.027	0.093	0.027
23.385	1.908	0.098	1.565	0.125	1.337	0.073	0.199	0.037	0.134	0.036
23.698	1.675	0.081	1.524	0.111	1.096	0.058	0.172	0.032	0.133	0.031
24.012	2.260	0.151	2.260	0.188	1.207	0.087	0.196	0.040	0.171	0.040
25.900	2.042	0.119	2.042	0.157	1.144	0.073	0.192	0.037	0.154	0.036
26.844	1.679	0.087	1.679	0.121	1.042	0.059	0.172	0.031	0.120	0.031
27.788	1.711	0.086	1.711	0.121	1.113	0.061	0.168	0.032	0.113	0.032
29.677	1.603	0.086	1.603	0.118	1.189	0.067	0.201	0.033	0.129	0.032
30.716	1.671	0.089	1.671	0.122	1.114	0.063	0.191	0.032	0.114	0.031

ODP658C										
Age	Detrital Flux	±	Dust Flux	±	CaCO3 Flux	±	Corg Flux	±	Opal Flux	±
(cal ka - BP1950)	(g/cm2/kyr)	(1 sigma)	(g/cm^2/ka)	(1 sigma)	(g/cm^2/ka)	(1 sigma)	(g/cm^2/ka)	(1 sigma)	(g/cm^2/ka)	(1 sigma)
31.169	1.671	0.094	1.671	0.126	1.031	0.063	0.172	0.032	0.142	0.031
31.622	1.978	0.116	1.978	0.152	1.237	0.077	0.204	0.037	0.132	0.036
32.076	1.592	0.091	1.592	0.121	0.916	0.057	0.169	0.029	0.119	0.029
32.529	1.452	0.072	1.452	0.102	1.154	0.060	0.185	0.030	0.108	0.029
32.982	1.392	0.063	1.360	0.093	0.846	0.043	0.160	0.026	0.106	0.025
33.435	1.748	0.099	1.748	0.132	1.213	0.073	0.203	0.035	0.124	0.034
33.889	1.475	0.080	1.430	0.107	1.036	0.060	0.179	0.030	0.150	0.029
34.342	2.169	0.159	2.169	0.192	1.461	0.111	0.238	0.044	0.218	0.044
35.248	2.088	0.127	2.088	0.164	1.299	0.084	0.230	0.040	0.207	0.040
36.155	2.121	0.143	2.121	0.178	1.348	0.096	0.234	0.042	0.201	0.041
36.608	1.679	0.102	1.679	0.132	1.168	0.075	0.195	0.034	0.165	0.033
37.061	1.991	0.125	1.991	0.159	1.363	0.090	0.230	0.040	0.207	0.040
37.967	2.143	0.169	2.143	0.200	1.577	0.127	0.258	0.046	0.211	0.045
38.421	1.711	0.091	1.711	0.125	1.354	0.075	0.222	0.036	0.149	0.035
38.859	1.755	0.102	1.755	0.134	1.413	0.085	0.230	0.038	0.141	0.036
39.293	1.276	0.066	1.276	0.092	1.107	0.059	0.177	0.028	0.112	0.027
39.727	1.409	0.071	1.409	0.100	1.250	0.065	0.208	0.031	0.121	0.030
40.161	1.375	0.080	1.281	0.101	1.182	0.070	0.189	0.031	0.134	0.030
40.596	1.813	0.126	1.813	0.155	1.565	0.110	0.246	0.041	0.162	0.039
41.030	1.401	0.095	1.401	0.118	1.133	0.078	0.187	0.031	0.140	0.030
41.464	1.568	0.100	1.568	0.127	1.384	0.090	0.222	0.036	0.148	0.034
42.333	1.431	0.079	1.431	0.107	1.185	0.068	0.192	0.031	0.145	0.030
43.201	1.343	0.069	1.328	0.096	1.190	0.063	0.200	0.030	0.121	0.029
43.987	1.000	0.047	0.946	0.067	1.017	0.047	0.173	0.024	0.091	0.023
44.256	1.155	0.057	0.999	0.076	1.149	0.057	0.198	0.028	0.112	0.027
44.690	0.927	0.042	0.859	0.061	0.973	0.044	0.158	0.022	0.091	0.022
45.559	1.257	0.065	1.257	0.090	1.008	0.054	0.158	0.026	0.111	0.026
46.179	1.187	0.064	1.026	0.081	1.036	0.057	0.180	0.027	0.120	0.026
46.902	1.374	0.077	1.018	0.089	1.156	0.067	0.197	0.030	0.146	0.030
47.811	1.652	0.115	1.652	0.142	1.021	0.075	0.176	0.032	0.149	0.032
48.265	1.825	0.136	1.779	0.161	1.233	0.096	0.208	0.038	0.182	0.037
48.741	1.269	0.076	1.269	0.099	0.988	0.061	0.167	0.027	0.133	0.027
49.218	0.892	0.040	0.880	0.060	0.797	0.037	0.133	0.020	0.092	0.019
49.694	1.598	0.111	1.598	0.137	1.286	0.091	0.222	0.036	0.160	0.034
50.647	0.719	0.032	0.280	0.038	0.879	0.037	0.156	0.019	0.102	0.019
51.599	0.649	0.030	0.263	0.035	0.893	0.037	0.157	0.019	0.100	0.018
52.076	0.875	0.045	0.178	0.045	1.033	0.051	0.182	0.024	0.135	0.023
52.552	1.138	0.065	0.511	0.064	1.199	0.068	0.240	0.030	0.176	0.029
53.028	0.598	0.023	0.405	0.034	0.632	0.024	0.120	0.015	0.087	0.015
53.505	0.980	0.053	0.606	0.059	0.995	0.054	0.193	0.025	0.129	0.024
53.981	1.471	0.098	1.471	0.123	1.124	0.077	0.190	0.032	0.148	0.031
54.457	1.805	0.136	1.805	0.163	1.003	0.080	0.164	0.034	0.156	0.033
54.897	2.518	0.265	2.518	0.294	1.331	0.145	0.229	0.049	0.219	0.049
55.301	2.018	0.162	1.869	0.181	1.438	0.119	0.243	0.043	0.197	0.042
55.704	1.091	0.065	0.870	0.075	1.157	0.068	0.190	0.028	0.118	0.026
56.107	1.098	0.066	0.767	0.072	1.043	0.063	0.170	0.026	0.111	0.025
56.511	1.144	0.076	0.836	0.080	1.188	0.079	0.176	0.029	0.130	0.028
56.914	1.209	0.083	0.876	0.085	1.133	0.079	0.179	0.029	0.137	0.028
57.721	1.071	0.065	0.339	0.057	1.336	0.078	0.217	0.030	0.111	0.028
58.124	0.566	0.025	0.178	0.029	0.756	0.031	0.130	0.016	0.067	0.015
58.528	0.769	0.042	0.244	0.041	1.032	0.053	0.168	0.022	0.091	0.021
58.931	1.324	0.084	0.775	0.082	0.913	0.061	0.200	0.028	0.116	0.026
59.334	1.077	0.064	0.721	0.069	1.140	0.067	0.179	0.027	0.122	0.026
59.738	1.054	0.061	0.709	0.067	0.988	0.058	0.164	0.025	0.122	0.024
60.141	1.470	0.108	1.046	0.106	1.423	0.105	0.222	0.037	0.189	0.036
60.948	1.373	0.084	1.155	0.099	1.174	0.074	0.175	0.031	0.159	0.030
61.755	1.464	0.096	1.464	0.120	1.138	0.077	0.173	0.031	0.162	0.031
62.158	1.553	0.101	1.553	0.127	1.284	0.085	0.180	0.034	0.165	0.033
62.562	2.412	0.233	2.412	0.263	1.932	0.189	0.278	0.055	0.226	0.053
62.965	1.257	0.083	1.257	0.104	1.247	0.082	0.172	0.030	0.128	0.029
63.368	1.281	0.080	1.281	0.102	1.112	0.071	0.150	0.028	0.127	0.028
64.175	1.495	0.061	1.495	0.096	1.148	0.050	0.162	0.030	0.118	0.030
64.579	1.202	0.047	1.202	0.076	0.961	0.040	0.144	0.025	0.105	0.024
64.982	1.843	0.153	1.843	0.179	1.368	0.116	0.199	0.039	0.153	0.038
65.405	1.277	0.077	1.277	0.100	0.986	0.061	0.145	0.026	0.106	0.026
65.808	1.018	0.057	0.836	0.069	0.854	0.049	0.129	0.022	0.095	0.022
66.615	0.970	0.057	0.820	0.069	0.994	0.059	0.148	0.023	0.088	0.023
67.019	1.256	0.090	1.256	0.110	1.295	0.093	0.182	0.031	0.113	0.030

B. Chapter 3 Data

ODP 1208A		
Age	Detrital/Dust Flux	±
(ka)	(g/cm2/ka)	(1 sigma)
0.300	0.211	0.01
1.350	0.208	0.01
3.277	0.206	0.01
4.884	0.218	0.01
6.199	0.228	0.01
7.441	0.260	0.01
8.723	0.279	0.01
11.837	0.297	0.01
13.303	0.418	0.01
14.035	0.448	0.02
16.070	0.475	0.02
16.779	0.565	0.02
17.589	0.521	0.02
18.502	0.556	0.02
19.220	0.595	0.02
19.605	0.615	0.02
20.102	0.616	0.02
20.493	0.607	0.02
20.995	0.582	0.02
23.115	0.576	0.02
25.141	0.607	0.02
26.307	0.598	0.02
26.762	0.650	0.03
27.168	0.669	0.03
27.523	0.655	0.03
27.928	0.630	0.03
28.586	0.584	0.02
29.600	0.568	0.02
30.512	0.536	0.02
32.640	0.530	0.02
35.072	0.514	0.02
35.680	0.514	0.02
36.693	0.479	0.02
37.706	0.509	0.02
38.720	0.595	0.03
39.733	0.590	0.03
40.746	0.540	0.02
42.368	0.549	0.02
44.800	0.532	0.02
45.813	0.576	0.03
46.826	0.560	0.02
47.840	0.484	0.02
48.853	0.428	0.02
49.866	0.445	0.02
50.880	0.532	0.02
52.906	0.544	0.03
53.818	0.758	0.04
54.933	0.723	0.04
55.946	0.731	0.04
56.960	0.762	0.05
57.973	0.847	0.06
58.685	0.724	0.04

ODP 1208A		
Age (ka)	Detrital/Dust Flux (g/cm2/ka)	± (1 sigma)
120.000	0.412	0.03
120.782	0.265	0.01
121.493	0.259	0.01
122.915	0.248	0.01
124.336	0.301	0.02
125.758	0.315	0.02
127.180	0.252	0.01
128.531	0.227	0.01
129.953	0.287	0.02
131.445	0.307	0.02
132.156	0.499	0.05
133.152	0.398	0.03
133.578	0.497	0.05
134.289	0.521	0.05
135.000	0.532	0.05
136.175	0.486	0.05
138.525	0.486	0.05
139.699	0.487	0.05
140.874	0.596	0.07
143.224	0.639	0.08
145.574	0.562	0.06
147.923	0.590	0.07
150.273	0.536	0.06
152.623	0.468	0.05
154.973	0.473	0.05
157.205	0.476	0.05
159.555	0.553	0.07
161.904	0.531	0.07
164.372	0.562	0.07
166.721	0.528	0.07
169.071	0.632	0.10
170.246	0.449	0.05
171.421	0.439	0.05
172.596	0.454	0.05
173.770	0.642	0.11
174.945	0.590	0.09
176.120	1.058	0.29
177.178	0.487	0.06
178.470	0.470	0.06
180.820	0.576	0.09
182.934	0.509	0.07
184.344	0.407	0.05
185.519	0.357	0.04
186.694	0.493	0.07
187.869	0.651	0.12
190.219	0.624	0.12
192.568	0.673	0.14
193.743	0.443	0.06
194.801	0.445	0.06
197.268	0.523	0.09
199.617	0.404	0.05

ODP 1208A		
Age (ka)	Detrital/Dust Flux (g/cm2/ka)	± (1 sigma)
201.967	0.420	0.06
204.317	0.368	0.05
206.667	0.319	0.04
209.016	0.333	0.04
211.366	0.451	0.08
212.423	0.485	0.09
213.598	0.751	0.21
214.891	0.380	0.06
216.066	0.339	0.05
217.240	0.286	0.03
218.063	0.964	0.36
227.974	0.410	0.07
229.257	0.409	0.07
231.822	0.341	0.05
234.388	0.360	0.06
236.826	0.359	0.06
239.520	0.334	0.05
240.803	0.297	0.04
242.086	0.486	0.12
243.369	0.193	0.02
244.652	0.211	0.03
245.806	0.333	0.06
247.217	0.487	0.13
249.370	0.405	0.09
252.000	0.444	0.11
253.894	0.401	0.09
255.788	0.346	0.07
257.682	0.296	0.05
259.577	0.333	0.07
261.376	0.283	0.05
265.259	0.333	0.07
267.153	0.390	0.10
268.953	0.645	0.27
270.942	0.436	0.12
272.836	0.644	0.28
274.825	0.766	0.40
276.529	0.684	0.32
278.423	0.633	0.28
280.412	0.603	0.26
282.306	0.368	0.10
284.106	0.329	0.08
286.000	0.525	0.21
288.308	0.471	0.17
291.128	0.214	0.04
293.436	0.307	0.08
296.000	0.309	0.08
298.883	0.311	0.08
301.286	0.660	0.38
303.688	0.373	0.12
305.610	0.240	0.05
308.494	0.179	0.03
310.896	0.194	0.04
315.701	0.403	0.16
321.227	0.111	0.01
324.831	0.484	0.26
329.636	0.109	0.01
333.000	0.163	0.03

C. Chapter 4 Data

IODP U1430								
Age (ka)	87Sr/86Sr	Std Deviation (2σ)	εNd	Std Deviation (2σ)	207Pb/204Pb	Std Deviation (2σ)	208Pb/204Pb	Std Deviation (2σ)
1.23	0.720063	0.000067	-10.49	0.19	15.6507	0.0012	38.9273	0.0026
8.04	0.719352	0.000067	-9.52	0.19	15.6484	0.0012	38.9607	0.0026
19.26	0.718570	0.000067	-9.60	0.19	15.6372	0.0012	38.8730	0.0026
22.07	0.719179	0.000067	-9.27	0.19	15.6263	0.0012	38.8583	0.0026
33.58	0.719746	0.000067	-9.40	0.19	15.6513	0.0012	38.9432	0.0026
41.51	0.719043	0.000067	-9.33	0.19	15.6421	0.0012	38.9142	0.0026
54.56	0.719182	0.000067	-9.03	0.19	15.6405	0.0012	38.9074	0.0026
66.29	0.717808	0.000067	-9.58	0.19	15.6379	0.0012	38.8842	0.0026
78.03	0.718251	0.000067	-9.16	0.19	15.6347	0.0012	38.8906	0.0026
83.91	0.718033	0.000067	-8.87	0.19	15.6483	0.0012	38.9310	0.0026
90.84	0.718637	0.000067	-9.15	0.19	15.6544	0.0012	38.9493	0.0026
97.32	0.719246	0.000067	-9.56	0.19	15.6500	0.0012	38.9110	0.0026
104.02	0.716652	0.000067	-7.50	0.19	15.6204	0.0012	38.8940	0.0026
110.29	0.719210	0.000067	-9.68	0.19	15.6392	0.0012	38.8812	0.0026
114.63	0.719245	0.000067	-9.98	0.19	15.6529	0.0012	38.9576	0.0026
123.29	0.719311	0.000067	-10.28	0.19	15.6562	0.0012	38.9571	0.0026
127.63	0.716527	0.000067	-7.50	0.19	15.6299	0.0012	38.8388	0.0026
133.41	0.718517	0.000067	-8.19	0.19	15.6250	0.0012	38.8237	0.0026
137.89	0.717984	0.000067	-9.44	0.19	15.6345	0.0012	38.8678	0.0026
142.12	0.718617	0.000067	-9.12	0.19	15.6326	0.0012	38.8674	0.0026
149.33	0.719612	0.000067	-8.60	0.19	15.6349	0.0012	38.8731	0.0026
156.08	0.719073	0.000067	-9.45	0.19	15.6302	0.0012	38.8574	0.0026
163.06	0.718919	0.000067	-8.68	0.19	15.6313	0.0012	38.8659	0.0026
168.42	0.719053	0.000067	-8.25	0.19	15.6318	0.0012	38.8821	0.0026
175.16	0.718062	0.000067	-7.98	0.19	15.6337	0.0012	38.9134	0.0026
181.07	0.719317	0.000067	-9.54	0.19	15.6320	0.0012	38.8791	0.0026
188.04	0.718471	0.000067	-9.33	0.19	15.6218	0.0012	38.8183	0.0026
195.01	0.718781	0.000067	-9.50	0.19	15.6361	0.0012	38.9306	0.0026

References

Adkins, J., deMenocal, P., & Eshel, G. (2006). The "African humid period" and the record of marine upwelling from excess 230Th in Ocean Drilling Program Hole 658C. *Paleoceanography*, *21*(4), 1–14. https://doi.org/10.1029/2005PA001200

Andersen, M. B., Stirling, C. H., Zimmermann, B., & Halliday, A. N. (2010). Precise determination of the open ocean $^{234}U/^{238}U$ composition. *Geochemistry, Geophysics, Geosystems*, *11*(12). https://doi.org/10.1029/2010GC003318

Anderson, C., Murray, R., Dunlea, A., Giosan, L., Kinsley, C., McGee, D., & Tada, R. (2019). Aeolian delivery to Ulleung Basin, Korea (Japan Sea), during development of the East Asian Monsoon through the last 12 Ma. *Geological Magazine*, 1–12. https://doi.org/10.1017/s001675681900013x

Bacon, M. P. (1984). Glacial to interglacial changes in carbonate and clay sedimentation in the Atlantic Ocean estimated from 230Th measurements. *Chemical Geology*, *46*(2), 97–111. https://doi.org/10.1016/0009-2541(84)90183-9

Battisti, D. S., Ding, Q., & Roe, G. H. (2014). Coherent pan-Asian climatic and isotopic response to orbital forcing of tropical insolation. *Journal of Geophysical Research*, *119*(21), 11,997-12,020. https://doi.org/10.1002/2014JD021960

Bayon, G., German, C. R., Boella, R. M., Milton, J. A., Taylor, R. N., & Nesbitt, R. W. (2002). An improved method for extracting marine sediment fractions and its application to Sr and Nd isotopic analysis. *Chemical Geology*, *187*(3–4), 179–199. https://doi.org/10.1016/S0009-2541(01)00416-8

Bayon, G., Toucanne, S., Skonieczny, C., André, L., Bermell, S., Cheron, S., … Barrat, J. A. (2015). Rare earth elements and neodymium isotopes in world river sediments revisited. *Geochimica et Cosmochimica Acta*, *170*, 17–38. https://doi.org/10.1016/j.gca.2015.08.001

Biscaye, P. E., Grousset, F. E., Revel, M., Zielinski, G. A., Vaars, A., & Kukla, G. (1997). Asian provenance of glacial dust (stage 2) in the Greenland Ice Sheet Project 2 Ice Core , Summit , Greenland, *102*(97).

Bory, A. J. M., Abouchami, W., Galer, S. J. G., Svensson, A., Christensen, J. N., & Biscaye, P. E. (2014). A Chinese imprint in insoluble pollutants recently deposited in central greenland as indicated by lead isotopes. *Environmental Science and Technology*, *48*(3), 1451–1457. https://doi.org/10.1021/es4035655

Braconnot, P., Harrison, S. P., Kageyama, M., Bartlein, P. J., Masson-Delmotte, V., Abe-Ouchi, A., … Zhao, Y. (2012). Evaluation of climate models using palaeoclimatic data. *Nature Climate Change*, *2*(6), 417–424. https://doi.org/10.1038/nclimate1456

Bradtmiller, L. I., McGee, D., Awalt, M., Evers, J., Yerxa, H., Kinsley, C. W., & deMenocal, P. B. (2016). Changes in biological productivity along the northwest African margin over the past 20,000 years. *Paleoceanography*, *31*(1), 185–202. https://doi.org/10.1002/2015PA002862

Bronk Ramsey, C. (2008). Deposition models for chronological records. *Quaternary Science Reviews*, *27*(1–2), 42–60. https://doi.org/10.1016/j.quascirev.2007.01.019

Cacho, I., Grimalt, J. O., Pelejero, C., Canals, M., Sierro, F. J., Flores, J. A., & Shackleton, N. (1999). Dansgaard-Oeschger and Heinrich event imprints in Alboran Sea paleotemperatures. *Paleoceanography*, *14*(6), 698–705. https://doi.org/10.1029/1999PA900044

Chen, J., Li, G., Yang, J., Rao, W., Lu, H., Balsam, W., … Ji, J. (2007). Nd and Sr isotopic characteristics of Chinese deserts : Implications for the provenances of Asian dust, *71*, 3904–3914. https://doi.org/10.1016/j.gca.2007.04.033

Cheng, H., Edwards, R. L., Sinha, A., Spötl, C., Yi, L., Chen, S., … Zhang, H. (2016). The Asian monsoon over the past 640,000 years and ice age terminations. *Nature*, *534*(7609), 640–646. https://doi.org/10.1038/nature18591

Chiang, J. C. H., Fung, I. Y., Wu, C. H., Cai, Y., Edman, J. P., Liu, Y., … Labrousse, C. A. (2015). Role of seasonal transitions and westerly jets in East Asian paleoclimate. *Quaternary Science Reviews*, *108*, 111–129. https://doi.org/10.1016/j.quascirev.2014.11.009

Clift, P., & Plumb, R. (2008). *The Asian Monsoon: Causes, History and Effects*. Cambridge: Cambridge University Press. https://doi.org/10.1017/CBO9780511535833

Cole, J. M., Goldstein, S. L., deMenocal, P. B., Hemming, S. R., & Grousset, F. E. (2009). Contrasting compositions of Saharan dust in the eastern Atlantic Ocean during the last deglaciation and African Humid Period. *Earth and Planetary Science Letters*, *278*(3–4), 257–266. https://doi.org/10.1016/j.epsl.2008.12.011

Collins, J. A., Govin, A., Mulitza, S., Heslop, D., Zabel, M., Hartmann, J., … Wefer, G. (2013). Abrupt shifts of the Sahara-Sahel boundary during Heinrich stadials. *Climate of the Past*, *9*(3), 1181–1191. https://doi.org/10.5194/cp-9-1181-2013

deMenocal, P.B. (1995). Plio-Pleistocene African climate. *Science*, *270*(5233), 53–59.

deMenocal, Peter B., Ortiz, J., Guilderson, T., Adkins, J., Sarnthein, M., Baker, L., & Yarusinsky, M. (2000). Abrupt onset and termination of the African Humid Period: Rapid climate responses to gradual insolation forcing. *Quaternary Science Reviews*, *19*(1–5), 347–361. https://doi.org/10.1016/S0277-3791(99)00081-5

deMenocal, Peter B., Ortiz, J., Guilderson, T., & Sarnthein, M. (2000). Coherent high- and low-latitude climate variability during the holocene warm period. *Science*, *288*(5474), 2198–2202. https://doi.org/10.1126/science.288.5474.2198

deMenocal, Peter B., Ruddiman, W. F., & Pokras, E. M. (1993). Influences of High- and Low-Latitude Processes on African Terrestrial Climate: Pleistocene Eolian Records from Equatorial Atlantic Ocean Drilling Program Site 663. *Paleoceanography*, *8*(2), 209–242.

Doherty, O. M., Riemer, N., & Hameed, S. (2012). Control of Saharan mineral dust transport to Barbados in winter by the Intertropical Convergence Zone over West Africa. *Journal of Geophysical Research Atmospheres*, *117*(19), 1–13. https://doi.org/10.1029/2012JD017767

Ferrat, M., Weiss, D. J., Dong, S., Large, D. J., Spiro, B., Sun, Y., & Gallagher, K. (2012). Lead atmospheric deposition rates and isotopic trends in Asian dust during the last 9.5kyr recorded in an ombrotrophic peat bog on the eastern Qinghai-Tibetan Plateau. *Geochimica et Cosmochimica Acta*, *82*, 4–22. https://doi.org/10.1016/j.gca.2010.10.031

Gasse, F. (2000). Hydrological changes in the African tropics since the Last Glacial Maximum. *Quaternary Science Reviews*, *19*(1–5), 189–211. https://doi.org/10.1016/S0277-3791(99)00061-X

Hathaway, J. C. (1956). Procedure for Clay Mineral Analyses Used in the Sedimentary Petrology Laboratory of the U.S. Geological Survey*. *Clay Minerals*, *3*(15), 8–13. https://doi.org/10.1180/claymin.1956.003.15.05

Hovan, S. A., Rea, D. K., & Pisias, N. G. (1991). Late Pleistocene Continental Climate and Oceanic Variability Recorded in Northwest Pacific Sediments. *Paleoceanography*, *6*(3), 349–370. https://doi.org/10.1029/91PA00559

Hovan, S. A., Rea, D. K., Pisias, N. G., & Shackleton, N. J. (1989). A direct link between the China loess and marine d180 records: Aeolian flux to the north Pacific. *Nature*, *340*, 296–298. https://doi.org/10.1038/340301a0

Irino, T., & Tada, R. (2002). High-resolution reconstruction of variation in aeolian dust (Kosa) deposition at ODP site 797, the Japan Sea, during the last 200 ka. *Global and Planetary Change*, *35*(1–2), 143–156. https://doi.org/10.1016/S0921-8181(02)00135-2

Irino, Tomohisa, Tada, R., Ikehara, K., Sagawa, T., Karasuda, A., Kurokawa, S., … Lu, S. (2018). Construction of perfectly continuous records of physical properties for dark-light sediment sequences collected from the Japan sea during integrated ocean drilling program expedition 346 and their potential utilities as paleoceanographic studies. *Progress in Earth and Planetary Science*, *5*(1). https://doi.org/10.1186/s40645-018-0176-7

Jacobel, A. W., McManus, J. F., Anderson, R. F., & Winckler, G. (2017). Climate-related response of dust flux to the central equatorial Pacific over the past 150 kyr. *Earth and Planetary Science Letters*, *457*, 160–172. https://doi.org/10.1016/j.epsl.2016.09.042

Jickells, T. D., An, Z. S., Andersen, K. K., Baker, A. R., Bergametti, C., Brooks, N., … Torres, R. (2005). Global iron connections between desert dust, ocean biogeochemistry, and climate. *Science*, *308*(5718), 67–71. https://doi.org/10.1126/science.1105959

Jolly, D., Prentice, I. C., Bonnefille, R., Ballouche, A., Bengo, M., Brenac, P., … Waller, M. (1998). Biome reconstruction from pollen and plant macrofossil data for Africa and the Arabian peninsula at 0 and 6000 years. *Journal of Biogeography*, *25*(6), 1007–1027. https://doi.org/10.1046/j.1365-2699.1998.00238.x

Kuper, R., & Kröpelin, S. (2006). Climate-controlled Holocene occupation in the Sahara: Motor of Africa's evolution. *Science*, *313*(5788), 803–807.

Kutzbach, J. E. (1981). Monsoon climate of the early Holocene: climate experiment with the Earth's orbital parameters for 9000 years ago. *Science*, *214*(OCTOBER), 59–61.

Laskar, J., Robutel, P., Joutel, F., Gastineau, M., Correia, A. C. M., & Levrard, B. (2004). Long-term solution for the insolation quantities of the Earth. *Astronomy and Astrophysics*, (428), 261–285. https://doi.org/10.1017/S1743921307011404

Li, F. (2007). Distribution characteristics of lead isotope in dust source areas and its trace significance in the North of China (in Chinese). *J Desert Res*, *27*(5), 738–744.

Lisiecki, L. E., & Raymo, M. E. (2005). A Pliocene-Pleistocene stack of 57 globally distributed benthic δ 18 O records. *Paleoceanography*, *20*(1), 1–17. https://doi.org/10.1029/2004PA001071

Liu, Y., Chiang, J. C. H., Chou, C., & Patricola, C. M. (2014). Atmospheric teleconnection mechanisms of extratropical North Atlantic SST influence on Sahel rainfall. *Climate Dynamics*, *43*(9–10), 2797–2811. https://doi.org/10.1007/s00382-014-2094-8

Martrat, B., Grimalt, J. O., Shackleton, N. J., De Abreu, L., Hutterli, M. A., & Stocker, T. F. (2007). Four climate cycles of recurring deep and surface water destabilizations on the Iberian margin. *Science*, *317*(5837), 502–507. https://doi.org/10.1126/science.1139994

McArthur, J. M., Howarth, R. J., & Bailey, T. R. (2002). Strontium Isotope Stratigraphy: LOWESS Version 3: Best Fit to the Marine Sr-Isotope Curve for 0–509 Ma and Accompanying Look-up Table for Deriving Numerical Age. *The Journal of Geology*, *109*(2), 155–170. https://doi.org/10.1086/319243

McGee, D., deMenocal, P. B., Winckler, G., Stuut, J. B. W., & Bradtmiller, L. I. (2013). The magnitude, timing and abruptness of changes in North African dust deposition over the last 20,000yr. *Earth and Planetary Science Letters*, *371–372*, 163–176.

https://doi.org/10.1016/j.epsl.2013.03.054
McGee, David, & deMenocal, P. B. (2017). *Climatic Changes and Cultural Responses During the African Humid Period Recorded in Multi-Proxy Data* (Vol. 1). Oxford University Press. https://doi.org/10.1093/acrefore/9780190228620.013.529
McGee, David, Marcantonio, F., McManus, J. F., & Winckler, G. (2010). The response of excess 230Th and extraterrestrial 3He to sediment redistribution at the Blake Ridge, western North Atlantic. *Earth and Planetary Science Letters*, *299*(1–2), 138–149. https://doi.org/10.1016/j.epsl.2010.08.029
McGee, David, Moreno-Chamarro, E., Green, B., Marshall, J., Galbraith, E., & Bradtmiller, L. (2018). Hemispherically asymmetric trade wind changes as signatures of past ITCZ shifts. *Quaternary Science Reviews*, *180*, 214–228. https://doi.org/10.1016/j.quascirev.2017.11.020
McGee, David, Winckler, G., Borunda, A., Serno, S., Anderson, R. F., Recasens, C., … Sun, Y. (2016). Tracking eolian dust with helium and thorium: Impacts of grain size and provenance. *Geochimica et Cosmochimica Acta*, *175*, 47–67. https://doi.org/10.1016/j.gca.2015.11.023
Meyer, I., Davies, G. R., Vogt, C., Kuhlmann, H., & Stuut, J. B. W. (2013). Changing rainfall patterns in NW Africa since the Younger Dryas. *Aeolian Research*, *10*, 111–123. https://doi.org/10.1016/j.aeolia.2013.03.003
Middleton, J. L., Mukhopadhyay, S., Langmuir, C. H., McManus, J. F., & Huybers, P. J. (2018). Millennial-scale variations in dustiness recorded in Mid-Atlantic sediments from 0 to 70 ka. *Earth and Planetary Science Letters*, *482*, 12–22. https://doi.org/10.1016/j.epsl.2017.10.034
Molnar, P., Boos, W. R., & Battisti, D. S. (2010). Orographic Controls on Climate and Paleoclimate of Asia: Thermal and Mechanical Roles for the Tibetan Plateau. *Annual Review of Earth and Planetary Sciences*, *38*(1), 77–102. https://doi.org/10.1146/annurev-earth-040809-152456
Mortlock, R. A., & Froelich, P. N. (1989). A simple method for the rapid determination of biogenic opal in pelagic marine sediments. *Deep Sea Research Part A, Oceanographic Research Papers*, *36*(9), 1415–1426. https://doi.org/10.1016/0198-0149(89)90092-7
Mulitza, S., Heslop, D., Pittauerova, D., Fischer, H. W., Meyer, I., Stuut, J. B., … Schulz, M. (2010). Increase in African dust flux at the onset of commercial agriculture in the Sahel region. *Nature*, *466*(7303), 226–228. https://doi.org/10.1038/nature09213
Mulitza, S., Prange, M., Stuut, J. B., Zabel, M., Von Dobeneck, T., Itambi, A. C., … Wefer, G. (2008). Sahel megadroughts triggered by glacial slowdowns of Atlantic meridional overturning. *Paleoceanography*, *23*(4), 1–11. https://doi.org/10.1029/2008PA001637
Murphy, L. N., Clement, A. C., Albani, S., Mahowald, N. M., Swart, P., & Arienzo, M. M. (2014). Simulated changes in atmospheric dust in response to a Heinrich stadial. *Paleoceanography*, *29*(1), 30–43. https://doi.org/10.1002/2013PA002550
Nagashima, K., & Tada, R. (2012). Teleconnection mechanism between millennial-scale Asian Monsoon dynamics and North Atlantic climate. *PAGES News*, *20*(2), 64–65. https://doi.org/10.22498/pages.20.2.64
Nagashima, K., Tada, R., Matsui, H., Irino, T., Tani, A., & Toyoda, S. (2007). Orbital- and millennial-scale variations in Asian dust transport path to the Japan Sea. *Palaeogeography, Palaeoclimatology, Palaeoecology*, *247*(1–2), 144–161. https://doi.org/10.1016/j.palaeo.2006.11.027
Nagashima, K., Tada, R., Tani, A., Sun, Y., Isozaki, Y., Toyoda, S., & Hasegawa, H. (2011).

Millennial-scale oscillations of the westerly jet path during the last glacial period. *Journal of Asian Earth Sciences*, *40*(6), 1214–1220. https://doi.org/10.1016/j.jseaes.2010.08.010
Nagashima, K., Tada, R., & Toyoda, S. (2013). Westerly jet-East Asian summer monsoon connection during the Holocene. *Geochemistry, Geophysics, Geosystems*, *14*(12), 5041–5053. https://doi.org/10.1002/2013GC004931
Nath, B. N., Makishima, A., Noordmann, J., Tanaka, R., & Nakamura, E. (2009). Comprehensive analysis for major, minor and trace element contents and Sr-Nd-Pb-Hf isotope ratios in sediment reference materials, JSd-1 and MAG-1. *Geochemical Journal*, *43*, 207–216. https://doi.org/10.2343/geochemj.1.0018
Ndeye, M. (2008). Marine reservoir ages in northern Senegal and Mauritania coastal waters. *Radiocarbon*, *50*(2), 281–288. https://doi.org/10.1017/S0033822200033580
Party, S. S. (2002a). Leg 198 summary. In *Bralower, T.J., Premoli Silva, I., Malone, M.J., et al., 198: College Station TX (Ocean Drilling Program)* (Vol. 198, pp. 1–84).
Party, S. S. (2002b). Site 1208. In *Bralower, T.J., Premoli Silva, I., Malone, M.J., et al., 198: College Station TX (Ocean Drilling Program)* (Vol. 198, pp. 1–93).
Pittauerov, D., Mulitza, S., Hettwig, B., Chehade, W., Stuut, J.-B., Mollenhauer, G., & Fischer, H. W. (2009). Application of self-absorption correction method in gamma spectroscopy for 210 Pb and 137 Cs sediment chronology on the continental slope off NW Africa . *Radioprotection*, *44*(5), 457–461. https://doi.org/10.1051/radiopro/20095085
Prospero, J. M., & Lamb, P. J. (2003). African droughts and dust trasport to the Caribbean: climate change implications. *Science*, *302*(5647), 1024–1027. https://doi.org/10.1126/science.1089915
Raczek, I., Jochum, K. P., & Hofmann, A. W. (2003). Neodymium and Strontium Isotope Data for USGS Reference Materials BCR-1, BCR-2, BHVO-1, BHVO-2, AGV-1, AGV-2, GSP-1, GSP-2 and Eight MPI-DING Reference Glasses - Raczek - 2007 - Geostandards Newsletter - Wiley Online Library. *Geostandards Newsletter*, *27*, 173–179. Retrieved from http://onlinelibrary.wiley.com/doi/10.1111/j.1751-908X.2003.tb00644.x/abstract%5Cnpapers3://publication/uuid/250EA78E-28A6-4C33-97C6-B8B80075A644
Reimer, P. J., Bard, E., Bayliss, A., Beck, J. W., Blackwell, P. G., Ramsey, C. B., … van der Plicht, J. (2013). IntCal13 and Marine13 Radiocarbon Age Calibration Curves 0–50,000 Years cal BP. *Radiocarbon*, *55*(04), 1869–1887. https://doi.org/10.2458/azu_js_rc.55.16947
Ridley, D. A., Heald, C. L., & Ford, B. (2012). North African dust export and deposition: A satellite and model perspective. *Journal of Geophysical Research Atmospheres*, *117*(2), 1–21. https://doi.org/10.1029/2011JD016794
Ridley, D. A., Heald, C. L., & Prospero, J. M. (2014). What controls the recent changes in African mineral dust aerosol across the Atlantic? *Atmospheric Chemistry and Physics*, *14*(11), 5735–5747. https://doi.org/10.5194/acp-14-5735-2014
Roe, G. (2009). On the interpretation of Chinese loess as a paleoclimate indicator. *Quaternary Research*, *71*(2), 150–161. https://doi.org/10.1016/j.yqres.2008.09.004
Romero, O. E., Kim, J. H., & Donner, B. (2008). Submillennial-to-millennial variability of diatom production off Mauritania, NW Africa, during the last glacial cycle. *Paleoceanography*, *23*(3), 1–17. https://doi.org/10.1029/2008PA001601
Ruddiman, W., Sarnthein, M., Baldauf, J., Backman, J., Bloemendal, J., Curry, W., … Yasuda, H. (1988). *Proceedings of the Ocean Drilling Program Leg 108*.
Sanchez Goñi, M. F., & Harrison, S. P. (2010). Millennial-scale climate variability and

vegetation changes during the Last Glacial: Concepts and terminology. *Quaternary Science Reviews*, *29*(21–22), 2823–2827. https://doi.org/10.1016/j.quascirev.2009.11.014

Schiemann, R., Lüthi, D., & Schär, C. (2009). Seasonality and interannual variability of the westerley jet in the Tibetan Plateau region. *Journal of Climate*, *22*(11), 2940–2957. https://doi.org/10.1175/2008JCLI2625.1

Seierstad, I. K., Abbott, P. M., Bigler, M., Blunier, T., Bourne, A. J., Brook, E., … Vinther, B. M. (2014). Consistently dated records from the Greenland GRIP, GISP2 and NGRIP ice cores for the past 104ka reveal regional millennial-scale δ18O gradients with possible Heinrich event imprint. *Quaternary Science Reviews*, *106*, 29–46. https://doi.org/10.1016/j.quascirev.2014.10.032

Serno, S., Winckler, G., Anderson, R. F., Jaccard, S. L., Kienast, S. S., & Haug, G. H. (2017). Change in dust seasonality as the primary driver for orbital-scale dust storm variability in East Asia. *Geophysical Research Letters*, *44*(8), 3796–3805. https://doi.org/10.1002/2016GL072345

Shen, X., Wan, S., France-Lanord, C., Clift, P. D., Tada, R., Révillon, S., … Li, A. (2017). History of Asian eolian input to the Sea of Japan since 15 Ma: Links to Tibetan uplift or global cooling? *Earth and Planetary Science Letters*, *474*, 296–308. https://doi.org/10.1016/j.epsl.2017.06.053

Singarayer, J. S., Valdes, P. J., & Roberts, W. H. G. (2017). Ocean dominated expansion and contraction of the late Quaternary tropical rainbelt. *Scientific Reports*, *7*(1), 1–9. https://doi.org/10.1038/s41598-017-09816-8

Skonieczny, C., McGee, D., Winckler, G., Bory, A., Bradtmiller, L. I., Kinsley, C. W., … Malaizé, B. (2019). Monsoon-driven Saharan dust variability over the past 240,000 years. *Science Advances*, *5*(1), eaav1887. https://doi.org/10.1126/sciadv.aav1887

Skonieczny, C., Paillou, P., Bory, A., Bayon, G., Biscara, L., Crosta, X., … Grousset, F. (2015). African humid periods triggered the reactivation of a large river system in Western Sahara. *Nature Communications*, *6*, 6–11. https://doi.org/10.1038/ncomms9751

Suman, D. O., & Bacon, M. P. (1989). Variations in Holocene sedimentation in the North American Basin determined from230Th measurements. *Deep Sea Research Part A, Oceanographic Research Papers*, *36*(6), 869–878. https://doi.org/10.1016/0198-0149(89)90033-2

Sun, D. (2004). Monsoon and westerly circulation changes recorded in the late Cenozoic aeolian sequences of Northern China. *Global and Planetary Change*, *41*(1), 63–80. https://doi.org/10.1016/j.gloplacha.2003.11.001

Tada, R., Murray, R. W., Alvarez Zarikian, C. A., Anderson, W. T. J., Bassetti, M.-A., Brace, B. J., … Ziegler, M. (2015). Site U1430. *Proceedings of the Integrated Ocean Drilling Program*, *346*. https://doi.org/10.2204/iodp.proc.346.110.2015

Tada, Ryuji, Irino, T., Ikehara, K., Karasuda, A., Sugisaki, S., Xuan, C., … Ziegler, M. (2018). High-resolution and high-precision correlation of dark and light layers in the Quaternary hemipelagic sediments of the Japan Sea recovered during IODP Expedition 346. *Progress in Earth and Planetary Science*, *5*(1), 1–10. https://doi.org/10.1186/s40645-018-0167-8

Tada, Ryuji, Murray, R. W., & Alvarez Zarikian, C. A. (2013). Asian Monsoon: onset and evolution of millennial-scale variability of Asian Monsoon and its possible relation with Himalaya and Tibetan plateau uplift. *Integrated Ocean Drilling Program Scientific Prospectus*, *346*. https://doi.org/10.2204/iodp.sp.346.2013

Tanaka, T., Togashi, S., Kamioka, H., Amakawa, H., Kagami, H., Hamamoto, T., … Dragusanu,

C. (2000). JNdi-1: A neodymium isotopic reference in consistency with LaJolla neodymium. *Chemical Geology*, *168*(3–4), 279–281. https://doi.org/10.1016/S0009-2541(00)00198-4

Tierney, J. E., Pausata, F. S. R., & De Menocal, P. B. (2017). Rainfall regimes of the Green Sahara. *Science Advances*, *3*(1), 1–10. https://doi.org/10.1126/sciadv.1601503

Tjallingii, R., Claussen, M., Stuut, J. B. W., Fohlmeister, J., Jahn, A., Bickert, T., … Röhl, U. (2008). Coherent high- and low-latitude control of the northwest African hydrological balance. *Nature Geoscience*, *1*(10), 670–675. https://doi.org/10.1038/ngeo289

Todt, W., Cliff, R. A., Hanser, A., & Hofmann, A. W. (1996). *Earth Processes: Reading the Isotopic Code*. *American Geophysical Union*. https://doi.org/10.1126/science.202.4365.304

Van der Does, M., Korte, L. F., Munday, C. I., Brummer, G. J. A., & Stuut, J. B. W. (2016). Particle size traces modern Saharan dust transport and deposition across the equatorial North Atlantic. *Atmospheric Chemistry and Physics*, *16*(21), 13697–13710. https://doi.org/10.5194/acp-16-13697-2016

Waelbroeck, C., Labeyrie, L., Michel, E., Duplessy, J. C., McManus, J. F., Lambeck, K., … Labracherie, M. (2002). Sea-level and deep water temperature changes derived from benthic foraminifera isotopic records. *Quaternary Science Reviews*, *21*(1–3), 295–305. https://doi.org/10.1016/S0277-3791(01)00101-9

Waelbroeck, C., Paul, A., Kucera, M., Rosell-Melé, A., Weinelt, M., Schneider, R., … Turon, J. L. (2009). Constraints on the magnitude and patterns of ocean cooling at the Last Glacial Maximum. *Nature Geoscience*, *2*(2), 127–132. https://doi.org/10.1038/ngeo411

Wang, W., Evan, A. T., Flamant, C., & Lavaysse, C. (2015). On the decadal scale correlation between African dust and Sahel rainfall: The role of Saharan heat low-forced winds. *Science Advances*, *1*(9), 2010–2015. https://doi.org/10.1126/sciadv.1500646

Wang, Y., Cheng, H., Edwards, R. L., Kong, X., Shao, X., Chen, S., … An, Z. (2008). Millennial- and orbital-scale changes in the East Asian monsoon over the past 224,000 years. *Nature*, *451*(7182), 1090–1093. https://doi.org/10.1038/nature06692

Weldeab, S., Lea, D. W., Schneider, R. R., & Andersen, N. (2007). 55,000 Years of West African Monsoon and Ocean Thermal Evolution. *Science*, *316*(June), 1303–1306.

Williams, R. H., McGee, D., Kinsley, C. W., Ridley, D. A., Hu, S., Fedorov, A., … deMenocal, P. B. (2016). Glacial to Holocene changes in trans-Atlantic Saharan dust transport and dust-climate feedbacks. *Science Advances*, *2*(11), 1–12. https://doi.org/10.1126/sciadv.1600445

Winckler, G., Anderson, R. F., Fleisher, M. Q., McGee, D., & Mahowald, N. (2008). Covariant glacial-interglacial dust fluxes in the equatorial Pacific and Antarctica. *Science*, *320*(5872), 93–96. https://doi.org/10.1126/science.1150595

Woodhead, J. D., & Hergt, J. M. (2000). Pb-isotope analyses of USGS reference materials. *Geostandards Newsletter*, *24*(1), 33–38. https://doi.org/10.1111/j.1751-908X.2000.tb00584.x

Zhang, W., Chen, J., Ji, J., & Li, G. (2016). Evolving flux of Asian dust in the North Pacific Ocean since the late Oligocene. *Aeolian Research*, *23*, 11–20. https://doi.org/10.1016/j.aeolia.2016.09.004

Zobeck, T. M., Gill, T. E., & Popham, T. W. (1999). A two-parameter Weibull function to describe airborne dust particle size distributions. *Earth Surface Processes and Landforms*, *955*, 943–955. https://doi.org/10.1002/(SICI)1096-9837(199909)24:10<943::AID-ESP30>3.0.CO;2-9